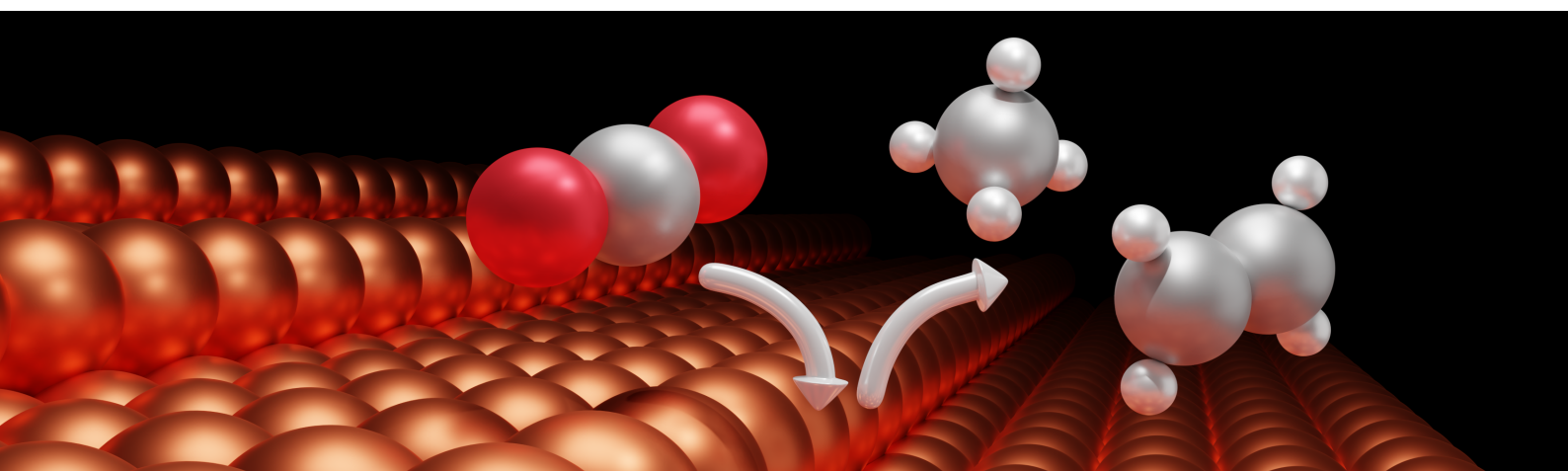


Computational Insights and Catalyst Syntheses for the Electrochemical CO₂ Reduction



Dissertation

zur Erlangung des akademischen Grades
Doktor der Naturwissenschaften
- Dr. rer. nat. -

Lukas Carl Friedrich John

Erklärung

Hiermit versichere ich, Lukas Carl Friedrich John, dass ich die vorliegende Arbeit mit dem Titel

„Computational Insights and Catalyst Syntheses for the Electrochemical CO₂ Reduction“

eigenständig verfasst habe und nur die angegebenen Quellen und Hilfsmittel verwendet habe. Alle benutzten Quellen sind wörtlich oder sinngemäß als solche kenntlich gemacht. Diese Arbeit wurde bisher bei keiner Universität eingereicht.

Münster, 29. Oktober 2018

Lukas John

Die vorliegende Arbeit wurde im Zeitraum von Juni 2015 bis Dezember 2018 in der Arbeitsgruppe von Prof. Stephan Schulz am Institut für Anorganische Chemie der Universität Duisburg-Essen angefertigt.

Finanziell wurde das Projekt durch die *International Max Planck Research School on Reactive Structure Analysis for Chemical Reactions* (IMPRS RECHARGE) gefördert.

1. Gutachter: Prof. Dr. Stephan Schulz
2. Gutachter: Prof. Dr. Alexander Auer

Tag der Disputation: 14.12.2018

Abstract

The efficient conversion of CO₂ into useful products can be a solution for two major problems the world is currently facing: energy storage and global warming. The electrochemical conversion of CO₂ is a promising field of research in this area, with copper as one of the most active catalysts with high selectivity towards valuable products. The present work deals with the electrochemical CO₂ reduction from a quantum mechanical point of view and applies the results in the synthesis of catalytic materials.

In chapter 4.1, model systems for catalytic surfaces of different materials are developed based on a quantum cluster approach. Subsequently, the chemically meaningful pathways to all experimentally observed C₁ and C₂ products are connected to a network of >70 intermediates. In chapter 4.2, the intermediates are placed on a copper surface model and their energies are evaluated via *density functional theory* (DFT) in order to find the minimum energy path and the rate-limiting step for each product. Adsorbed CO (*CO) was found to be the key intermediate for the selectivity towards CH₄ and C₂ products. Its hydrogenation to *CHO is the rate-determining step for CH₄ production and the dimerization of *CO opens the pathway to C₂ products like ethylene. Chapter 4.3 deals with the same evaluation on intermetallic NiGa and Ni₃Ga surfaces. On Ni₃Ga, the calculations suggest a different mechanism for CH₄ formation, which proceeds through the *COH intermediate and is caused by the structure-directing properties of Ga in the intermetallic phase.

In the following chapter 5.1, the possibilities to produce thin films of the investigated materials via *metal-organic chemical vapor deposition* (MOCVD) as a method to enhance their catalytic activity over the existing materials are investigated. Phase-pure samples with minimal contaminations were generated for the NiGa and Ni₂Ga phases through this method. The synthesis of additional Ni/Ga phases via induction melting is examined in chapter 5.2. For those phase-pure samples, any catalytic effect based on impurities and surface structuring can be excluded, which is necessary for a valid comparison between theory and experiment.

Übersicht

Die effiziente Umwandlung von CO₂ in nützliche Produkte kann helfen, zwei große und aktuelle Probleme der Menschheit zu lösen: Energiespeicherung und globale Erwärmung. Die elektrochemische Umwandlung von CO₂ ist ein vielversprechendes Forschungsgebiet, wobei Kupfer einer der aktivsten Katalysatoren mit einer starken Selektivität für wertvolle Produkte ist.

Die vorliegende Arbeit beschäftigt sich mit der elektrochemischen CO₂-Reduktion von einem quantenmechanischen Standpunkt aus und wendet die Ergebnisse in der Synthese katalytischer Materialien an.

In Kapitel 4.1 werden Modellsysteme von katalytischen Oberflächen verschiedener Materialien basierend auf einem Quanten-Cluster Ansatz entwickelt. Anschließend werden die chemisch sinnvollen Reaktionspfade zu allen experimentell beobachteten C₁- und C₂-Produkten zu einem Netzwerk aus >70 Intermediaten verbunden. In Kapitel 4.2 werden die Intermediate auf das Modell einer Kupfer-Oberfläche platziert und ihre Energien mittels *Dichtefunktionaltheorie* (DFT) evaluiert, um den Minimum-Energie-Pfad und den geschwindigkeitsbestimmenden Schritt für jedes Produkt zu ermitteln. Adsorbiertes CO (*CO) wurde als Schlüsselintermediat bezüglich der Selektivität für CH₄ und C₂-Produkte identifiziert. Die Hydrierung zu *CHO ist der geschwindigkeitsbestimmende Schritt für die Produktion von CH₄ und die Dimerisierung von *CO öffnet den Pfad zu C₂-Produkten, wie z.B. Ethylen. Kapitel 4.3 behandelt die gleiche Evaluierung auf intermetallischen NiGa- und Ni₃Ga-Oberflächen. Auf Ni₃Ga legen die Berechnungen einen unterschiedlichen Mechanismus für die Produktion von CH₄ nahe, der über das *COH-Intermediat führt, was durch die strukturdirigierenden Eigenschaften von Ga in der intermetallischen Phase hervorgerufen wird.

In dem darauffolgenden Kapitel 5.1 werden die Möglichkeiten für die Herstellung von dünnen Filmen der untersuchten Materialien mittels *metallorganischer chemischer Gasphasenabscheidung* (MOCVD) evaluiert, um deren katalytische Aktivität gegenüber existierenden Materialien zu steigern. Phasenreine Proben mit minimalen Kontaminationen konnten so für die NiGa- und Ni₂Ga-Phasen synthetisiert werden. Die Synthese von zusätzlichen Ni/Ga-Phasen durch Induktionsschmelzen wird in Kapitel 5.2 untersucht. Die so hergestellten Proben schließen eine veränderte katalytische Aktivität durch Verunreinigungen und Oberflächenstrukturierung aus, was für einen stichhaltigen Vergleich zwischen Theorie und Experiment notwendig ist.

Table of Contents

1	Introduction	9
2	Objective	13
3	Theoretical Background	15
3.1	Heterogeneous Catalysis	15
3.1.1	(Thermal) CO ₂ Reduction	17
3.1.2	Electrochemical CO ₂ Reduction.....	19
3.2	Chemical Vapor Deposition	22
3.3	Ni/Ga Intermetallics	28
3.4	Computational Chemistry	30
3.4.1	Schrödinger Equation	30
3.4.2	Electron Density.....	31
3.4.3	Kohn-Sham Equations.....	32
3.4.4	Exchange-Correlation Functional.....	34
3.4.5	Basis Sets.....	35
3.4.6	Limitations of DFT.....	35
3.5	Computational Heterogeneous Catalysis	37
3.5.1	Quantities of Interest.....	37
3.5.2	DFT in Practice	39
4	Evaluation Part I: Mechanistic Investigations	43
4.1	Model System	43
4.1.1	Construction of Model Clusters and Pre-Optimization	43
4.1.2	Network of Intermediates.....	47
4.2	Copper	50
4.2.1	Introduction to CO ₂ RR on Copper.....	50
4.2.2	Cluster Model.....	51
4.2.3	C ₁ Products.....	53
4.2.4	C ₂ Products.....	59
4.2.5	Competition between CO ₂ RR and HER.....	64
4.3	Ni/Ga Intermetallics	66
4.3.1	Introduction to CO ₂ RR on Ni/Ga Intermetallics	66

4.3.2	NiGa.....	67
4.3.3	Ni ₃ Ga.....	70
4.4	Other Materials.....	74
5	Evaluation Part II: Material Synthesis.....	77
5.1	MOCVD	77
5.1.1	Copper	77
5.1.2	Solid Precursors: Ni(acac) ₂ and Ga(acac) ₃	80
5.1.3	Liquid Precursors: Ga ^f Bu ₃ and Ni(allyl)Cp.....	82
5.2	Induction Melting	87
6	Conclusion and Outlook.....	91
6.1	Quantum Mechanical Calculations	91
6.2	Material Synthesis	93
7	Methods and Materials.....	95
7.1	General	95
7.2	Computational Details.....	95
7.3	Analytics.....	97
7.4	Chemical Vapor Deposition	98
7.5	Induction Melting	100
7.6	X-Ray Diffraction.....	101
7.7	Electron Microscopy	102
7.8	Energy-Dispersive X-Ray Spectroscopy.....	104
7.9	Syntheses.....	105
7.9.1	Inert Atmosphere.....	105
7.9.2	Solvents	105
7.9.3	Chemicals	105
8	References.....	111
9	Abbreviations	121
10	Acknowledgements	123
11	Publications.....	125

1 Introduction

The utilization of CO₂ as a chemical feedstock has intrigued chemists since it was discovered that nature uses this molecule to retain energy from sunlight via transformation to biomass during photosynthesis.

On the other hand, mankind has used this biomass with increasing growth since the industrial revolution to meet their energy demand. Biomass is converted into transportation fuels, electricity and materials, which ultimately results in the release of CO₂ and heat into the atmosphere. The global CO₂ emissions from fuel combustion for example passed 30 gigatons in 2010, which contribute in great amount to the increasing atmospheric CO₂ concentration (Figure 1).^[1]

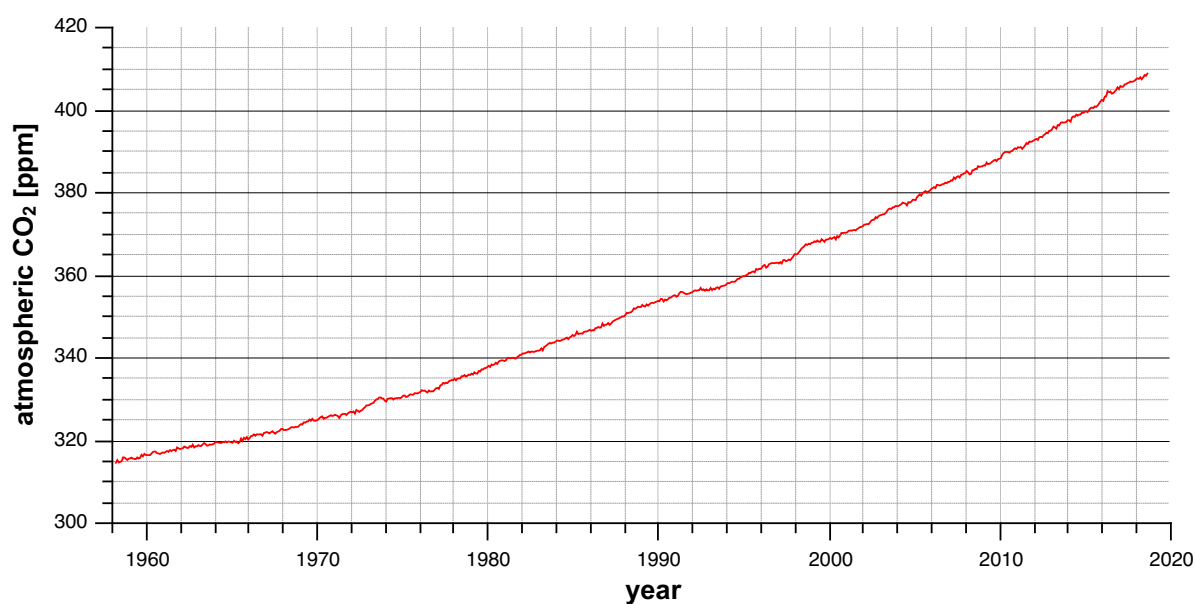


Figure 1. Atmospheric CO₂ levels from 1956 to 2018.^[2]

The anthropogenic release of CO₂ into the atmosphere can be directly linked to an increase of the global mean temperature during that time period.^[3] Besides the environmental impact, the utilization of fossil resources becomes more challenging and expensive with increasing depletion of available reservoirs.^[4,5]

Recycling CO₂ can counteract these effects by providing a source for fuels, commodity chemicals as well as an energy storage solution, and at the same time reducing anthropogenic CO₂ emissions.^[6–8]

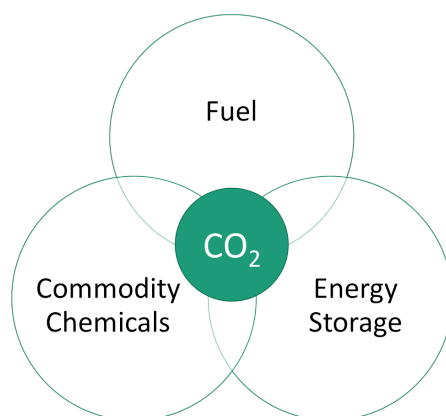


Figure 2. Utilization of CO₂.

While nature has developed a mechanism to utilize CO₂ from air at very low concentrations (currently 400 ppm, which corresponds to a partial pressure of 0.04 bar), it would be technologically very challenging to engineer a comparable industrial process.^[9] The high concentrations of CO₂, potentially even pressurized, necessary to ensure efficient conversion of CO₂ in large-scale processes with current technologies, can be supplied locally.^[10] They are available at industrial sites such as coal-fired power plants, in the iron, steel and cement production industry and in other chemical processes.

In sources with lower partial pressure, separation techniques can be applied to capture CO₂. A frequently implemented option is the amine-based method, especially utilizing monoethanolamine, in which CO₂ is separated from other gaseous components through the formation of an amine adduct. Other possible techniques apply carbonate looping, chemical looping, membranes and ionic liquids.^[8,10–12]

Although CO₂ reacts with medium to strong nucleophiles such as water and amines, it is generally perceived as an inert molecule. This is due to the high activation barrier for synthetic transformations such as C-H or C-C bond formations and the thermodynamic stability of CO₂. Fundamental research in the field of CO₂ activation, especially during the last quarter of the 20th century, yielded in substantial progress in the development of catalytic systems. Explored reactions with CO₂ include the incorporation in materials such as polycarbonates or polyurethanes, the synthesis of functional molecules such as alcohols, aldehydes or carboxylic acids, or the reduction to different commodity chemicals like CO, CH₄ or CH₃OH as an entrance into the established chemical value chain.^[13,14]

Driving forces of those reactions are either high-energy reactants like H₂, electrical current, solar radiation or thermal energy. However, additional catalysts are necessary to circumvent the kinetic inertness of CO₂.

Most prominent examples of the classical heterogeneously catalyzed conversion of CO₂ are the Sabatier reaction and the reverse water-gas-shift reaction, which opens the path to *Fischer-Tropsch* products.^[15–18] Although these processes are well established, they possess a few structural drawbacks. They operate only efficiently under steady load at large scale, which limits their applicability to centralized industrial sites where CO₂ is supplied constantly.

The growing implementation of renewable resources like wind energy and photovoltaics as sources of electricity calls for more flexible energy storage solutions to balance overcapacity originating from fluctuations in power generation. The *electrochemical CO₂ reduction reaction* (CO₂RR) provides a technology that can use the overproduction of electricity and store the energy chemically by producing fuels or other commodity chemicals whenever available. This flexibility is based on the reaction conditions such as ambient temperature and pressure, scale independence and tunable selectivity.

In this scenario, CO₂RR is competing directly with the electrochemical production of H₂, which is discussed as alternative fuel and energy storage solution.^[19–22] However, CO₂RR can provide a broad variety of products for chemical utilization, energy storage or fuel application with significantly higher volumetric energy densities. The selectivity for specific products can be tuned, depending on demand and point of integration into available infrastructures.^[23,24]

This broad scope of possible products also bears some challenges in the development of CO₂RR applications. In many cases, high overpotentials are required to produce desired products or to enhance product selectivity. Also, the competing *hydrogen evolution reaction* (HER) takes place at similar potentials like CO₂RR, reducing its efficiency.^[25]

In order to develop competitive CO₂RR processes, it is vital to understand the underlying principles leading to more active and selective electrocatalysts.

2 Objective

This doctoral thesis contains two parts. First goal is to gain a comprehensive view of the electrochemical CO₂ reduction from a quantum mechanical standpoint. The second part deals with the synthesis of suitable electrocatalytic materials for the experimental validation of the theoretical findings as well as possible enhancement over available materials.

The theoretical investigations start with the development of a model system that can be treated with standard *density functional theory* (DFT) methods in order to mimic the active surface of an electrocatalyst. A network of >70 possible intermediates is designed that covers chemically reasonable reaction pathways to all C₂ products. Those intermediates are then placed on the surface model and their geometries are optimized using DFT. The relative energies of connected intermediates are treated with the *computational hydrogen electrode* (CHE) model, accounting for applied potential and the addition of protons and electrons, in order to find the minimum energy path. Anticipated results are the reaction mechanism, the potential limiting step, expected onset potentials for products and an explanation for the experimentally observed product selectivity.

Materials of interest are copper and Ni/Ga intermetallics due to their unique ability to produce highly reduced molecules from CO₂ at moderate overpotentials. Copper can produce up to 20 different molecules, which results in the challenge to control product selectivity. Understanding the corresponding reaction mechanisms is necessary for a conscious catalyst improvement. A substantial number of experimental studies have been conducted with copper as electrocatalyst, which are the foundation for a valid comparison between theory and experiment. Ni/Ga intermetallics also produce highly reduced molecules such as CH₄ and C₂H₆ with a comparable activity as observed for copper.

The selectivity regarding those hydrocarbons is even higher, but *Faradaic efficiencies* (FE) are drastically reduced due to the preference of H₂ evolution.

Understanding the differences and communalities of Cu and Ni/Ga intermetallics might lead to the development of more active or selective catalysts for the electrochemical CO₂ reduction.

In the second part, material samples of copper and especially Ni/Ga intermetallics are synthesized based on the theoretical findings. *Chemical vapor deposition* (CVD) is used to produce thin films of the desired materials on silicon wafers to provide ready-to-use electrodes. Especially challenging is the phase pure preparation of Ni/Ga films due to the existence of many different Ni/Ga phases in narrow composition windows of the phase diagram. In addition to CVD, induction melting is used for the preparation of pure samples with defined Ni/Ga ratios that can easily be used for the comparison of theoretical and experimental results, due to their purity and lack of structural influences compared to the rough thin films from CVD.

3 Theoretical Background

3.1 Heterogeneous Catalysis

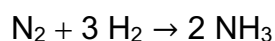
Catalysis plays an important role in chemical industry. It is regularly stated, that over 90% of all chemical products involve at least one catalytic step. Estimations suggest a contribution of catalytic processes to the world's *gross domestic product* (GDP) of >35%, providing significant economic driving forces for the understanding and development of new catalysts and catalytic processes.^[26]

This industry is based on the chemical conversion of reactants, following a specific path, to yield the desired products. This specific path is changed by catalysts in a way that the activation energies for the individual steps are lowered, resulting in higher reaction rates (kinetic control). As a broad definition, catalysts are substances that enhance reaction rates without being permanently altered in the process. They are often divided into three categories: *enzymatic*, *homogeneous* and *heterogeneous*. Enzymatic catalysts are proteins, which have evolved over several thousand years in order to efficiently and selectively catalyze metabolic processes in organisms under given conditions. In recent decades, bioengineering has developed methods for the utilization and manipulation of enzymes for the production of pharmaceuticals and other chemicals.^[27,28] Homogeneous catalysts are employed in the same phase as the reactant, in most cases a liquid solution. They are relevant to a number of industrial processes, such as the production of acetic acid in the *Monsanto* and *Cativa* process, polymerizations by *Ziegler-Natta* catalysts or oxidation reactions like the *Wacker* process.^[29–32] Heterogeneous catalysts are materials that exist in a different phase than the reactants and are typically solid. Due to this property, they can easily be separated from the products, which is a major advantage over homogeneous catalysts. Therefore, they are the preferred type of catalyst in large scale industrial processes, where catalyst leaching and product purification have substantial economic consequences.

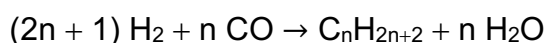
There are several different classes of heterogeneous catalysts, including transition metals or transition metal-based compounds (oxides, chlorides, sulfides, ...), zeolites, metal-organic-frameworks and supported homogeneous catalysts.

Transition metals are potent catalysts due to their variable oxidation states and partially filled *d*-orbitals, which allow them to form complexes and to adopt electronic and steric demands from reactants and intermediates, thus lowering activation energies. Several of the economically most important processes such as the *Haber-Bosch* process, the *Fischer-Tropsch* process and the synthesis of methanol and sulfuric acid, use transition metals or their compounds as catalysts. Their catalytic activity is often tuned with the application of support materials, for example Al₂O₃.

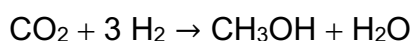
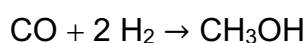
In the *Haber-Bosch* process, α -Fe catalyzes the reaction of nitrogen and hydrogen to ammonia under elevated pressures and temperature.



The *Fischer-Tropsch* process converts syngas into hydrocarbons with different late transition metal catalysts, such as Co, Fe, Ni or Ru.



In methanol synthesis, a complex mixture of Cu, ZnO and Al₂O₃ is used as catalysts to convert syngas or carbon dioxide.



During sulfuric acid production, vanadium pentoxide is utilized as catalyst to convert sulfur dioxide and oxygen into sulfur trioxide, which is then hydrolyzed.



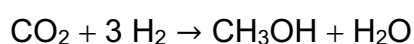
In addition to these processes, transition-metal catalysts are also used in different processes to utilize CO₂, which is discussed in the following two chapters.

3.1.1 (Thermal) CO₂ Reduction

Several methods have been developed to convert CO₂ into useful products for applications as fuels as well as the inclusion into the existing chemical value chain.

Thermodynamically, the hydrogenation of CO₂ does not impose any difficulties, since reaction enthalpies for the formation of methanol or methane are moderately negative with -50 kJ/mol and -165 kJ/mol, respectively. The challenge in these reactions, however, is to overcome the high activation energies. Several catalytic systems have been developed to meet this specific challenge.

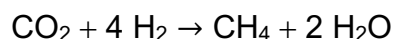
As mentioned above, the established process for methanol synthesis from syngas is also capable to convert CO₂ into methanol. It was developed in its current form by *Imperial Chemical Industries* (ICI) in 1966. The process operates at ca. 500 K with a pressure of ca. 100 bar and uses a Cu/ZnO/Al₂O₃ catalyst.^[33]



The active phase of this catalyst has been subject to several investigations. Recent experimental and theoretical evidence suggest a Cu stepped site, promoted with metallic Zn as the active site.^[34] Although it is challenging to evaluate such a reaction network based on theoretical methods, computational studies have led to the successful prediction of new catalysts such as Cu/Ni and Ni/Ga intermetallics, which have been verified in experimental studies.^[35,36]

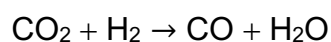
Methanol is used primarily as solvent or feedstock for chemical syntheses, but has also been discussed as potential fuel or fuel precursor due to its high volumetric energy density, making it an even more important commodity in the future.^[37–39]

The conversion of CO₂ through hydrogenation is called methanation. It was first discovered by *Sabatier* and *Senderens* in 1902.^[15] Methanation is used for the removal of CO and CO₂ from process gases, but is also discussed as a way to produce synthetic natural gas and to store energy from solar and wind power. Different late transition metal catalysts such as Ni, Ru and Rh have been investigated to produce CH₄ as part of a power-to-gas initiative.^[16,40]



Methane is the main component of natural gas, therefore, the methanation of CO₂ with renewable energy could be integrated in the existing gas distribution system and serve as fuel for transportation.

The reverse water-gas shift reaction is another way to convert CO₂ with H₂. Here, CO₂ is only partially reduced to CO. It is commonly used in the *Fischer-Tropsch* process to balance the H₂/CO ratio.



Different supported Cu and Fe-based catalysts are employed in this reaction.^[41] In addition to its established application, the resulting CO can be used in the *Fischer-Tropsch* process or in higher alcohol synthesis to produce liquid fuels, which are easier to handle than their gaseous counterparts.^[42]

A different approach for the direct coupling of solar energy and CO₂ utilization is photocatalysis. In photocatalytic applications, electron-hole (e⁻/h⁺) pairs are generated through the irradiation of semiconductor materials with (sun) light. In aqueous solutions of CO₂, those electrons cause the reduction of CO₂, while the h⁺ oxidize water to O₂ and protons.^[43] Reduction products vary widely from CO, CH₄ and higher hydrocarbons in the gas-phase, to oxygenated products such as alcohols, aldehydes or carbonic acids in the liquid phase.^[44] Several different materials have been evaluated as photocatalysts for CO₂ reduction, including TiO₂, graphitic carbon nitride and metal-organic frameworks.^[45-49] The photocatalytic CO₂ reduction is similar to its electrocatalytic counterpart, with respect to product scope and general functionality.

3.1.2 Electrochemical CO₂ Reduction

Electrical current can be used as a source of energy to convert CO₂ into several value-added products. Based on the choice of electrode material and its modification, up to 24 different products have been observed in aqueous solution to date.^[50–54] Developed materials include metals, transition metal oxides, transition metal chalcogenides and carbon-based materials.^[55]

Hori et al. compared different metals for the CO₂RR in 1985. While main group metals were found to primarily produce formic acid (Sn, Pb, In), transition metals preferentially produce CO (Zn, Au, Pd) or only H₂ (Ni, Fe), whereas Cu was the only pure metal to produce CH₄ in significant quantities.^[56] Only recently, Ag nano-foam was reported to produce significant amounts of CH₄ as well.^[57] The production of formic acid by use of main group metals is due to the weak binding energy of the adsorbed *COOH intermediate. On active transition metals, *COOH binds strong enough for further reduction to *CO, which binds less strongly and is therefore released. Cu has the (almost) unique ability to produce a variety of different highly reduced products, such as CH₄, C₂H₄ and EtOH, containing up to four carbon atoms. Those products are more valuable than formic acid and CO, because they can be used directly in existing infrastructures and exhibit higher energy densities, if considered as energy storage solution. Dependent on the electrodes' morphology, the product selectivity can be tuned over a wide range (see also chapter 4.2.1).^[55]

Based on the catalytic performance of the pure metals, several studies have been conducted with the application of alloys in order to improve the catalytic performance. Alloying changes the electronic and geometric structure of the material and thereby also the binding strength of the reaction intermediates. It was found that the performance of alloys, especially with regard to selectivity, can be tuned with compositional changes and even more with the inherent structural change. In general, the investigated catalytically active materials can be divided into four groups (Figure 3).

Group I metals are characterized by weak M-C bonds, resulting in the formation of formic acid as main product. Metals of the group II form slightly stronger M-C bonds, but still bind CO weak enough that it can be released easily. Group III metals represent well-balanced bond strength between too weak and too strong binding of the carbonaceous intermediates, thus opening the path for highly reduced products. Group IV metals bind CO too strongly. As a result, their activation energy are far too high for further reduction and the catalyst surface is poisoned by adsorbed CO.^[58]

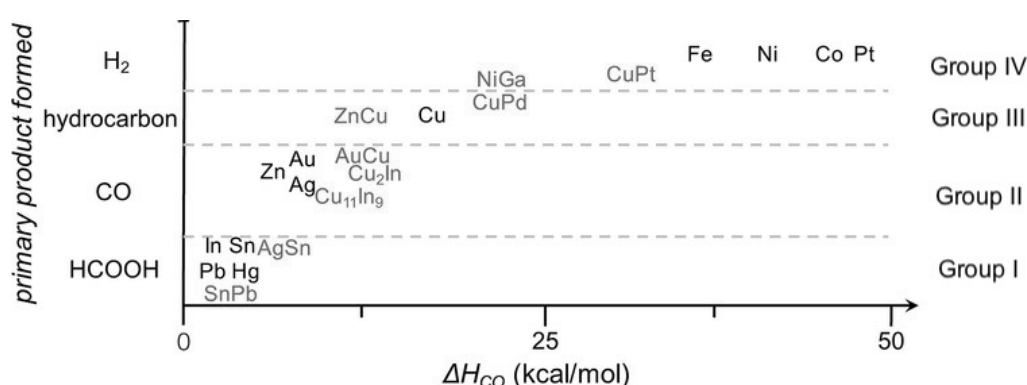


Figure 3. General relationship between product selectivity and CO binding strength (ΔH_{CO}).^[58]

Although the chemical reactivity of CO_2 is low, the equilibrium potentials of CO_2 reduction to various compounds are not very negative, compared to H_2 evolution in aqueous electrolyte solutions (Table 1).

Table 1. Main products of electrochemical CO_2 reduction and water reduction with their corresponding reduction potentials, referenced to *standard hydrogen electrode* (SHE) and pH 7 in aqueous solutions at 25 °C and 1 atm gas pressure.^[44]

Reaction	E^0 (V vs. SHE)
$2 H_2O + 2 e^- \rightarrow 2 OH^- + H_2$	-0.41
$CO_2 + 2 H^+ + 2 e^- \rightarrow CO + H_2O$	-0.51
$CO_2 + 2 H^+ + 2 e^- \rightarrow HCOOH$	-0.58
$CO_2 + 8 H^+ + 8 e^- \rightarrow CH_4 + 2 H_2O$	-0.24
$CO_2 + 6 H^+ + 6 e^- \rightarrow CH_3OH + H_2O$	-0.39
$2 CO_2 + 12 H^+ + 12 e^- \rightarrow C_2H_4 + 4 H_2O$	-0.34
$2 CO_2 + 14 H^+ + 14 e^- \rightarrow C_2H_6 + 4 H_2O$	-0.27
$2 CO_2 + 12 H^+ + 12 e^- \rightarrow C_2H_5OH + 3 H_2O$	-0.33

This situation leads to two considerable challenges. First, the potential from which on the individual products are observed experimentally is usually higher than the equilibrium potential. This overpotential is caused by energetically unfavorable elementary steps along the reaction pathway. Second challenge is the competing HER, which occurs at similar potentials, but with oftentimes lower overpotentials, thus lowering the Faradaic efficiency of CO₂ reduction.

In order to compare the performance of different catalytic materials and experimental setups, the definition of fundamental parameters is necessary.

The onset potential refers to the applied voltage necessary to produce detectable amounts of the specific product. It has usually a higher absolute value than the corresponding equilibrium potential and the difference between them is defined as overpotential.

The selectivity towards a specific product in an electrochemical reaction can be expressed as the Faradaic efficiency (FE) ϵ_F ,

$$\epsilon_F = \frac{\alpha \cdot n \cdot F}{Q}$$

where α is the number of electrons transferred in the reaction, n is the produced number of moles of that product, F is Faraday's constant and Q refers to the complete amount of charge passed.

The current density is a measure for the reaction rate and is important for the applicability of a technical process, since it determines the size and thereby cost of a facility for a given production rate. The overall current density is usually calculated via dividing the current by the geometric surface area of the working electrode. The partial current density for a certain product can be obtained by multiplying the corresponding Faradaic efficiency with the overall current density.^[55]

Despite numerous reported studies, which yielded catalytic systems with improved activity and selectivity, several challenges still remain unsolved: High overpotentials, a result of unfavorable adsorption energies of key reaction intermediates, resulting in distinct potential limiting steps; competition between CO₂ reduction and HER results in the low FE, while the poor product selectivity is caused by a variety of energetically similar pathways.

Understanding the limiting steps and reaction pathways towards the different products is expected to help in the development of new enhanced catalysts.

3.2 Chemical Vapor Deposition

Technical processes for the deposition of material thin films from the gas-phase include the *physical vapor deposition* (PVD), *atomic layer deposition* (ALD), which utilizes chemical reactions during deposition, and the *chemical vapor deposition* (CVD). Fundamental process of CVD is the decomposition of precursors on hot surfaces. CVD is sectioned further into sub-classes, based on the working pressure, temperature, precursor type and reactor geometry.

A CVD process is operated between atmospheric pressure and high vacuum. The reduction in pressure leads to a greater mean free path length of the precursor molecules, thus reducing gas-phase reactions.

The energy input, necessary for the decomposition process, is usually provided thermally. In some cases, the energy is supplied in form of a plasma or by radiation with light. In hot-wall reactors the whole reaction chamber is heated by an external source, whilst in cold-wall reactors only the substrate is heated, preventing unnecessary material deposition on the reactor walls (Figure 4).

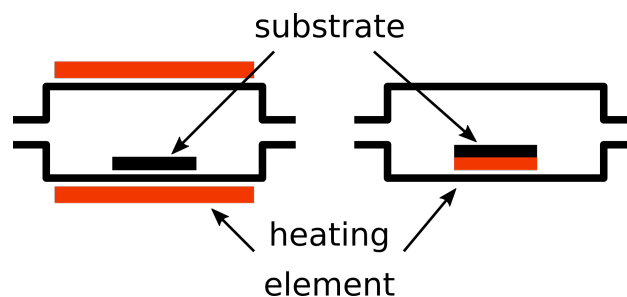


Figure 4. Scheme of a hot-wall (left) and a cold-wall (right) CVD reactor.

An important subclass is the *metal organic chemical vapor deposition* (MOCVD). Metal organic precursors, such as metal alkyls, aryls, cyclopentadienyls or carbonyls, do have distinct advantages over classical precursors, such as metal halides, hydrides or oxides. They are often thermally less stable and have a high vapor pressure, which makes them applicable in a broader range of temperatures and pressures. For the preparation of intermetallic phases, the intended metals can be supplied in form of individual molecules (dual source precursors) or already combined into one precursor molecule (single source precursors). Single source precursors allow for the metals to be supplied to the substrate in exactly the intended stoichiometry, although in case of metal CVD they tend to be thermally instable and possess low vapor-pressures. Dual source precursors on the other hand are more versatile and can be modified more easily, meeting the necessary criteria for optimal deposition, like vapor pressure and thermal stability.

During MOCVD, a sequence of individual steps, such as transport, sorption, nucleation and reaction processes, takes place simultaneously (Figure 5).

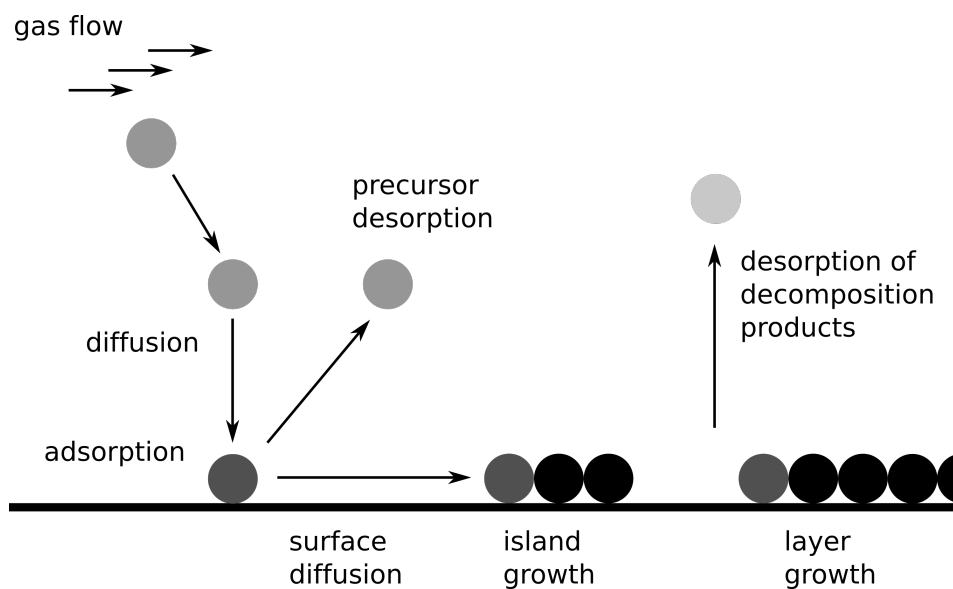


Figure 5. Processes in MOCVD.

In a first step, the precursors are vaporized. Solid precursors are sublimed and for liquid precursors usually bubbler cylinders are used in which the carrier gas is conveyed through the liquid and thus saturated with the precursor.

The amount of precursor in the gas phase is controlled via the working pressure and temperatures of the precursor containers. In case of dual source precursors, their stoichiometry in the gas phase can be controlled by a difference in gas flow rates and by cooling or heating the precursor containers individually.

During transport of the precursor molecules from the container into the reactor, condensation can be prevented by heating the supply pipes. On the other hand, the temperature should be low enough to prevent gas phase reactions, which would lead to partial or even total decomposition of the precursors.

The precursors are transported into the reactor via convection, initiated by a pressure gradient between inlet and outlet. The flow profile in the reactor strongly depends on the working pressure. If the pressure is reduced, the flow profile typically meets the conditions for laminar flow (Figure 6). Over the substrate, the gas flow is reduced by friction between the gas molecules and the static surface

until convection is reduced to zero and mass transport occurs through diffusion only. Inside this boundary layer, diffusion of the precursor molecules is caused by a concentration gradient between the flowing gas and the substrate's surface.

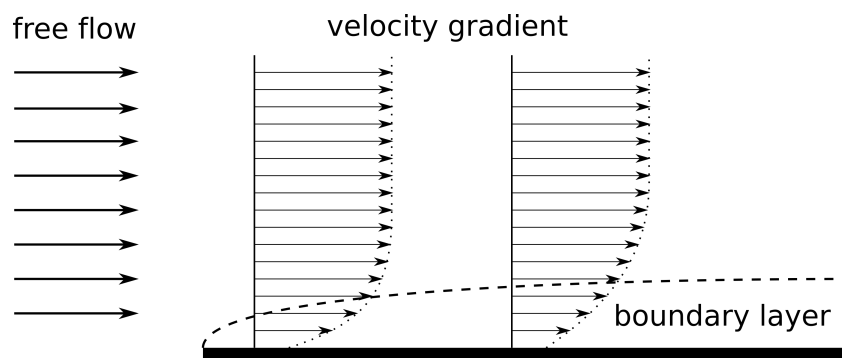


Figure 6. Velocity gradient in laminar flow.

When a precursor molecule reaches the substrate, it can be adsorbed on the surface physically or chemically, based on the binding modalities. Subsequently, decomposition of the precursor and diffusion of the created fragments takes place. The most common decomposition mechanisms are dissociation of neutral ligands, heterolytic bond cleavage such as β -hydride-elimination and homolytic bond cleavage. Volatile decomposition products desorb from the surface and are transported out of the reactor after diffusing through the boundary layer. In order to grow a new layer on the substrate a higher adsorption than desorption rate is necessary. When atoms, that are diffusing over the surface, are colliding, multi-atom aggregates can form, which serve as nucleation seeds. This is called homogeneous nucleation. Heterogeneous nucleation on the other hand takes place at structural defects of the substrate.

At first, the small nucleation seeds are metastable due to an energetically unfavorable large surface to bulk ratio and will only form stable aggregates when they surpass a critical radius. During the secondary nucleation phase, several nucleation seed coalesce to larger aggregates and formed voids are filled through the accretion of additional atoms. The growth rate is determined by the slowest single step during the described process and is influenced by the substrate temperature, reactor pressure and precursor feed.

When a material is grown on a different substrate (heteroepitaxy), a distinction between three growth modes can be made (Figure 7). Which mode applies, depends on the different interactions between substrate and deposited atoms as well as the interactions among the deposited atoms.

When the adsorption energy on the substrate and the deposited material are similar, monolayer after monolayer grows on the substrate. This is called the *Frank-van-der-Merwe* growth. In the *Volmer-Weber* growth, interactions between the adatoms is stronger than between the adatoms and the substrate, which leads to the formation of three-dimensional islands and thereby rough films. In an intermediary process, the *Stranski-Krastanow* growth, the formation of islands is favored over monolayers above a critical layer thickness, which leads to both 2D and 3D structures.

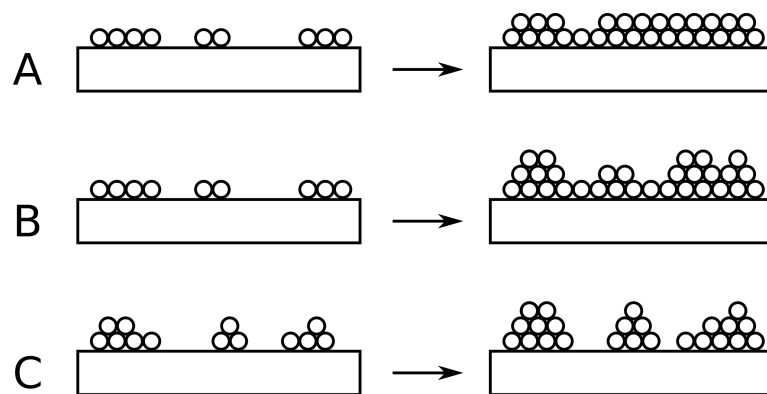


Figure 7. Growth modes in CVD: *Frank-van-der-Merwe* (A), *Stranski-Krastanow* (B) and *Volmer-Weber* (B).

The temperature of the substrate has a major impact on the film growth (Figure 8). At low temperatures, the so-called kinetically controlled regime, the growth rate depends on the decomposition rate of the precursors on the substrates surface. The decomposition rate of the precursor molecules can be described by the simple Arrhenius equation.

$$k = A \cdot e^{\frac{-E_a}{RT}}$$

With rising temperature, the rate of precursor decomposition also rises, leading to higher growth rates within the kinetically-controlled region, until the growth rate reaches a maximum and stays constant. In this second section, the so-called

diffusion-controlled regime, nearly all precursor molecules that reach the substrate decompose. The growth rate is limited only by the diffusion rates of the precursor molecules through the boundary layer. If the temperature increases further, more desorption and gas-phase reactions take place, thus reducing the growth rate with rising temperature.^[59]

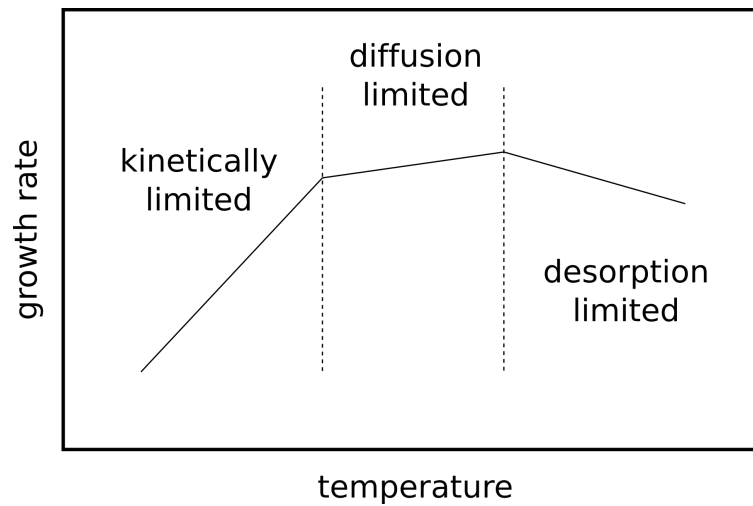


Figure 8. Growth rate as a function of substrate temperature.

3.3 Ni/Ga Intermetallics

In the Ni/Ga system, ten different phases were identified and characterized to date: Ni₃Ga, Ni₂Ga, Ni₅Ga₃, Ni₃Ga₂ (HT), Ni₃Ga₂ (LT), NiGa, Ni₃Ga₄, Ni₂Ga₃, Ni₃Ga₇ and NiGa₅.^[60,61]

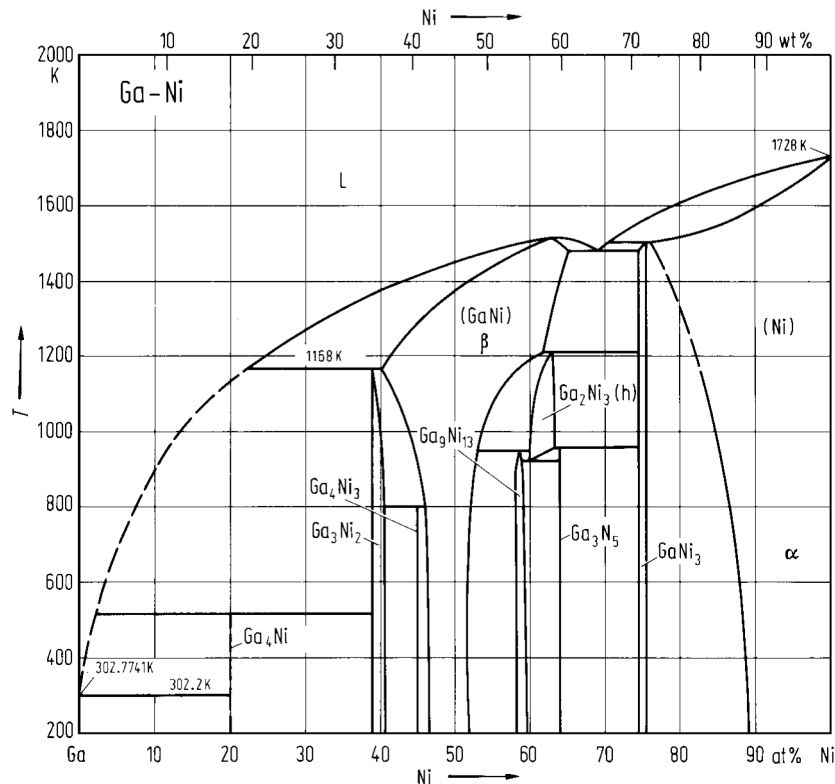


Figure 9. Phase diagram of Nickel-Gallium.^[62]

One eutectic point is observed at the composition Ni₆₉Ga₄₁. The β -NiGa phase crystallizes in the cubic $Pm\bar{3}m$ space group (CsCl structure) with the lattice parameter $a = 2.8949 \text{ \AA}$ and was observed for a composition of Ni_xGa_{1-x} over the range $0.42 < x < 0.69$.^[61,63] The β -NiGa phase represents the thermodynamic minimum with a Gibbs free energy of formation $\Delta G = -32 \text{ kJ/mol}$ at 1100 K.^[64] The electrical resistivity at room-temperature of $3.7 \cdot 10^{-8} \text{ } \Omega\text{m}$ makes it a good conductor and electrode material.^[65]

The α -Ni₃Ga phase also crystallizes in the $Pm\bar{3}m$ space group (AuCu₃ structure) with the lattice parameter $a = 3.59 \text{ \AA}$ (Ni₇₂Ga₂₈) and was observed for a composition of Ni_xGa_{1-x} over the range $0.75 < x < 0.89$.^[66]

Several approaches have been made to synthesize Ni/Ga intermetallics for different applications.

The synthesis of Ni/Ga bulk materials has been realized via induction melting and arc melting from the elements under inert atmosphere.^[67,68] Thin films of NiGa and Ni₂Ga₃ were grown via molecular-beam epitaxy onto GaAs with the intention of producing a semiconductor/metal/semiconductor structure for an application in electronics.^[69]

Nanoparticles of Ni/Ga intermetallics have been used as alkyne semihydrogenation catalysts and were synthesized via hydrogenation of layered double hydroxides^[70] or via microwave induced co-pyrolysis of metal organic precursors in ionic liquids.^[71] These preparation techniques, however, led to materials with high concentrations of residual oxygen and carbon.

Supported Ni/Ga intermetallics were prepared via incipient wetness impregnation of the nitrate solutions on silica and subsequent reduction with H₂. Those samples of Ni₅Ga₃ showed a high activity in the thermal hydrogenation of CO₂ to MeOH, which was in the same range as the industrial Cu/ZnO/Al₂O₃ catalyst.^[36]

3.4 Computational Chemistry

3.4.1 Schrödinger Equation

In 1933, the Nobel Prize in Physics was granted to *Erwin Schrödinger* and *Paul Dirac* “for the discovery of new productive forms of atomic theory”. This discovery is condensed in the time dependent *Schrödinger equation*:

$$\hat{H}|\Psi(r, t)\rangle = i\hbar \frac{\partial}{\partial t} |\Psi(r, t)\rangle$$

Or in its simplified time-independent form:

$$\hat{H}\Psi = E\Psi$$

Although its simple form, this equation is a complete but very complex description of non-relativistic systems and thus most of chemistry. *Paul Dirac* described it like this: “The underlying physical laws necessary for the mathematical theory of a large part of physics and the whole of chemistry are thus completely known, and the difficulty is only that the exact application of these laws leads to equations much too complicated to be soluble.”^[72]

This becomes apparent when the *Hamiltonian* operator \hat{H} and wavefunction Ψ are examined in detail. The exact definition of the Hamiltonian depends on the system that is described by the Schrödinger equation. For example, in case of the well-known particle in a box or the harmonic oscillator the Hamiltonian has a simple form and the Schrödinger equation can be solved exactly, but for chemically relevant systems it becomes more complex.

In real systems, the *Born-Oppenheimer* approximation can be applied in order to simplify the Schrödinger equation, which states that the movement in a system can be separated into an electronic and a nuclear part. Since electrons move much faster than nuclei, their equation of movement can be solved considering a static ensemble of nuclei. In a second step, the result can be used as a potential in a *Schrödinger equation* containing only the nuclear kinetic energy.^[73]

In a system, where multiple electrons are interacting with multiple nuclei, a description of the Hamiltonian is:

$$\left[-\frac{\hbar^2}{2m_e} \sum_{i=1}^N \nabla_i^2 + \sum_{i=1}^N V(r_i) + \sum_{i=1}^N \sum_{j<i}^N U(r_i, r_j) \right] \Psi = E\Psi$$

Here, m_e is the electron mass and ∇^2 is the *Laplacian operator*. The three terms describe the kinetic energy of each electron, the Coulomb interactions between each electron and the collection of nuclei, and the Coulomb interaction between the electrons, respectively.^[74]

For this Hamiltonian, Ψ is the electronic wavefunction, which is a $3N$ -dimensional function, based on all spatial coordinates of every electron in the system.

The electron-electron interaction term makes it a multi-body problem that cannot be solved analytically. Therefore, in the field of quantum chemistry many methods have been developed in order to solve the Schrödinger equation numerically by approximating Ψ and \hat{H} (e.g. Hartree-Fock, perturbation theory, coupled cluster, ...). These techniques rely on systematic approximations, so that a hierarchy of methods is developed which increase in accuracy through the addition of complexity. Naturally, these methods tend to get more computationally intense with rising complexity, limiting the applicable system size.^[75]

3.4.2 Electron Density

The wavefunction provides a fundamental description of an electronic system, but it is not an observable in nature. What can be observed, is only the probability of an electron occupying a certain position in space. The spatial probability of all electrons N_e summed up can be described as electron density $n(\vec{r})$.

$$n(\vec{r}) = N \int_{\mathbb{R}^3} \dots \int_{\mathbb{R}^3} |\Psi(\vec{r}, \vec{r}_2, \dots, \vec{r}_{N_e})|^2 d\vec{r}_2 \dots d\vec{r}_{N_e}$$

This description of an electronic system based on electron density rather than the electronic wavefunction reduces the problem with $3N$ dimensions down to one with only three, making it more applicable for larger systems.

The theoretical justification of *density functional theory* (DFT) is based on two theorems provided by *Hohenberg* and *Kohn* in 1964.^[76] The first theorem proves that the ground-state energy is a functional of the electron density, meaning that the electron density determines all ground-state properties of a system, including energy and wave function. Although it states that there is a functional of the energy density that can be used to solve the Schrödinger equation, it is not specified how it can be determined exactly or even what form it has. The second theorem defines an important property of this functional. The true electron density, corresponding to the full solution of the Schrödinger equation, is defined as the electron density that minimizes the energy of the overall functional. This variational approach is used in practice numerically with approximate forms of the functional.^[74]

3.4.3 Kohn-Sham Equations

The functional described by the *Hohenberg-Kohn theorem* can be written as an ensemble of non-interacting one-electron equations in an effective potential function that results in the same electron density like the system with interacting electrons. Those N one-electron functions are called *Kohn-Sham functions* and are much easier to solve than the corresponding N -electron Schrödinger equation.^[77]

The one-electron energy functional $E(\Psi_i)$ can now be expressed in form of an analytically describable term $E_{known}(\Psi_i)$ and the exchange-correlation term $E_{XC}(\Psi_i)$.

$$E(\Psi_i) = E_{known}(\Psi_i) + E_{XC}(\Psi_i)$$

In its full form, the Kohn-Sham equations consist of the electron kinetic energies, the Coulomb interactions between an electron and the collection of nuclei $V(r)$, the Hartree potential $V_H(r)$ and the exchange-correlation potential $V_{XC}(r)$.

$$\left[-\frac{\hbar^2}{2m} \nabla^2 + V(r) + V_H(r) + V_{XC}(r) \right] \Psi_i(r) = E_i \Psi_i(r)$$

The Hartree potential $V_H(r)$ describes the Coulomb interactions between the described electron and the total electron density, defined by all considered electrons.

$$V_H(r) = e^2 \int \frac{n(r')}{|r - r'|} d^3r'$$

At one point in the calculation, the Coulomb interaction between the described electron and itself is considered, but because it is part of the total electron density, this self-interaction is incorrect from a physical standpoint. Compensations for the self-interaction and other effects (e.g. *Pauli-repulsion*, *van-der-Waals forces*) are summarized in the exchange-correlation potential $V_{XC}(r)$. The Kohn-Sham equations do not possess an inherent physical meaning but are often used in practice to approximate actual electronic states. In order to find the electron density with the lowest energy, an iterative procedure is used in which an initial trial density is chosen based on parametrized profiles, the Kohn-Sham equations are solved using the trial density, the electron density is calculated based on this solution and compared to the initial electron density. If they are equal, this is the ground-state electron density. If they are not equal, both densities are mixed in a specified way to obtain a new trial density and restart the process. This is known as the *self-consistent field* (SCF) process to determine the ground-state electron density of a given set of atomic coordinates.^[74]

In order to optimize the atomic coordinates to a local energy minimum, a similar iterative process is applied. In a first step an initial guess for the atomic coordinates is supplied. During the second step the ground-state energy of this system is calculated using the SCF process. In the third step the forces on each atomic nucleus is calculated via the *Hellman-Feynman theorem*.^[78] If the calculated forces are sufficiently small, then a local minimum is found. If not, the positions of the nuclei are changed along their force-trajectories and a new geometry optimization cycle is started with the new coordinates.

3.4.4 Exchange-Correlation Functional

In the *Kohn-Sham* formalism, the many-electron problem has not been solved but was transferred to the exchange-correlation function $V_{XC}(r)$.

It has been proven impossible to find the true $V_{XC}(r)$ for all but very simple systems^[79], although hundreds of different approximations have been developed to this day.^[77,80–84]

Four commonly used approximation techniques are the *localized density approximation* (LDA), the *general gradient approximation* (GGA), *meta-GGA functionals* and the *hybrid functionals*. In LDA functionals it is assumed that $V_{XC}(r)$ is a function of the electron density $n(r)$ at only this point and not at all points. This approach often delivers sufficient results, especially when the electron density is similar over the whole system, like for electrons in the conduction band of metals. But for inhomogeneous systems like molecules, the bond strengths are usually overestimated. In GGA functionals, not only the electron density at these coordinates, but also its derivation with respect to the location is considered. With this approach, good results have been achieved with respect to molecular geometries and ground-state energies. The *revised Perdew-Burke-Ernzerhof* (RPBE) functional, that was used during this project, is part of this family.^[85] With meta-GGAs, also the second derivative of the electron density with respect to the location was introduced as a factor, as a hierarchic expansion. In hybrid functionals, only part of the exchange-correlation potential is calculated according to DFT (e.g. GGA) and another part is calculated as exchange energy of the Kohn-Sham functionals like in the Hartree-Fock method. This results in generally more accurate results for molecules than pure GGA functionals. Prominent representative of this class is the *Becke, 3-parameter, Lee-Yang-Parr* (B3LYP) functional.^[86]

3.4.5 Basis Sets

Basis sets are mathematical, approximative representations of the electronic wavefunctions, in order to convert the differential equations of the quantum mechanical model into efficiently computer-treatable algebraic equations.

A basis set can either be composed of atomic orbitals or plane waves. Plane waves are used in periodic boundary approaches, while atomic orbitals are treated in linear combinations to yield an approximation of the molecular wavefunction.

Physically most meaningful are the *Slater-type orbitals* (STOs), which are solutions to the Schrödinger equation of hydrogen-like atoms. However, STOs are difficult to treat computationally and can be approximated by *gaussian-type orbitals* (GTOs). Several different GTOs have been published with typically hierarchical increasing size and other modifications. A common modification is the addition of polarization functions for the electron density of the atom in molecules, since the minimal basis set only describes the gas-phase atom sufficiently well. Another common modification is the addition of diffuse functions for the treatment of long-range forces, especially important for anions and dipole moments.^[87]

Similar to the exchange-correlation functional, several different basis sets have been constructed to be used in specific scenarios.

3.4.6 Limitations of DFT

The concept of DFT provides an efficient approach for solving the Schrödinger equation, but some fundamental limitations remain.

The Hohenberg-Kohn theorems only prove that the ground-state energy is a functional of the electron density. Therefore, events and properties that are based on excited states, such as UV-VIS spectra and X-ray absorption are not well described by DFT and need advanced methods like time-dependent DFT.^[88]

Another inaccuracy of DFT are the Kohn-Sham orbitals, which are not equivalent to the true wavefunction and only describe auxiliary systems with non-interacting electrons. Thus, the Kohn-Sham eigenvalues do not equal the real eigenvalues of the system and its electronic structure is not represented perfectly by the one obtained from DFT.

Despite numerous attempts over the last decades, the true exchange-correlation functional is unknown. Many different approximations have been developed and have each been optimized for specific fields only.^[89] Some might excel for the description of crystalline structures, while others are more accurate for the treatment of molecules, like the widely used B3LYP.^[90,91] This proved to be a challenge in heterogeneous catalysis, since the catalytic properties are determined by interactions between two classes of systems, namely molecules and solids. In response, new functionals have been developed that are optimized for surface properties. The RPBE functional was one of the first and most successful in this field and is therefore applied in this thesis.^[85]

Many newly developed methods include more reference data to improve general accuracy. However, the fact that even meta-GGA functionals show comparably large errors when fitted against wide data sets, indicate that the approach of adding additional information is likely not to yield the true exchange-correlation functional.^[92] At the same time, the computational cost of improving on the exchange-correlation functional may exceed the cost of more sophisticated methods than DFT, rendering its application impractical.

Despite the mentioned limitations, DFT is the most used method in practical applications, due to its superior accuracy/cost ratio and general robustness.

3.5 Computational Heterogeneous Catalysis

3.5.1 Quantities of Interest

The fundamental property of a system, which guides catalytic processes, is the *potential energy surface* (PES). This is a $3N$ dimensional surface, with N being the number of atoms in the system, and can be reduced to a more intuitive two-dimensional representation by connecting two local minima (Figure 10).

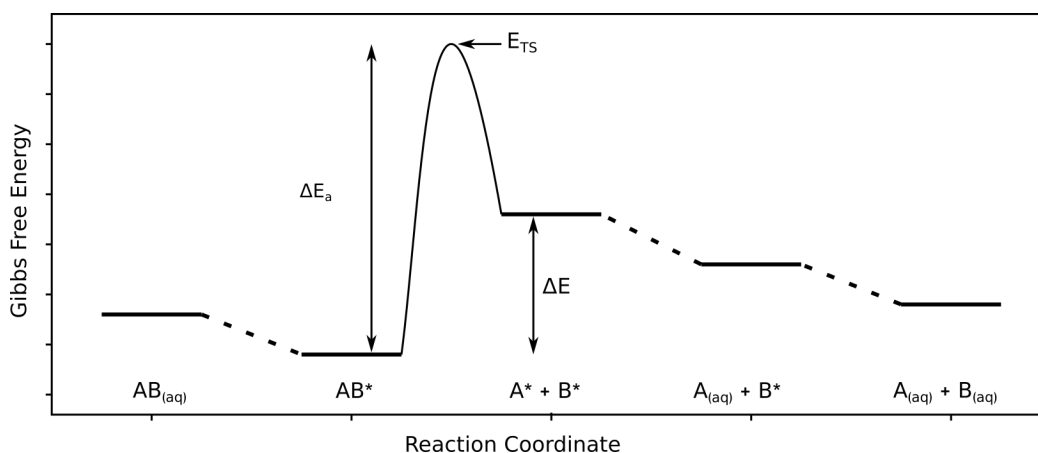


Figure 10. Two-dimensional representation of the potential energy surface of a reaction $AB \rightarrow A + B$ on a catalytic surface. The * denotes species adsorbed to the surface. Reaction energy ΔE , activation energy ΔE_a and transition state energy E_{TS} are labeled for the elementary step $AB^* \rightarrow A^* + B^*$.

Those minima correspond to stable reactants, products or intermediates of the reaction. The most relevant connecting path is the one with the lowest energy barrier, and the point on this path with the highest energy is referred to as the transition state. Therefore, the energies of all participating reactants, products, intermediates and transition states provide an excellent approximation of the full energy surface.

Activation energies E_a determine the rate of a reaction k , following the *Arrhenius equation*:

$$k = A \cdot e^{\frac{-E_a}{RT}}$$

with the pre-exponential factor A , universal gas constant R and temperature T . Since the activation energy influences the reaction rate exponentially, a small change in E_a has a large influence on the rate. Therefore, it is crucial to exactly determine the activation energy, if an accurate kinetical description is required.

The macroscopic observable free energy ΔG of a reaction is a result of the sum over the free energies of all elementary steps ΔG_E .

$$\Delta G = \sum \Delta G_E$$

Gibbs free energy comprises the change in enthalpy ΔH and entropy ΔS of a reaction multiplied with the temperature T .

$$\Delta G = \Delta H - T\Delta S$$

Whilst for many stable molecules ΔH and ΔS have been measured experimentally and can be found in numerous databases and handbooks, measuring the energies of adsorbates and transition states is much more challenging.

There are a few techniques to determine those quantities directly, such as molecular beam impingement, calorimetry and temperature-programmed desorption/reaction. Although those approaches delivered some highly accurate measurements for adsorption energies, they are restricted to stable molecules, well-defined samples and exclude environmental factors.^[93]

A second approach to obtain energetics experimentally is to derive them from measured catalytic properties based on a microkinetic model. Here, the change in catalytic rate is observed with respect to a variation in parameters like temperature and pressure. A model containing these parameters is then fitted against the experimental data. This approach, however, requires a number of assumptions, such as the reaction mechanism, and in complex systems often leads to multiple solutions that cannot be distinguished. Nevertheless, it is often applied successfully.^[94,95]

The fundamental problem in measuring these energies is based on heterogeneous catalysis being an intrinsically local phenomenon that takes place at active sites and not the entire surface. On the other hand, macroscopic measurements are always an average over many active sites and also inactive sites which cannot be distinguished easily, nor is there a trivial way to isolate them, like in molecular catalysis. The active sites often are high-energy surfaces, steps, edges, defects or impurities, which represent only a small fraction of all abundant surface atoms. Most relevant properties, such as rates and selectivity, depend exponentially on the activation energies in the system, so that a site with a slightly lower activation barrier may exhibit rates which are orders of magnitude higher than those of the other sites. For this reason, even small amounts of active sites can dominate the observed activity.

Due to their local nature and since the active sites usually consist of only a few atoms, quantum mechanical methods can be used to treat catalytic processes computationally. Based on the local description of all relevant adsorbed intermediates and the calculation of their relative energies as well as transition-states, the activity of different materials and surfaces can be derived from this approach.

3.5.2 DFT in Practice

In order to understand the complex reduction network of CO₂ to various products, a substantial number of energies are necessary. If a few energies are unobtainable experimentally, which is usually the case even for moderately complex systems, the catalytic rate might not be explained conclusively.

At this point, quantum mechanics can provide a systematic description of all relevant parameters, such as reaction energies and activation energies. The most efficient method for obtaining such a large number of energies in a foreseeable time period is DFT. In contrast to other methods like molecular mechanics or coupled-cluster theory, DFT provides the best accuracy/time ratio for a project with the need for several hundreds of energies.^[74]

With an informed choice of a specialized exchange-correlation functional, DFT often yields accurate results which are in good agreement with experimental data.^[85]

The lack of *London* dispersion interactions in standard DFT can lead to unrealistic results, since they are the dominant part of long-range interactions. Especially for larger systems with weak interactions, like molecules adsorbed on surfaces, dispersion interactions account for the main part of the attractive forces. Therefore, several methods have been developed to include dispersion interactions. For example dispersion-corrected DFT, parameterized functionals or dispersion-correction potentials.^[96] A widely used type of dispersion-corrected DFT is *Grimme's* DFT-D3 approach, which includes attractive C_6/R^6 terms with atom-pairwise specific dispersion coefficients and cutoff radii, computed from first principles.^[97] This is a convenient way of adding dispersion corrections to the calculation, without adding computational cost.

In order to realistically treat the electrochemical reduction of CO_2 , solvent effects need to be considered in the calculations. This can be accomplished by either including explicit solvent molecules around the active site, which results in an accurate treatment at the cost of substantially added computation time, introduced by the additional degrees of freedom. A second approach is the treatment of the solvent through the introduction of an implicit solvation model, for example the *conductor-like polarizable continuum model* (CPCM).^[98] Here, the solvent is represented by a dielectric polarizable continuum and the electrode model is placed in a cavity that possesses its approximate shape. This way, the electronic effects of the solvent are considered, but not its explicit interactions. Although this model is less accurate, it excels at computation time and, even more important for the energetic evaluation of a reaction network, makes calculations of different intermediates directly comparable.

The exact treatment of an electrode with the dimensions of $1 \cdot 1 \cdot 0.1$ cm would require a system with an atom count of approx. 10^{23} , which is impossible to handle with today's computational resources. Instead, a model system is required to treat surfaces computationally. Two approaches are available to generate such a model: cluster and periodic. *Plane-wave periodic boundary* (PB) models reduce the treated atom count through periodic expansion of a central unit in all special directions. Interatomic forces are then calculated under inclusion of the atoms in a neighboring cell. Advantages of this approach are the relatively small number of explicitly treated atoms and a good physical representation of the crystal lattice. On the other hand, PB calculations also result in periodic plane-wave orbitals, which differ significantly from localized orbitals and complicate property calculations. *Quantum cluster* calculations deliver localized orbitals, since they treat the arrangement of atoms like one molecule. Main difficulty here is the property convergence with variation in cluster dimensions. Since borders of the cluster are anomalies, which also effect the inner atoms, relatively large cluster sizes must be chosen to ensure property convergence at the active site. Oftentimes geometrical constraints are placed on the outermost atoms to mimic the bulk structure.^[99]

4 Evaluation Part I: Mechanistic Investigations

Identifying the mechanism, which takes place on the electrode's surface during electrochemical CO₂ reduction, is crucial for the conscious development of improved catalysts. The evaluation of a network of possible intermediates by means of DFT energies provides a systematic and efficient view of the catalytic mechanism, when compared to experimental results. Such an evaluation can reduce the complexity of such a broad network with up to 100 intermediates to the important steps, which determine product selectivity and activity of the catalyst.

4.1 Model System

4.1.1 Construction of Model Clusters and Pre-Optimization

In order to construct atomic clusters of the desired materials, their structures were obtained from crystallographic data, reported in literature.^[100]

Based on those structures, super cells with the appropriate surface exposed were generated in the *Avogadro* 1.2.0 program^[101] from which the intended clusters were cut out.

In a first benchmark test, several clusters with different sizes (Figure 11) were used to calculate the exemplary reaction energy of the hydrogenation of *CO to *CHO. This reaction was chosen, because it involves only two and three atoms which geometry needs to be optimized and in addition this reaction was proposed to play an important role in the CO₂RR on some materials.^[55,102,103]

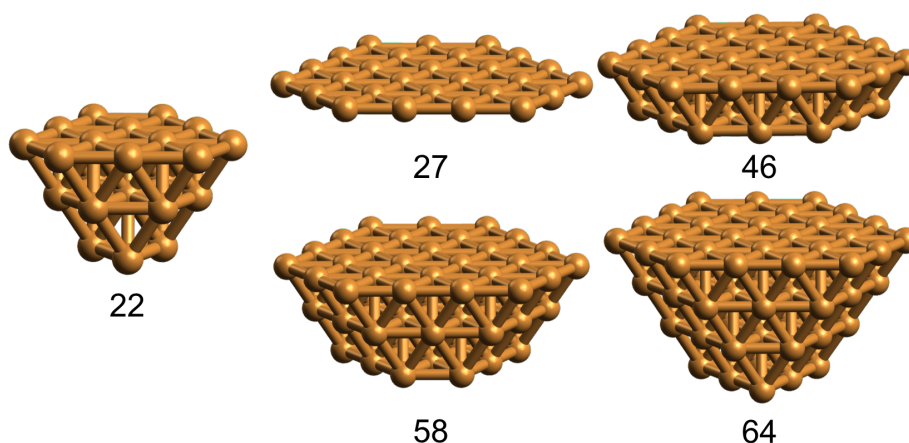


Figure 11. Cluster sizes used in the benchmark test with their respective atom count.

During the benchmark test, geometries of the clusters were fixed and the geometry of the adsorbates was allowed to relax freely, in order to avoid structural influences and only observe energy convergence based on cluster size. The reaction energy was found to converge within the limit of 1 kJ/mol at the 58-atom cluster (Figure 12). This cluster is characterized by two layers of atoms surrounding the central coordination site in all directions.

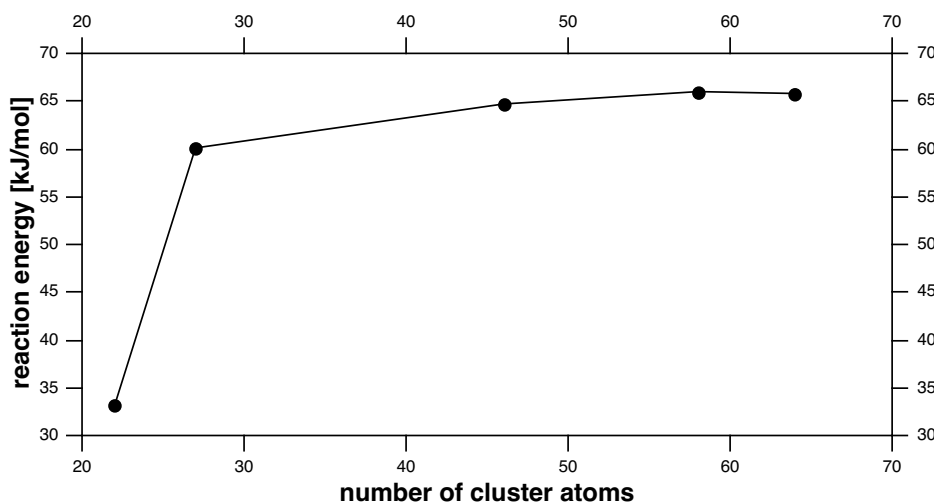


Figure 12. Reaction energies of the hydrogenation of *CO to *CHO on different cluster sizes.

Therefore, the cluster sizes in the production runs were chosen so that the central 5-atom (211)/(210) or 4-atom (111)/(100) motive was surrounded by two layers of atoms, resulting in 64-65 atoms per cluster (82 in case of Cu(100)).

For the main part of the investigations, stepped (211) or (210) surfaces were chosen, because under-coordinated sites are known for their higher catalytic activity^[104] and also stepped surfaces allow for the coordination of adsorbates on flat or stepped sites, thus raising the possibility to find the optimal minimum energy path (Figure 13).



Figure 13. Exemplary stepped surface clusters for the investigation of Cu, NiGa and Ni₃Ga.

In order to mimic the structural constraints of a physical surface, the outermost layer of atoms was confined in space and all other atoms were allowed to relax freely during geometry optimizations. Since some of the investigated materials were expected to exhibit unpaired electrons, the geometry of all clean clusters was optimized with a varying set of multiplicities, in order to find the energetic minimum (Table 2).

Table 2. Multiplicities at which minimal energies were observed for the materials and surfaces used in this study. One of the two denoted multiplicities was chosen based on the presence of unpaired electrons in each intermediate. The addition “mix/Ni” indicates whether the surface step consists of alternating Ni and Ga or of pure Ni.

Material	Multiplicity S
Cu(211)	1 / 2
Cu(100)	3 / 4
Cu(111)	2 / 3
NiGa(210)	7 / 8
Ni ₃ Ga(211)-mix	11 / 12
Ni ₃ Ga(211)-Ni	17 / 18

NiAl(210)	7 / 8
Ni ₃ Al(211)	4 / 5
Ni(211)	51 / 52
Zn(111)	1 / 2
CuNi(211)	24 / 25
CuZn(210)	3 / 4

In case of the Cu(211) cluster, the *single point energy* (SPE) rises in a parabolic fashion with an increased multiplicity. Depending on whether the adsorbate possesses an unpaired electron or not, a multiplicity of $S = 1$ or $S = 2$ was chosen.

NiGa(210) shows a flat energy profile for varying multiplicities. The energy minimum lays at $S = 8$ with a steep increase to higher and a flat increase to lower multiplicities. Therefore, a multiplicity of $S = 7$ or $S = 8$ was chosen. In case of Ni₃Ga(211), the lowest energy was observed at $S = 11$. The increase in energy towards $S = 9$ was higher (+8 kJ/mol) than towards $S = 13$ (+2.6 kJ/mol). Therefore $S = 11$ or $S = 12$ was chosen.

In general, near the energetic minimum the difference in energy between two multiplicities is below 5 kJ/mol, so that a second evaluation for each individual intermediate is not necessary.

In the following discussion of reaction paths and the evaluation of the results, species that are adsorbed on a surface are denoted with an asterisk (*).

Initially the surface is covered by water, which is replaced by CO₂ in a first step. The first hydrogenation reaction takes place at the oxygen center, forming a carboxyl (*COOH) intermediate. From there either formic acid (HCOOH) can be produced, which represents the product with the lowest electron intake (2 e⁻), or *COOH can be hydrogenated at the hydroxy group, which results in *CO after dehydration.

From this point forward several pathways open up, which define product selectivity based on their relative energies. If desorption is favored over further reduction, carbon monoxide is released, limiting the product scope to formic acid and CO. However, when CO is bound strongly enough, hydrogenation reactions can take place either at the carbon or oxygen center, opening a network of intermediates. If oxygen hydrogenation is generally preferred, hydrocarbon species (*CH, *CH₂, *CH₃) are formed on the surface. Those hydrocarbons can either dimerize to yield acetylene, ethene or ethane, or they can be fully reduced to yield methane. On the other hand, when carbon hydrogenation is favored, the first intermediate is an aldehyde (*CHO), followed by the formation of adsorbed formaldehyde (*OCH₂), which is subsequently reduced to methoxide (*OCH₃), from which methanol or methane can be formed via hydrogenation of the oxygen or carbon center, respectively.

In theory, dimerization of two C₁ species can occur at any point along the C₁ pathway, but experiments indicate that – at least on copper – dimerization takes place at the *CO stage or the following stage. This will be evaluated in detail later on. Dimerization of two *CO can be used as a valid starting point. If subsequent hydrogenation takes place at one oxygen atom, the reaction proceeds through ketene-like intermediates. Hydrogenation of the formed *CHCO can take place at the terminal carbon atom and thereby adsorbed ethenone is formed, which is expected to easily get hydrated under operating conditions to acetic acid (CH₃COOH). However, if *CHCO is hydrogenated at the central carbon atom, the reaction will lead to acetaldehyde as a first stable C₂ intermediate. Subsequent reduction of acetaldehyde can yield ethanol as well as ethane.

Coming back to the *CO-dimer, hydrogenation at a carbon atom would lead to *CHOCO, which is followed by glyoxal or *COCH₂O. In both cases, the following hydrogenation steps can occur along a broad network of intermediates, leading to all possible C₂ products with the most reduced products being ethylene and ethane.

4.2 Copper

4.2.1 Introduction to CO₂RR on Copper

Cu is unique in its ability to catalyze the electrochemical CO₂RR to hydrocarbons, alcohols and several other organic molecules with up to four carbon atoms at reasonable Faradaic efficiencies. Until now, 20 different products have been detected.^[50–52] Most other pure metals produce only partly reduced products such as formic acid or CO, or they do not convert CO₂ in favor of the competing HER.^[105]

Although its capabilities, drawbacks of the application of Cu are the poor product selectivity, low Faradaic efficiencies and high overpotentials, which are necessary to favor highly reduced products, such as methane, ethylene or ethanol. Several approaches have been made to overcome those drawbacks. Oxide derived copper for example lowers the onset potential and raises the selectivity towards C₂H₄ and EtOH.^[106,107] Copper nanoparticles^[108] showed enhanced methanation activity compared to polycrystalline copper, whereas copper nanocubes^[109,110] exhibit a high selectivity towards C₂H₄.

As a general trend, the ratio between C₁ and C₂/C₃ products is strongly influenced by the surface morphology. It has been shown that the formation of CH₄ is favored on low-energy surfaces like Cu(111) and that the pathway towards C₂H₄ and EtOH opens at lower potentials on high-energy surfaces like Cu(100) or Cu(211).^[107,109–112] Detailed views will be provided in the following chapters, at the appropriate positions.

Several DFT studies have been conducted, in order to illuminate the CO₂RR from a theoretical point of view. Due to the complexity of the CO₂RR, however, most studies focused on a partial area of the whole picture. Some described only the mechanism towards C₁ products, such as formic acid^[113–115] or CH₄^[116–119] (with inclusion of kinetics^[120–123]), whereas others include C₂ products, but limit their

investigation either to an incomplete variety of intermediates^[124,125], to the main products^[126,127] or to the C-C coupling step^[128,129].

All mechanisms proposed in these studies have been taken into consideration for the following evaluation, providing a comprehensive view of the reaction network.

4.2.2 Cluster Model

All intermediates presented in Scheme 1 were placed on a Cu(211) and their geometries were optimized with the outermost layer of the cluster constrained in position (Figure 14).

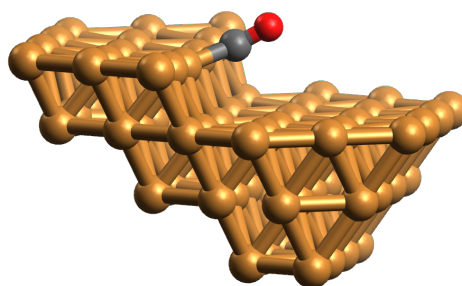


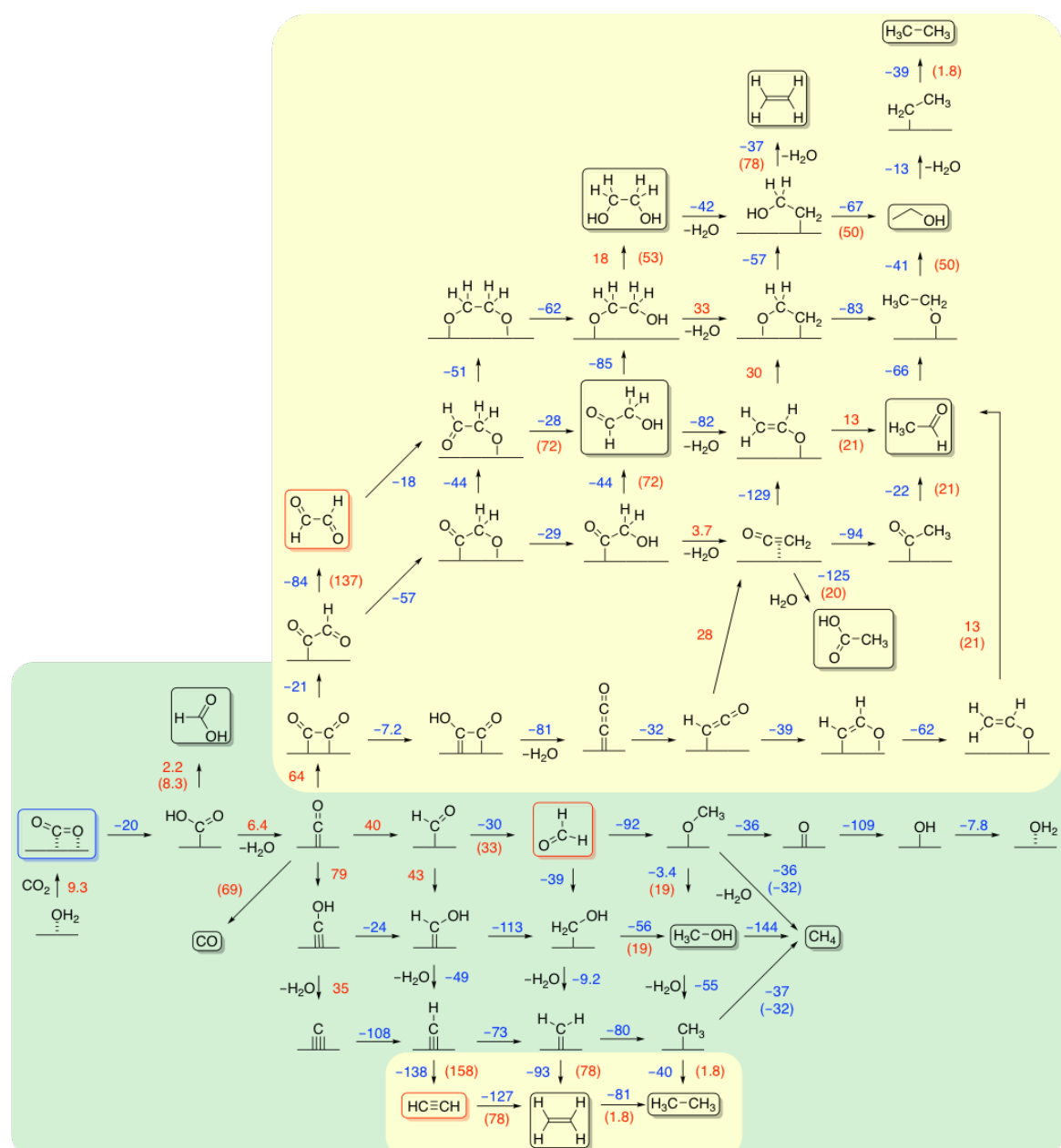
Figure 14. Model system for adsorbed CO on Cu(211).

The resulting SPE was compared to the neighboring intermediate in order to obtain the reaction energy following the basic equation

$$\Delta E = E_{product} - E_{educt}$$

The addition of hydrogen atoms was considered, based on the CHE model, as half the energy of a H₂ molecule. The influence of the surrounding solvent was treated implicitly with the CPCM approach.^[98] This model provides an effective simplification for an extensive screening study, without the need for addition of explicit solvent molecules.

All reaction and desorption energies at a potential of 0 V are depicted in Scheme 2. Desorption energies were calculated using the energy differences between the adsorbed product and adsorbed water, with respect to their corresponding energies in solution. For C₁ products, one adsorbed water molecule was used as reference, while for C₂ products, two water molecules were used, in order to account for the displacement of one water molecule by one CO₂ in the first place.



Scheme 2. Reaction network on Cu(211) with all reaction energies in kJ/mol. Desorption energies are denoted in brackets. C₁ and C₂ pathways are highlighted in green and yellow, respectively. Stable products are framed. Products in red frames have not been observed experimentally.

4.2.3 C₁ Products

In the initial step, the surface adsorbed water molecule is displaced by CO₂ from solution at moderate +9.3 kJ/mol. Then the first hydrogenation at one oxygen center takes place, which is exothermic by –20 kJ/mol, forming a carboxylic acid *COOH. A direct dissociation into *CO and *O is more energy demanding, with a reaction energy of +67 kJ/mol and an activation energy of 77 kJ/mol. Also, this would eliminate the possibility to produce formic acid, which is a main product at low potentials on Cu.

The hydrogenation of *COOH to formic acid is almost thermoneutral, but exhibits a relatively high activation energy of 61 kJ/mol, thus favoring the formation of *CO under elimination of H₂O at a comparable reaction energy of +6.4 kJ/mol, especially at higher potentials.

*CO has been shown to be an intermediate in CH₄ as well as C₂H₄ production^[50,130] and is the most reduced product on many other electrode materials like Zn, Au and Pd.^[56] Following the formation of *CO, various pathways including hydrogenation reactions of either the carbon or oxygen atom or dimerization are possible. All possible reactions are uphill in energy, but hydrogenation of the carbon atom – the formation of *CHO – needs the least reaction energy of about +13 kJ/mol. The dissociation of *CO to *C and *O, as discussed in thermal catalysis, would require +213 kJ/mol and is therefore discarded as reasonable reaction path.^[131,132] The next hydrogenation reaction also takes place at the carbon atom, resulting in adsorbed formaldehyde *OCH₂. The following conversion can proceed via the carbon bound *CH₂OH or the oxygen bound methoxy *OCH₃ intermediate. Since those and all following steps are downhill in energy, the actual path strongly depends on the respective activation energies.

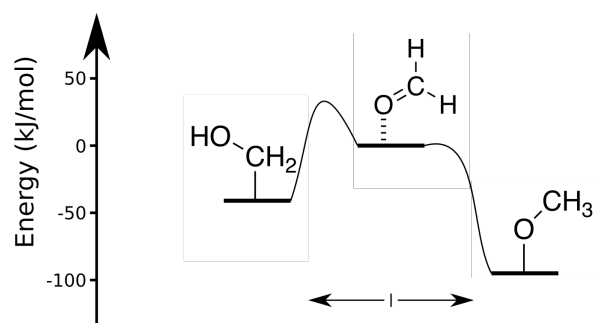


Figure 15. Energy diagram of the hydrogenation of adsorbed formaldehyde.

The hydrogenation at the carbon center was found to be more feasible than at the oxygen center, both thermodynamically and kinetically (Figure 15). The experimentally observed high selectivity towards CH_4 over CH_3OH is supported by two observations. First, the hydrogenation of the carbon atom of $^*\text{OCH}_3$ is thermodynamically more feasible than the hydrogenation of the oxygen (-36 kJ/mol vs. $+3.6 \text{ kJ/mol}$). Second, the further hydrogenation of adsorbed methanol yielding in $^*\text{CH}_4$ and $^*\text{OH}$ is highly exothermic (-144 kJ/mol). Even if methanol is formed, it would be reduced quickly to methane, also supported by an endothermic desorption of $+19 \text{ kJ/mol}$ for methanol compared to -32 kJ/mol in case of methane. The terminal oxide $^*\text{O}$, which is generated during methane formation, is subsequently reduced to $^*\text{OH}$ (-109 kJ/mol) and $^*\text{OH}_2$ (-7.8 kJ/mol), thus completing the catalytic cycle.

Activation energies of the one-dimensional PES hydrogenation reactions were assessed via bond-length scan of the involved O-H or C-H bonds in increments of maximum 0.1 \AA . The bond length scan can be seen as an upper limit of the activation energy, since the solvent environment was simulated with the CPCM approach and was not treated explicitly. Therefore, the direct hydrogenation/protonation from the surrounding water was neglected. It has been shown, that this treatment provides accurate results in case of carbon hydrogenation, but is often not the preferred mechanism in case of oxygen hydrogenation.^[133] Therefore, those activation energies are expected to be slightly overestimated by this approach.

quantities only, whereas C_2H_4 was found to be one of the main products.^[51,112] Also, the potential limiting step would be the same for CH_4 and C_2H_4 , which differs from observations made by *Schouten et al.*^[134] and *Gattrell et al.*^[130]. They proposed the formation of $*CHO$ to be the potential limiting step during CH_4 production, but towards C_2H_4 , a $*CO$ -dimer should be the key intermediate.

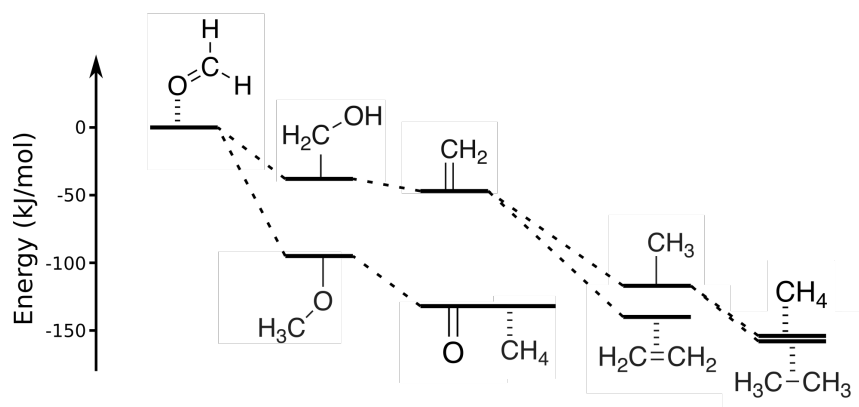


Figure 17. Energy diagram of two discussed pathways towards CH_4 , including the formation of C_2H_4 and C_2H_6 .

In this study, the hydrogenation of $*CO$ forming $*CHO$ was also found to be the potential limiting step during CH_4 formation with a reaction energy of +40 kJ/mol. This equals an expected onset potential for CH_4 production of -0.39 V. From this potential on, the reaction energies of all elementary steps become exothermic (Figure 18).

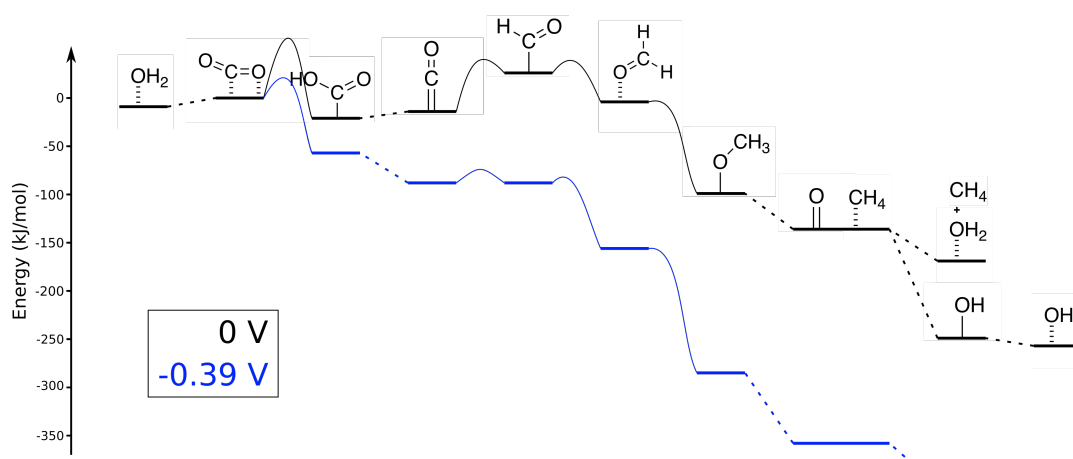


Figure 18. Energy diagram of the mechanism towards CH_4 at 0 V and at the expected onset potential of -0.39 V. Activation energies were extrapolated based on the *Bell-Evans-Polanyi* principle.^[135,136]

Comparing the reaction energies on the more active Cu(211) surface with the densely packed Cu(111) surface, energetic trends are similar favoring the same mechanistic path and the hydrogenation of *CO as potential limiting step. The major difference in activation can be reduced to the difference in CO binding energy. CO binds stronger to the surface of Cu(111) than Cu(211), which becomes apparent when comparing the relative energies of the prior and subsequent intermediates (Figure 19). The CO@Cu(111) lies -34 kJ/mol lower, whereas *COOH , *CHO and $\text{CO}_{(\text{aq})}$ are at similar energy levels, compared to Cu(211). This observation is also reflected in the calculated C-O bond lengths, which increase from free $\text{CO}_{(\text{aq})}$ (1.140 Å) over CO@Cu(211) (1.177 Å) to the strongly bound CO@Cu(111) (1.183 Å), as a result of the stronger back-bonding of the surface atoms into the π^* orbital of the adsorbed CO. In conjunction, the Mayer bond order decreases from 2.45 over 2.14 to 1.96, respectively.

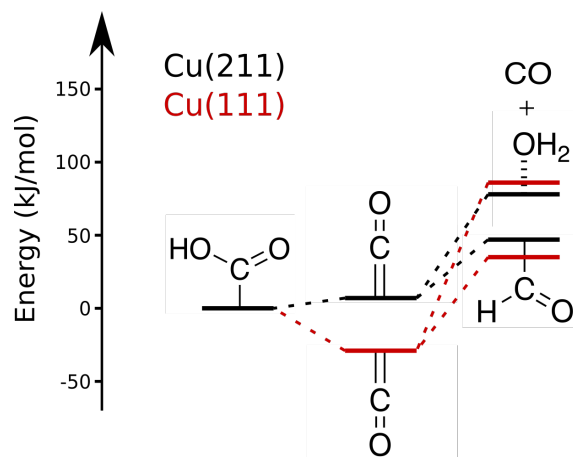


Figure 19. Energy diagram of the potential limiting step on Cu(211) and Cu(111).

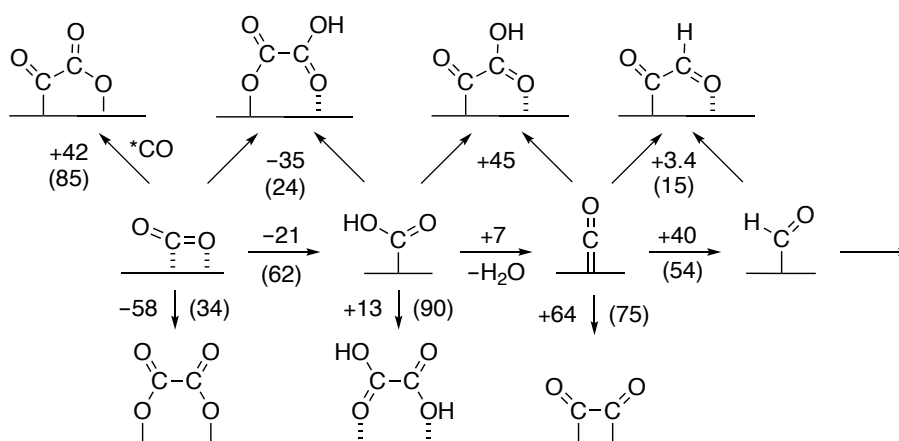
The stabilization of $^*\text{CO}$ on Cu(111) leads to a higher reaction energy of +62 kJ/mol during the following hydrogenation reaction. The higher activity of the Cu(211) surface can be explained by this destabilization of the $^*\text{CO}$ to some extent, but not too far so that the desorption of CO becomes feasible, which is the case for CO-producing materials such as Zn, Ag or Au.

The high selectivity of copper for CH_4 is based on the facile reduction of CO_2 to $^*\text{CO}$ and an intermediate binding energy of $^*\text{CO}$, which prevents the desorption of CO but on the other hand makes the reduction towards $^*\text{CHO}$ feasible at low overpotentials.

Key to higher efficiency of the CO_2RR on copper is the fine-tuning of the $^*\text{CHO}$ and especially the $^*\text{CO}$ adsorption energy. One successfully applied approach is the synthesis of materials with high concentrations of under-coordinated sites, which has been done by reduction of CuO or Cu_2O to porous Cu-surfaces^[107], or by the application of copper nanoparticles.^[108] Although this approach leads to a reduction in overpotential, in most cases also the selectivity for CH_4 is reduced in favor of products containing two or more carbon atoms such as ethylene or ethanol.

4.2.4 C₂ Products

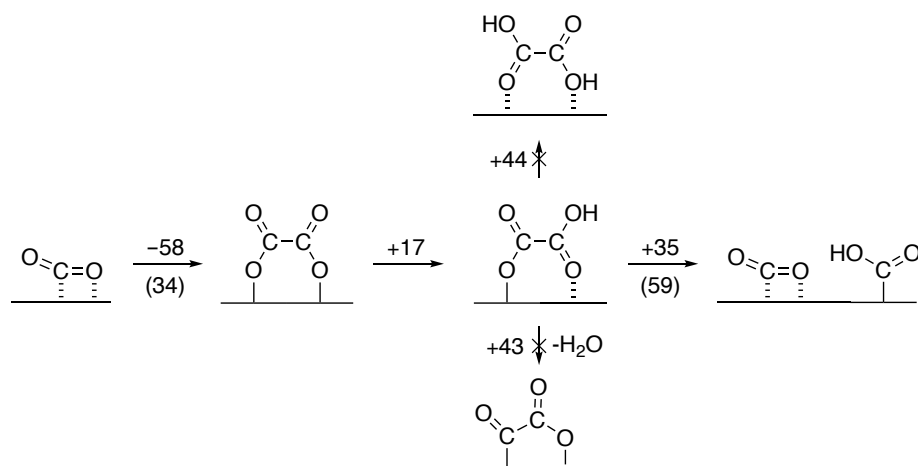
The evaluation of the C₂ formation pathways is far more complex than for C₁ products. Not only are there more observable products (7 vs. 4), which need to be accounted for in the reaction network, but also the C-C bond formation can occur at any point along the C₁ pathway. One indication for a reduction in complexity comes from the experimental observation, that CH₄ and C₂H₄ have different potential limiting steps.^[130,134] This means that the C-C bond formation must occur before *CO hydrogenation to *CHO, since a potential limiting step after that point, which would be even higher in energy, would result in the exclusive formation of CH₄, not C₂ products. In Scheme 3, all possible dimerization processes are displayed with their respective reaction and activation energies (if available).



Scheme 3. Possible C-C formation pathways with their respective reaction energies in kJ/mol. Activation energies are displayed in brackets.

Dimerization at early stages in the mechanism, resulting in oxalic acid type intermediates, show negative or nearly neutral reaction energies. The direct dimerization of two *CO₂ is the most exothermic reaction among them with -58 kJ/mol and a relatively low activation energy of 34 kJ/mol, which seems to be the preferred point of dimerization after a first evaluation. The following hydrogenation to *CO₂COOH is still feasible at a reaction energy of +17 kJ/mol, but at this point a dissociation to *CO₂ and *COOH is energetically less demanding (+35 kJ/mol) than the reaction to oxalic acid or *COCO₂ (Scheme 4).

In addition, oxalic acid has not been observed experimentally, which makes the dimerization at the *CO_2 stage nonrelevant for the formation of C_2 products.



Scheme 4. Early-stage dimerization pathway with corresponding reaction energies in kJ/mol. Activation energies are displayed in brackets (if available).

The next plausible point for dimerization is at the *CO stage. Dimerization can occur either between two *CO or in a concerted manner, coupled with a hydrogenation process, forming *COCHO or *COCOH . The concerted pathways are unlikely, since they are the most energy demanding steps, with over +70 kJ/mol.

The sole dimerization of two *CO requires +64 kJ/mol and an activation energy of 75 kJ/mol. This pathway is also in agreement with experimental observations, which state that CH_4 and C_2 products have different rate determining steps and while the one of CH_4 is pH dependent, the one for C_2 products is not.^[130,134] This coincides with the mechanism described here, since the rate-determining step for CH_4 involves a proton transfer, and the dimerization of *CO does not. This is also the reason why a dimerization of *CHO and *CO is unlikely to be the point of C-C bond formation, despite a reaction energy of only +3.4 kJ/mol. Here, the rate-determining step would be the hydrogenation of *CO for CH_4 and C_2 products, and also the competing hydrogenation of *CHO is energetically much more favored.

An additional important factor for the selective formation of C₂ products is the statistical availability of the C₁ monomers at the dimerization stage. If the energy barrier for dimerization is low, but no second monomer is available, the reaction will follow the C₁ path instead of forming C₂ products.

Studies have shown, that approximately 90% of the catalytically active surface *in operando* is covered with *CO, due to the rate-determining steps being the hydrogenation of *CO in case of CH₄ and its dimerization in case of C₂ products.^[137] Therefore, the high concentration of the monomeric species, necessary for efficient formation of C₂ products, is available and in agreement with the here proposed mechanisms.

Ethylene (Ethylene Glycol, Glycolaldehyde)

After dimerization of two *CO most hydrogenation steps are downhill in energy, making the actual path strongly dependent on the respective activation energies. In a first approximation, the activation energies are expected to follow the *Bell-Evans-Polanyi* principle^[135,136], since those hydrogenation reactions are chemically similar. This means, the activation energies scale in proportion to the reaction energies, resulting in lower activation energies for more exothermic reactions. This behavior was evaluated on the important first hydrogenation step (Figure 20). As expected based on reaction energies, the activation energy of the carbon hydrogenation is proportionally lower than the activation energy for the oxygen hydrogenation.

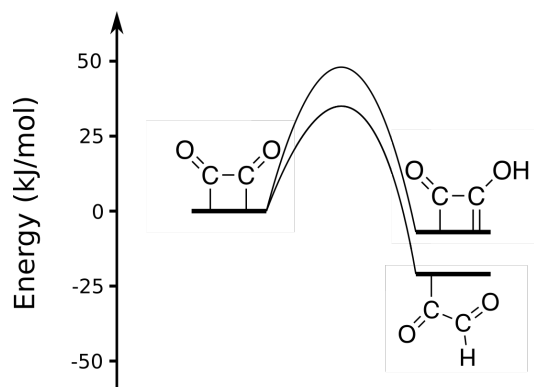


Figure 20. Energy diagram of the hydrogenation of the CO-dimer $*COCO$ at the carbon or oxygen atom.

Therefore, an evaluation based on only reaction energies, following the lowest energy steps, can deliver good estimations, when compared to experimental observations.

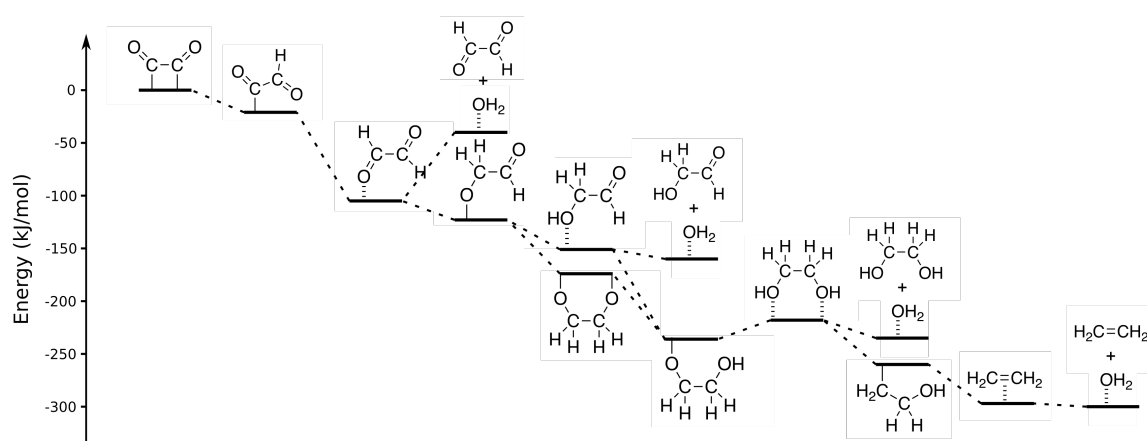


Figure 21. Energy diagram of the proposed mechanism towards ethene, ethylene glycol and glycolaldehyde.

In Figure 21, the minimum energy path for the formation of C_2H_4 and several side products is depicted. The hydrogenation of $*COCO$ to $*COCHO$ is followed by the formation of glyoxal. Glyoxal has not been observed in experimental studies, which is due to a desorption energy of $+56$ kJ/mol and an energetically unhindered further hydrogenation to $*OCH_2CHO$. Whilst the next hydrogenation step can produce glycolaldehyde, which was observed experimentally in small quantities^[51], the formation of $*(OCH_2)_2$ is energetically slightly more favored by -13 kJ/mol. Both intermediates can be reduced further to yield $*OCH_2CH_2OH$.

The next step is the only endothermic hydrogenation along this path. Hydrogenation at the OH-group and subsequent dehydration would require +33 kJ/mol, whereas hydrogenation of the surface-bound oxygen only requires +18 kJ/mol. The so produced and experimentally observed^[51] ethylene glycol can either desorb from the surface (-28 kJ/mol) or form the final C₂H₄ after two hydrogenation/dehydration steps, which is energetically more favored.

Ethanol (Acetic Acid, Acetaldehyde)

The mechanism for ethanol production follows a different pathway than for C₂H₄ production, which includes the formation of the experimentally observed side products acetic acid and acetaldehyde (Figure 22).^[51]

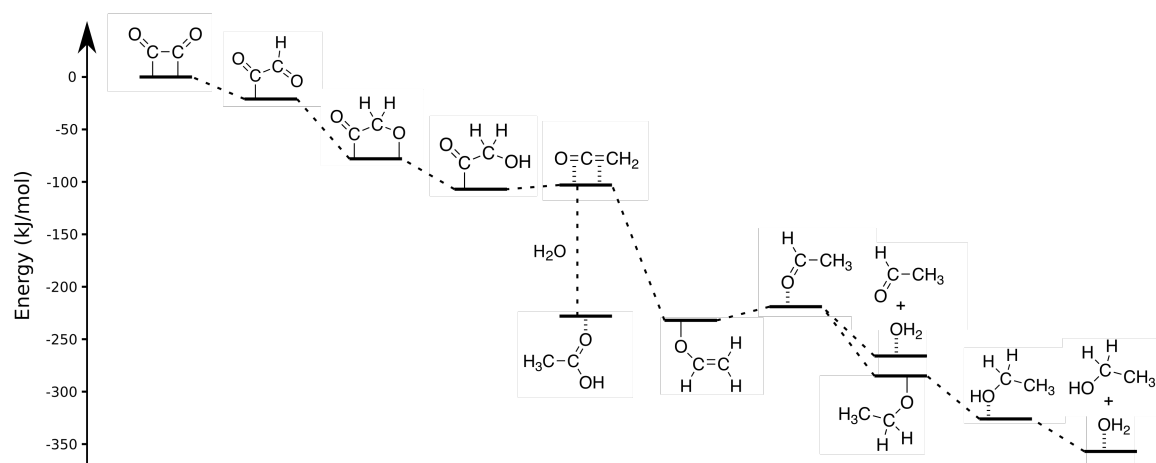


Figure 22. Energy diagram of the proposed mechanism towards ethanol, acetaldehyde and acetic acid.

Like in the C₂H₄-mechanism, the first step involves hydrogenation of the carbon atom on *COCO. In a second step, the same carbon atom is hydrogenated, which is followed by a hydrogenation of the adjacent oxygen atom and subsequent dehydration yielding ethenone. The ethenone can either hydrolyze, yielding acetic acid, an experimentally observed minor product,^[51] or it is further reduced to *OCHCH₂.

At 0 V, both paths are energetically equal, but at applied potentials, the formation of *OCHCH_2 gets more favored, since the hydrolysis is potential independent. The next hydrogenation resulting in acetaldehyde is the only step after C-C bond formation which is slightly endothermic by +13 kJ/mol. But at operating potentials, necessary for C-C bond formation, this step is also exothermic. Acetaldehyde either desorbs (-60 kJ/mol) or gets reduced to *OCH_2CH_3 with a reaction energy of -66 kJ/mol. The last hydrogenation results in adsorbed ethanol, which readily desorbs from the surface (-31 kJ/mol).

This mechanism describes the lowest energy path. However, DFT energies for this application are expected to exhibit errors of approximately 10 kJ/mol, which might alter the described mechanism after C-C bond formation slightly. But more important than the actual mechanism inside the C_2 network, is the finding that there are no significant energetical barriers following dimerization, which leads to the insight that in order to enhance product selectivity towards C_2 products, attention must be given to the early steps and especially to the dimerization process.

4.2.5 Competition between CO_2RR and HER

The competition between CO_2RR and HER is one of the major causes for low FE during formation of the above-mentioned products on any material. On copper, the FE of H_2 ranges from almost 100% at low negative potentials to under 5% under optimized conditions. It has been shown that under usual CO_2 reduction conditions ($pH < 10$), hydrogen evolution is pH dependent and can thereby be expressed in terms of proton reduction.^[138]

In order to exploit the effect of different surfaces on the hydrogen evolution, a model system consisting of two elementary steps was evaluated on Cu(211), Cu(100) and Cu(111) (Figure 23). The first step involves the addition of $H^+ + e^-$ to a surface bearing one water molecule, to mimic a minimal aquatic environment.

A second $\text{H}^+ + \text{e}^-$ pair is added to the adsorbed hydrogen atom to form H_2 in the subsequent step.

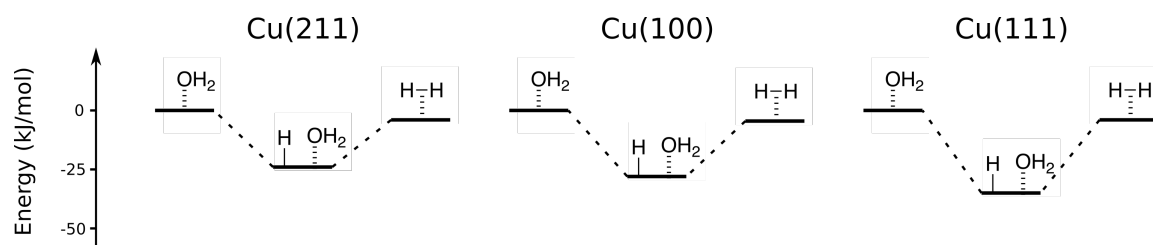


Figure 23. H_2 formation on different copper surfaces.

There are only small differences between the evaluated surfaces. The adsorbed single hydrogen atom is stabilized by -24 kJ/mol (211), -28 kJ/mol (100) and -35 kJ/mol (111) on the respective surfaces. The second, potential limiting step needs an expected overpotential of -0.17 V (211) to -0.26 V (111). This makes HER energetically more favored than CO_2RR on all evaluated surfaces.

The low FE of HER can be explained by means of catalyst poisoning. During CO_2 reduction, the rate limiting step follows the formation of $^*\text{CO}$ along all pathway. This means that if the reaction is not limited by mass transport, the surface is largely covered by $^*\text{CO}$, which inhibits HER and facilitates C_2 product formation through its high concentration on the surface. Steady state experiments in fact have shown $>90\%$ surface coverage of $^*\text{CO}$.^[137] If the applied potential passes -1.4 V, the HER recovers due to a fast depletion of $^*\text{CO}$ and thus available hydrogen reduction sites.^[50,139]

Since hydrogen evolution rates do not depend significantly on the chosen surface, it cannot be suppressed by synthesizing materials with particular surfaces exposed, but by controlling the reaction parameters in a way, that high $^*\text{CO}$ concentrations are achieved.

4.3 Ni/Ga Intermetallics

4.3.1 Introduction to CO₂RR on Ni/Ga Intermetallics

Ni/Ga intermetallics as catalysts for CO₂ reduction were first reported by *Nørskov et al.*^[36] and *Chorkendorff et al.*^[140] in a thermal CO₂ hydrogenation setup in 2014. They found MeOH to be the main product under those conditions. One electrochemical study on the CO₂RR with Ni/Ga intermetallics has been conducted by *Lewis et al.*^[141] in 2016. They observed an almost exclusive selectivity towards hydrocarbons with only trace amounts of CO. Main product was CH₄, followed by C₂H₆ and small amounts of C₂H₄ for all compositions. Ni₃Ga was found to have the highest selectivity towards CH₄, while NiGa showed the highest rate for C₂H₆ at low overpotentials. Despite their high observed selectivities, the amounts of hydrocarbons account for up to 4% FE only, compared to 96% FE for hydrogen, which leaves room for improvements. In order to understand the effects of composition on the activity and selectivity of Ni/Ga catalysts in the CO₂RR, two different models were chosen in this study. One represents the (210) surface of β -NiGa with a Ni-rich exposed step, and the other represents α -Ni₃Ga with a mixed (211) surface step (Figure 24).

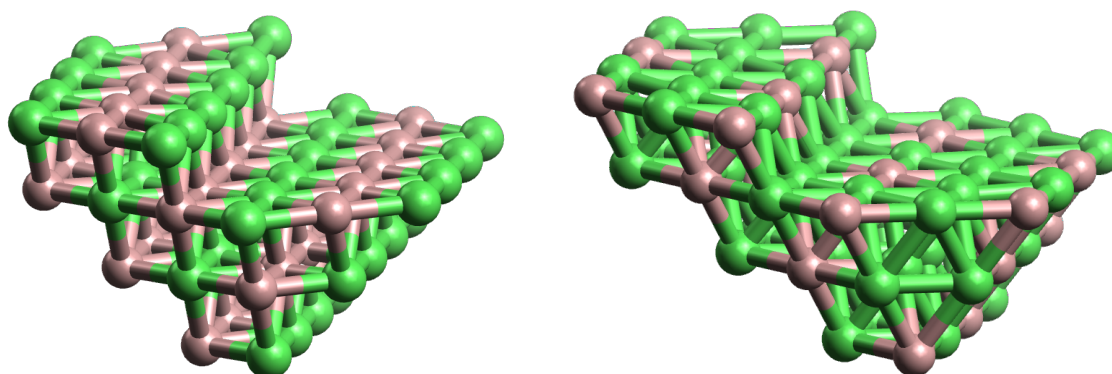
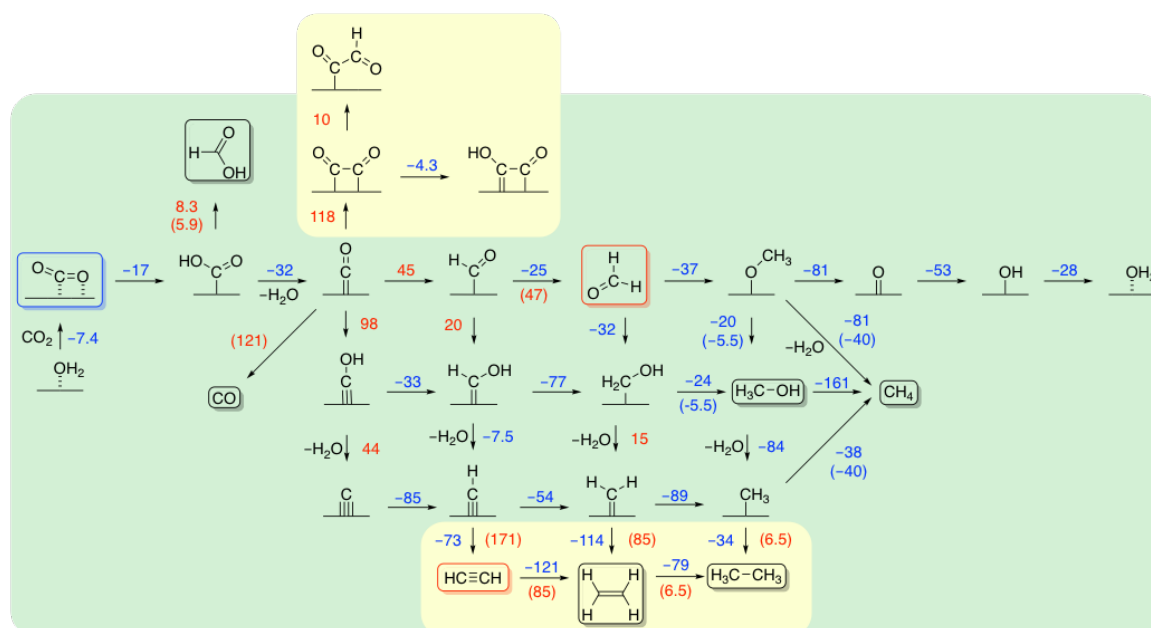


Figure 24. Model clusters of NiGa(210) (left) and Ni₃Ga(211) (right). Ni is depicted in green, Ga in red.

4.3.2 NiGa



Scheme 5. Reaction network on NiGa(210) with all reaction energies in kJ/mol. Desorption energies are denoted in brackets. C₁ and C₂ pathways are highlighted in green and yellow, respectively. Stable products are framed. The products in red frames have not been observed experimentally.

The relevant reaction steps and their corresponding energies on the stepped NiGa(210) surface are depicted in Scheme 5. Here, the CO₂RR towards CH₄ is likely to follow the same path as on the Cu(211) surface (Figure 25, top). After formation of *COOH and subsequent hydrogenation and dehydration resulting in *CO, the lowest energy path contains the *CHO, *OCH₂ and *OCH₃ intermediates, finally producing CH₄. Although, an alternative pathway with hydrogenation of *OCH₂ at the oxygen center is very similar in energy and cannot be distinguished clearly from the former mechanism due to limited accuracy of the DFT method (Figure 25, bottom). Here, the produced *CH₂OH intermediate is dehydrated in the next step, leading to *CH₂, which is hydrogenated successively to finally yield CH₄. Despite the dehydration of *CH₂OH being endothermic by +15 kJ/mol at 0 V, at the potentials necessary for *CO hydrogenation, this step is also significantly exothermic.

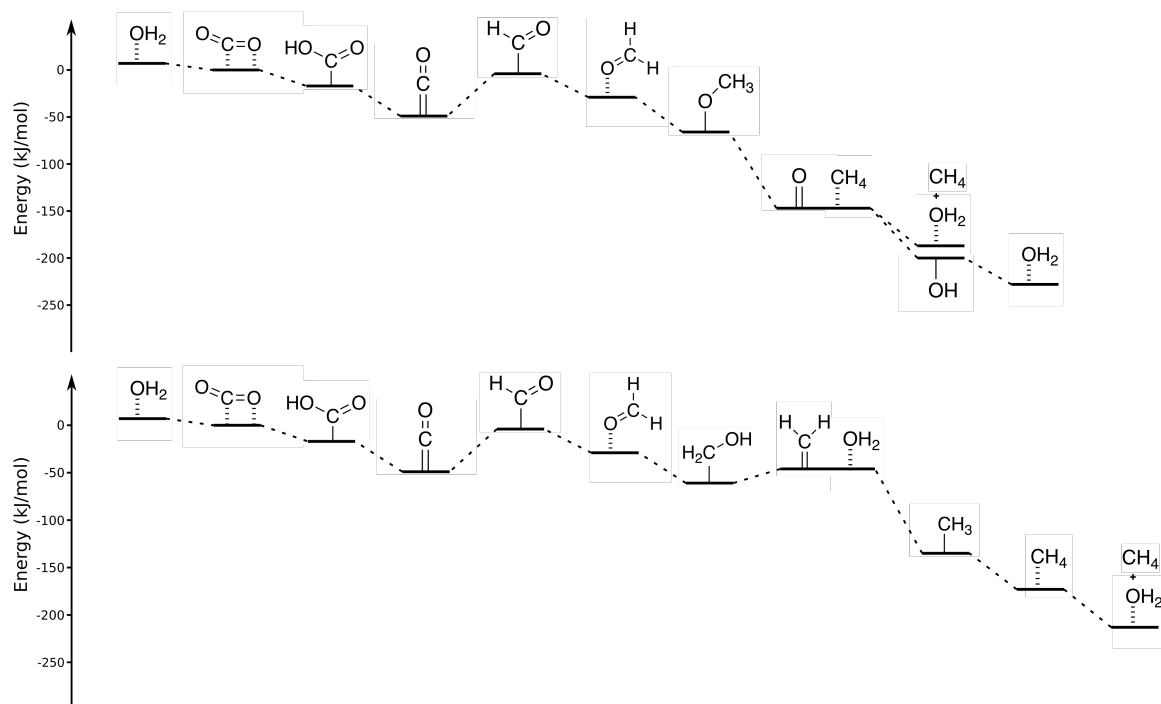


Figure 25. Energy diagrams of the two possible pathways from CO₂ to CH₄ on NiGa(210).

The different product selectivity between copper and NiGa lays in energetic differences of the relevant steps. Formic acid was observed as one of the main products on copper in several studies, while it was not observed at all on NiGa. This finding most likely results from the higher hydrogenation energy of *COOH towards *HCOOH of +8 kJ/mol (NiGa) compared to +2 kJ/mol (Cu) and the lower hydrogenation energy of *COOH towards *CO of -32 kJ/mol (NiGa) compared to +6 kJ/mol (Cu). This results in a preference of *CO over formic acid on NiGa by about -40 kJ/mol compared to +4 kJ/mol on Cu. In addition, CO is one of the main products on Cu, whereas it was only observed in trace amounts on NiGa, because of the difference in desorption energy. On Cu, +69 kJ/mol are needed to release CO from the surface, compared to +121 kJ/mol on NiGa.

The reaction energies from *CO to *CHO are comparable with their +45 kJ/mol and +40 kJ/mol on NiGa and Cu, respectively, which results in similar onset potentials.

The only C₂ products that are observed experimentally on NiGa are C₂H₆ and trace amounts of C₂H₄, which could indicate a different mechanism than on Cu with up to seven C₂ products. The rate-limiting step of the preferred pathway towards C₂ products on Cu is the dimerization of two *CO. On NiGa, this step needs +118 kJ/mol, which is hardly feasible at ambient temperature and much more than necessary for the competing *CHO formation. A more plausible dimerization takes place at a late stage in the CH₄ mechanism (Figure 26). The *CH₂ intermediate can dimerize to *C₂H₄ or react to *CH₃. The hydrogenation to *CH₃ is significantly more exothermic and therefore the preferred pathway, which agrees with the observed low selectivity towards C₂H₄. At this point, the dimerization and hydrogenation are at similar energetic levels, which explains the observed comparable selectivity towards CH₄ and C₂H₆.

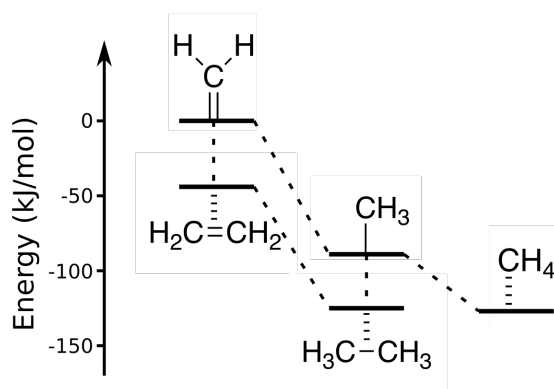
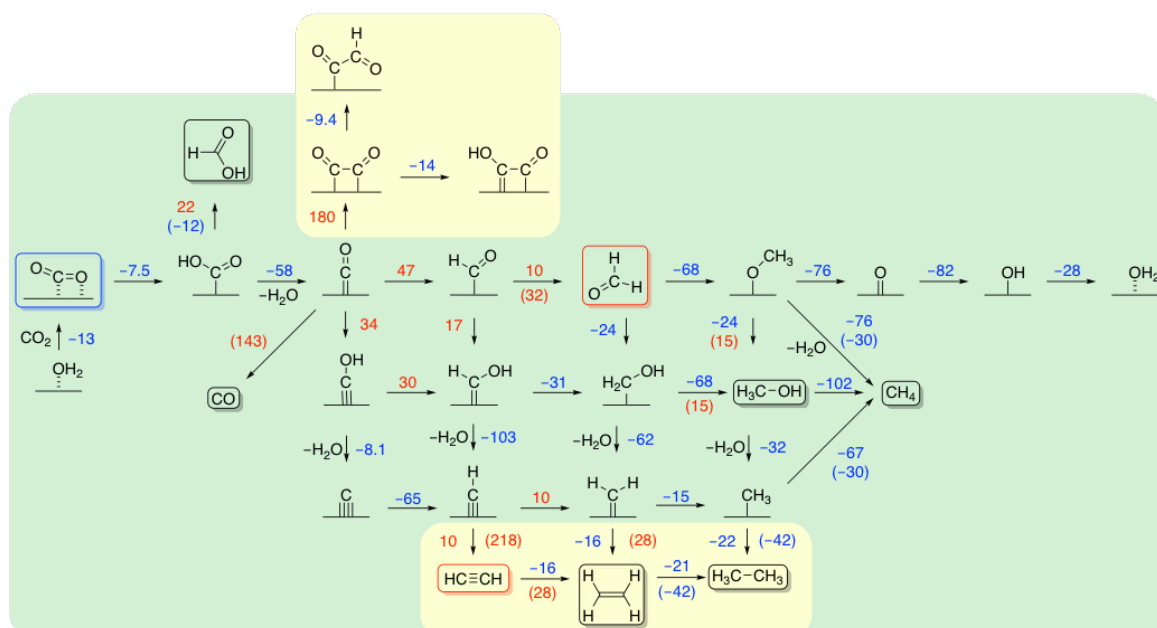


Figure 26. Energy diagram of possible dimerization reactions on NiGa(210).

4.3.3 Ni₃Ga



Scheme 6. Reaction network on Ni₃Ga(211) with all reaction energies in kJ/mol. Desorption energies are denoted in brackets. C₁ and C₂ pathways are highlighted in green and yellow, respectively. Stable products are framed. The products in red frames have not been observed experimentally.

The relevant reaction steps and their corresponding energies on the stepped Ni₃Ga(211) surface with a mixed step of alternating Ni and Ga atoms are depicted in Scheme 6. Here, the energetics on the path towards CH₄ differ significantly from those on NiGa and Cu, resulting in an altered mechanism (Figure 27).

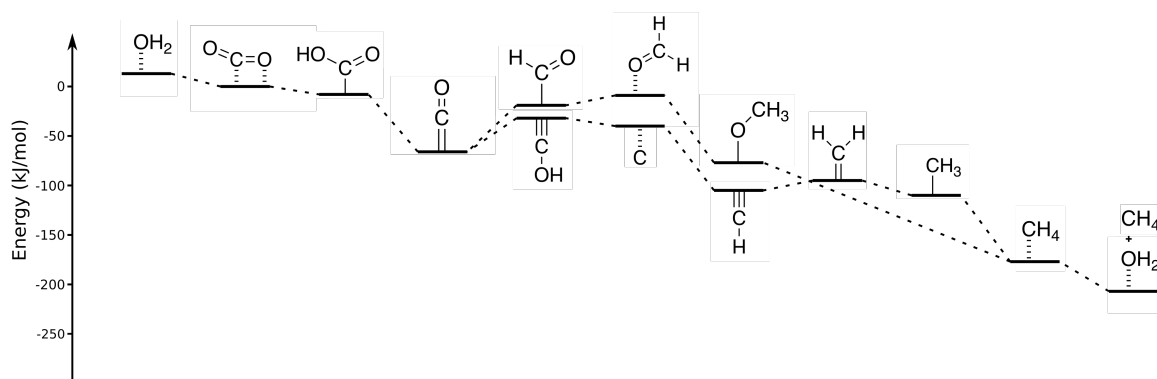


Figure 27. Energy diagram of the two possible pathways from CO₂ to CH₄ on Ni₃Ga(211).

The first steps are similar to NiGa, where each hydrogenation is downhill in energy until a basin is reached at the $^*\text{CO}$ intermediate. The subsequent hydrogenation is favored at the oxygen atom, instead of the carbon atom as on NiGa and Cu, by -13 kJ/mol. This opens an alternative pathway, where also the second oxygen is abstracted, forming a carbide $^*\text{C}$ intermediate, which is then hydrogenated successively to finally yield CH_4 .

Reason for the relative low energy of $^*\text{COH}$ compared to $^*\text{CHO}$ is the confining structure of the $\text{Ni}_3\text{Ga}(211)$ surface. The surrounding Ga atoms force the adsorbates to coordinate to a set of two Ni atoms in a way that differs from pure Ni steps of the same Ni_3Ga phase (Figure 28).

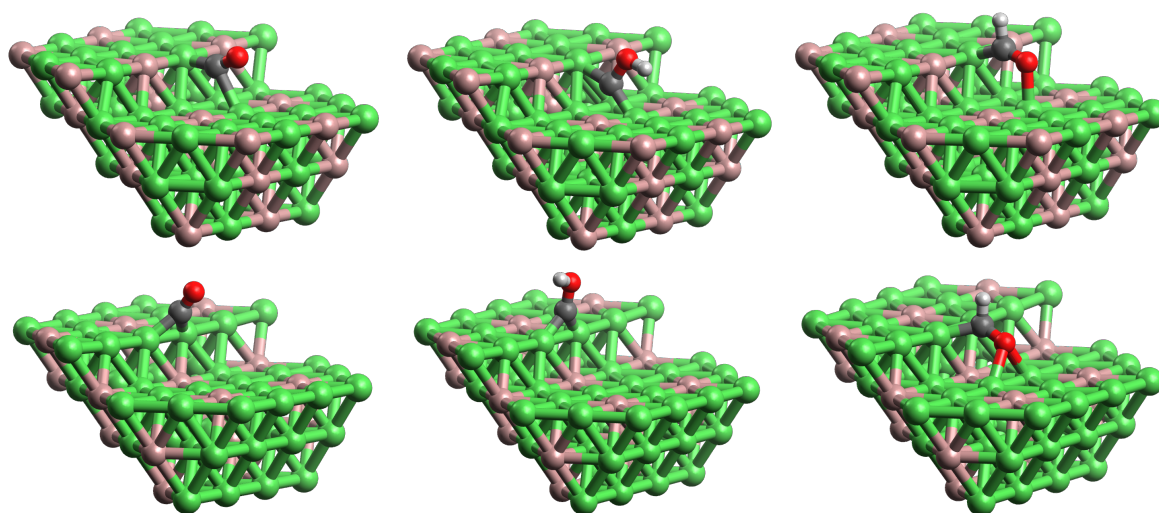


Figure 28. Structures of $^*\text{CO}$, $^*\text{COH}$ and $^*\text{CHO}$ (left to right) on a mixed (top) and a pure Ni (bottom) stepped surface.

On mixed steps, $^*\text{CO}$ is allowed to coordinate to the surface in a step-bridging fashion, in contrast to on-step on pure Ni steps. Although the coordination mode is different, desorption energies are very similar with $+143$ kJ/mol and $+145$ kJ/mol, respectively. $^*\text{CHO}$ is oriented in the same direction on both surfaces, which leads to similar hydrogenation energies yielding $^*\text{CHO}$ of $+47$ kJ/mol and $+64$ kJ/mol. On the pure Ni step, as on NiGa, the most stable conformation of $^*\text{COH}$ is on the stepped site, while on the mixed step the most stable conformation is step-bridging.

This configuration is, directed through the neighboring Ga centers, about -100 kJ/mol more stable than the one on the pure Ni step without directing Ga centers. On the pure Ni step a larger electron density resides on the carbon center, which leads to a charge of $-0.39 e$ vs. $-0.09 e$. This electron density can be distributed better on the mixed step, which leads to a more stabilized adsorbate (Figure 29).

A local energetic minimum which is similar to the one on the mixed step, was not found on the pure Ni step, which makes both depicted conformations the equivalent minimum energy structures.

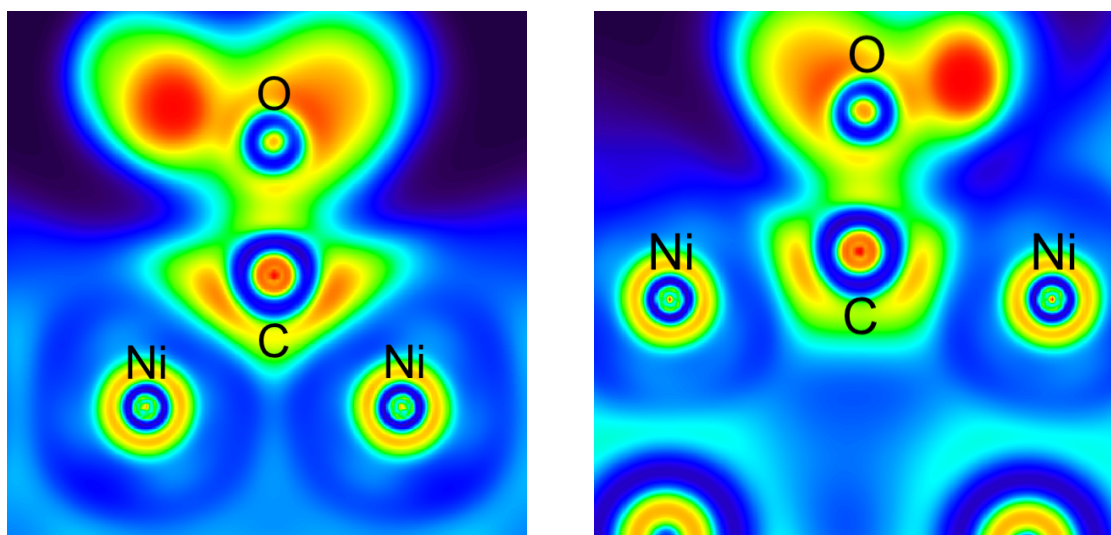


Figure 29. ELF plot of the adsorbed *COH on a pure Ni (left) and mixed (right) Ni₃Ga stepped surface in the Ni-C-Ni plane.

Although it is reasonable to assume that neither perfect mixed nor pure Ni steps are present in real samples, this comparison illustrates the structure-directing properties of Ga in Ni/Ga intermetallics, which lead to significant changes in reaction energies.

Evidence for the *COH pathway might be found experimentally through the identification of carbides or *carbon black* after electrolysis, introduced by the *C intermediate.

The carbide pathway also allows for the formation of C_2H_4 and C_2H_6 along the way through dimerization of $*CH_2$ and $*CH_3$, with dimerization energies of -16 kJ/mol and -22 kJ/mol, respectively (Figure 30). Experiments have shown that on Ni_3Ga , CH_4 is the main CO_2RR product, followed by C_2H_6 and small amounts of C_2H_4 .

These observations can be explained with the relative energies of the participating intermediates. The $*CH_2$ can dimerize to $*C_2H_4$ or is hydrogenated to $*CH_3$, at very similar energies. For the dimerization reaction, however, two $*CH_2$ intermediates must be in close proximity to each other and since the surface concentration of $*CH_2$ is expected to be low, the hydrogenation should be the most occurring reaction. Even if $*C_2H_4$ is formed, it can be readily reduced to $*C_2H_6$, since a desorption of C_2H_4 would require $+28$ kJ/mol and the hydrogenation is -21 kJ/mol downhill in energy. The stronger selectivity towards CH_4 is caused by the more exothermic hydrogenation of $*CH_3$ (-67 kJ/mol), compared to the dimerization energy of -22 kJ/mol.

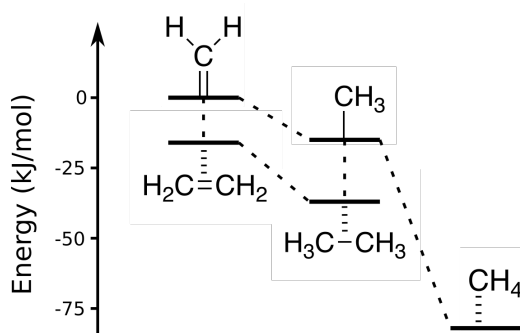


Figure 30. Energy diagram of possible dimerization reactions on $Ni_3Ga(211)$.

4.4 Other Materials

The in-depth comparisons of Cu, NiGa and Ni₃Ga revealed the hydrogenation of *CO to be the potential limiting step in all cases. Plotting the binding energies of *CHO against the binding energies of *CO on several materials reveals a linear scaling relationship (Figure 31).

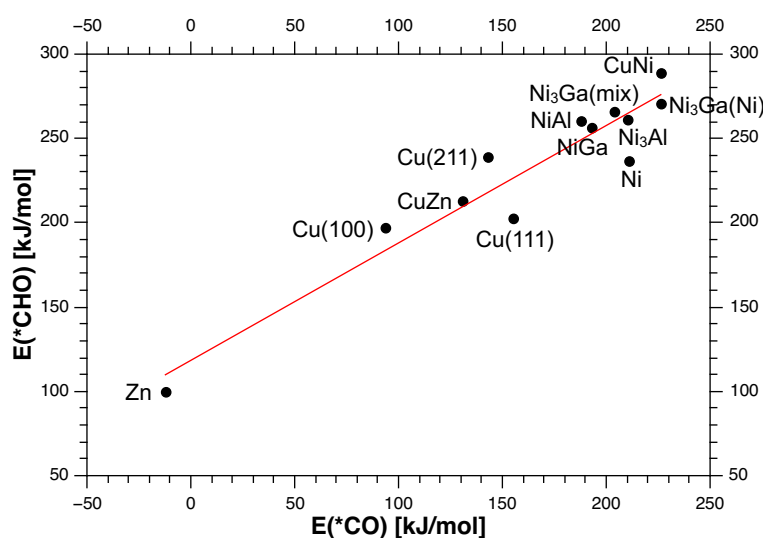


Figure 31. Binding energies of *CHO plotted against the binding energies of *CO.

Linear scaling relations are often used to rapidly screen materials for their catalytic activity. If linear scaling relations exist, the catalytic activity can be mapped as a function of one or two variables, thus reducing the complexity and estimating the catalytic activity of new materials, based on those variables. This approach has been used successfully to discover new catalytic materials.^[35,142–144]

The observed scaling relation implies a linear dependency between the binding strength of *CO and *CHO across all materials, which in turn means that the hydrogenation energy cannot be altered by designing a material that stabilizes one intermediate over the other. This would always affect the binding energies of both intermediates.

However, since the slope of the best-fit line is 0.7, not one, the reaction energy can be varied by a modification of the CO binding energy. Stabilizing *CO leads to a proportionally less stabilized *CHO and thus a larger energy gap between them. A lesser activation energy is therefore achieved with less stabilized *CO . Using the example of Cu(211) and NiGa, the desorption energy of CO is lower on Cu(211) (+143 kJ/mol vs. +193 kJ/mol), which results in a lower hydrogenation energy on Cu(211) of +13 kJ/mol compared to +45 kJ/mol on NiGa. On the other hand, a less stabilized *CO also leads to an easier desorption of CO, lowering the selectivity for CH_4 and C_2 products. This can be illustrated with the example of Zn. Here, the hydrogenation energy of *CO to *CHO (−4 kJ/mol) is very low, but this also favors the desorption of CO at −12 kJ/mol, which is the most reduced product observed on Zn. When focused on the lowest overpotentials, an optimum between reaction energy and CO desorption can be found by evaluating all activation energies (reaction rates) as a function of CO binding strength, but this would always result in a mixture of products. Since a subsequent separation of those products would be much more expensive, a higher selectivity is more energy- and cost-efficient, even if larger potentials are required.

It needs to be noted, however, that the energetics on different materials, plotted in Figure 31, do not follow the linear trend perfectly. The R^2 value of the linear regression line is 0.92, which can be a result of method inaccuracy or more likely an indication for some amount of variance in the dependency, that can be utilized.

As a result, the linear scaling relationship limits the possibilities for catalyst design. In order to enhance product selectivity and thereby cost efficiency of the process, research activities should be focusing on moderately strong CO binding sites in the range of CO desorption energies from +50 kJ/mol to +180 kJ/mol. Below this range, CO production is favored, while a larger desorption energy leads to the domination of HER. The focus on stronger CO binding sites in this energy window enhances the selectivity for CH_4 over CO release, while at the same time raising its onset potential. This increase in onset potential, however, is proportionally lower than the gain in selectivity and can be accepted as minor drawback.



5 Evaluation Part II: Material Synthesis

5.1 MOCVD

The chemical vapor deposition of metallic films is of technological interest for their applications in microelectronic devices, protective coatings or catalyst industries. Their high potential applications are based on their intrinsic properties including, electrical conductivity, chemical and thermal stability as well as catalytic activity.^[145]

Thin films of Cu and Ni/Ga intermetallics produced via CVD can serve as inexpensive (low amount of material) and potentially highly active (structured surface) electrocatalysts for CO₂RR.

5.1.1 Copper

Several different Cu precursors were applied in the CVD of Cu, Cu₂O and CuO thin films. Many ligands, and by far the most often used type, are variations of the acetylacetonate (pentane-2,4-dionate, acac) ligand. By the early 1960s, the number of Cu(II) β -diketonates exceeded sixty.^[146] Variations include the substitution of one oxygen against an N-R group^[147], the extension of the carbon chain^[148], the substitution of the γ -H^[149], the introduction of fluorinated groups at the ligands backbone^[150,151].

Acetylacetonates are a convenient group of precursors due to their stability against oxygen and moisture, their volatility and their simple synthetic accessibility.

Deposition experiments with the $\text{Cu}(\text{acac})_2$ precursor were conducted in a hot-wall reactor, equipped with a quartz tube, on Si(100) substrates.

In a first setup, argon (40 sccm) was used as a carrier gas at a pressure of 20 mbar and temperatures of 350 °C. The substrate was placed in the center of the quartz tube and was heated to the intended temperature. When a steady temperature was reached, the tube was shifted so that the precursor container moved from the cold zone inside the temperature gradient of the oven in order to facilitate sublimation without decomposition. After a deposition time of 30 min, a copper colored film was obtained on the substrate. Morphology and composition of the film were analyzed via *scanning electron microscopy* (SEM) and *energy-dispersive X-ray spectroscopy* (EDX) (Figure 32).

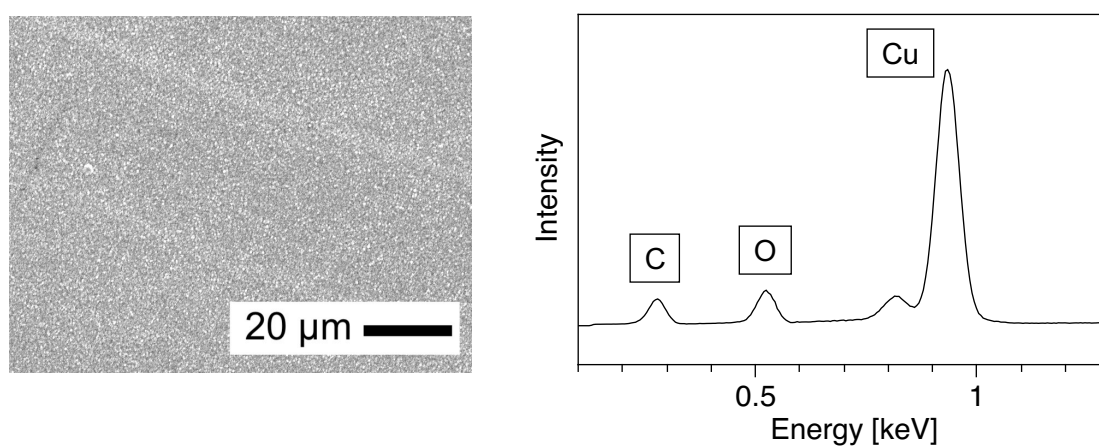


Figure 32. SEM image (left) and EDX spectrum (right) of a Cu film, produced at 20 mbar and 350 °C.

The obtained film exhibited a rough but homogeneous structure and contained moderate amounts of residual carbon and oxygen.

A quantification of those light elements via this standardless EDX method is not reliable, especially in comparison to the heavy elements used, like Cu, Ni and Ga. Therefore, denoted quantities of carbon and oxygen can be assumed to be rough estimations and are used for qualitative statements.

The addition of 5 sccm H_2 to the gas stream resulted in a reduction of the carbon and especially the oxygen contents of the film, but still carbon contents of approx. 10% remained. Also, the morphology changed from a closed grainy film

to individual nanoparticles, indicating a gas-phase reaction of $\text{Cu}(\text{acac})_2$ with H_2 (Figure 33). A reduction in temperature resulted in a reduced number of nanoparticles, but no change in morphology was achieved.

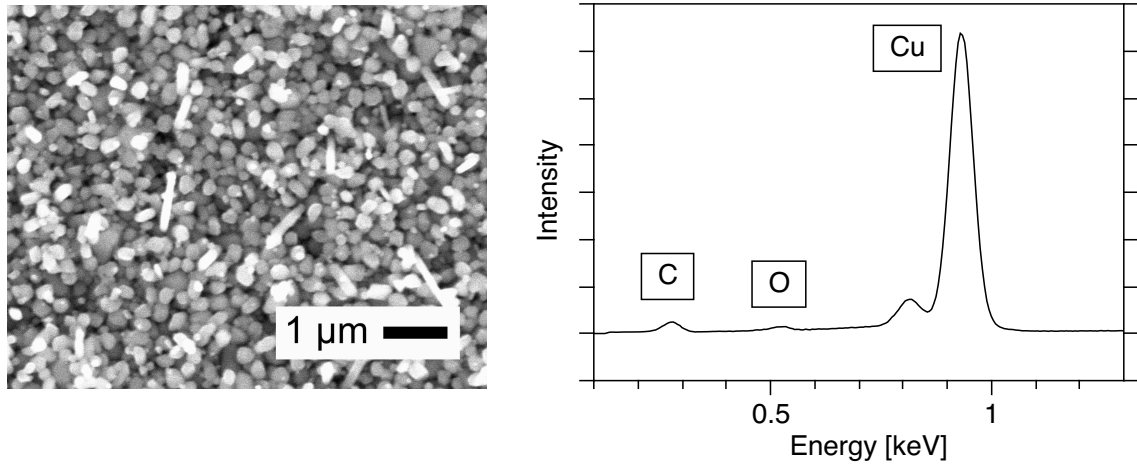


Figure 33. SEM image (left) and EDX spectrum (right) of the nanoparticles produced with $\text{Cu}(\text{acac})_2$ and addition of H_2 .

In order to avoid gas-phase reactions but still reduce the amount of residual carbon and oxygen in the deposited films, in a second setup, the preparation process was separated in two parts. A CuO film was deposited using an Ar/O_2 gas stream and reduced to Cu in a H_2 stream subsequently. Best results were achieved with $320\text{ }^\circ\text{C}$, 40 sccm Ar and 5 sccm O_2 at 20 mbar. A closed film of phase pure CuO with minimal amounts of residual carbon was obtained (Figure 34).

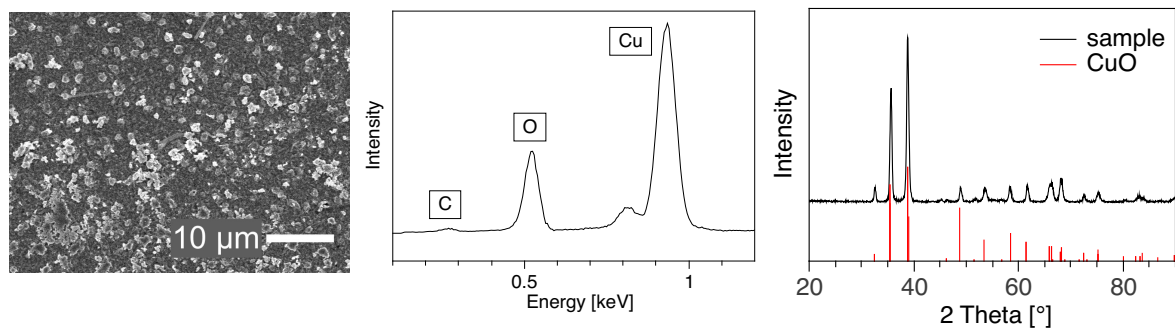


Figure 34. SEM image (left), EDX spectrum (center) and XRD diffractogram (right) of a prepared CuO film.

The CuO film was then reduced in a stream of 30 sccm H₂ at atmospheric pressure and 500 °C over the course of 3 h. EDX and *X-ray diffraction* (XRD) of the resulting porous film showed no residual oxide and carbon content (Figure 35).

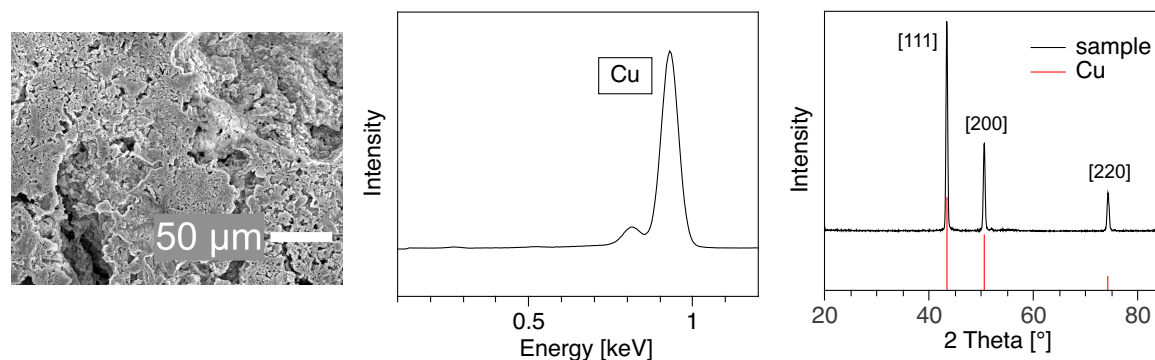


Figure 35. SEM image (left), EDX spectrum (center) and XRD diffractogram (right) of an oxide-derived Cu film.

The porosity of the prepared films makes them promising electrode materials in the electrochemical CO₂ reduction. On the one hand, the high surface area created by the porosity enhances the contact between the electrode and the CO₂ saturated solution, and on the other hand oxide derived copper has been shown to possess a higher selectivity towards highly reduced C₂ products such as ethylene and ethanol.^[106,152]

5.1.2 Solid Precursors: Ni(acac)₂ and Ga(acac)₃

A number of Ni and Ga precursors have been synthesized and evaluated for their application in MOCVD. Ligands that have been used for Ni precursors include carbonyl^[153], β-diketonates^[154], cyclopentadienyl^[155], aminoalkoxides^[156,157] and phosphites^[158]. For Ga precursors, especially alkyls^[159,160], alkoxides^[161] and β-diketonates^[162–164] are commonly used ligands.

Acetylacetonates are a convenient group of precursors due to their stability against oxygen and moisture, their volatility and their simple synthetic accessibility.

The synthetic efforts for the production of Ni/Ga intermetallic films were focused on Ni-rich compositions, since those phases have been shown to be more active in CO₂ reduction and are expected to be more stable against oxidation.^[36]

Deposition experiments were conducted in a hot-wall reactor setup (see chapter 7.4) on Si(100) substrates with native oxide layer and Ar as carrier gas. The reactor pressure was set to 1 mbar, ensuring sufficient sublimation at the chosen temperatures. The temperature was varied between 300 °C and 500 °C. Above 350 °C, the morphology of the produced films did not change but their carbon and oxygen content increased.

The resulting films possessed a grainy surface, good coverage and adherence on the substrate. They showed the intended composition of Ni/Ga = 1/1 with deviations of $\pm 5\%$, but with large amounts of residual carbon and oxygen (20-50%).

The addition of 5% H₂ to the carrier gas stream resulted in the reduction of contaminations, although still substantial amounts of oxygen and especially carbon remained in the film. Even post-deposition treatment with H₂ under higher temperatures could not reduce the carbon content in the films. EDX analysis showed a Ni/Ga ratio of 45/55 and XRD confirmed the β -NiGa phase without additional crystalline phases (Figure 36).

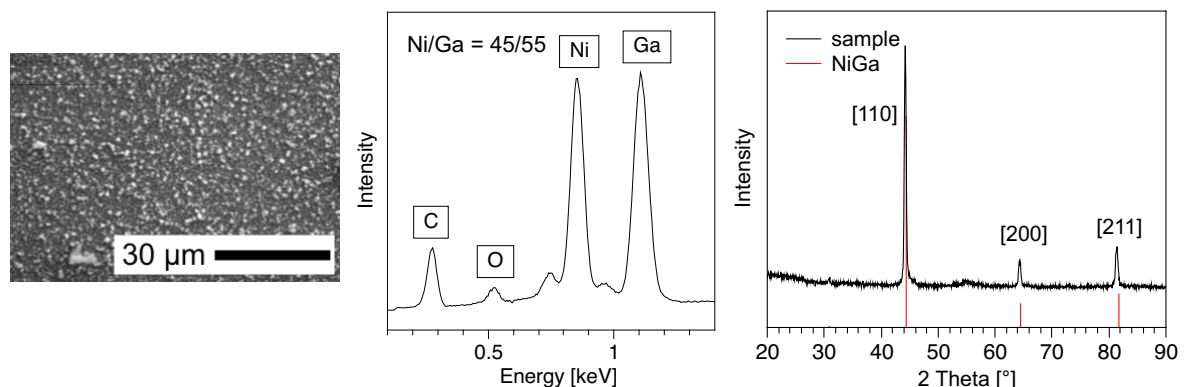


Figure 36. SEM image (left), EDX spectrum (center) and XRD diffractogram (right) of a prepared NiGa film at 330 °C.

A substantially different Ni/Ga ratio than 1/1 could not be achieved, since the composition of the film with this solid precursor setup is dictated by the Ni/Ga ratio in the gas phase. This, in turn, is mainly determined by the vapor pressure of the precursors. In order to tune the composition of the resulting film, several different precursor combinations would have to be evaluated in addition to the other deposition parameters. This inconvenience was circumvented through a different setup, where the feed rates of liquid Ni and Ga precursors can be adjusted individually.

5.1.3 Liquid Precursors: Ga^tBu₃ and Ni(allyl)Cp

The complex nature of the Ni/Ga phase diagram generates the need for highly volatile Ni and Ga precursors in order to control their stoichiometry in the gas phase individually. This is best achieved with bubbler systems, which require liquid precursors. This, however, eliminates most of the established nickel precursors, since most of them are solid under operation conditions. The liquid Ni(CO)₄ and Ni(PH₃)₄ were ruled out, due to their high toxicity, and some also liquid nickel aminoalkoxides were known to result in films with high amounts of residual impurities.^[156,157] Allylcyclopentadienylnickel remained, since it met all criteria. It melts at 9 °C, has one of the highest vapor pressures (10 Torr at 73 °C) after Ni(CO)₄ and gives Ni films with <5% residual carbon and no oxygen.^[165]

Differential scanning calorimetry (DSC) analysis of Ni(allyl)Cp (Figure 37, left) shows clean thermal decomposition at 215 °C and an onset temperature of 185 °C.

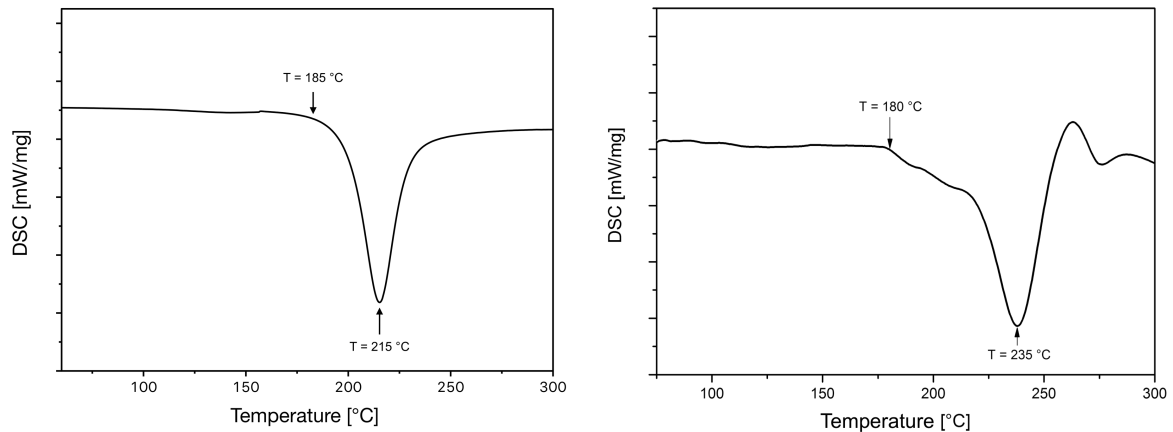


Figure 37. DSC curves of Ni(allyl)Cp (left) and GaᶠBu₃^[166] (right).

Corresponding to this decomposition temperature, GaᶠBu₃ was chosen as gallium precursor due to its similar decomposition and onset temperatures of 235 °C and 180 °C, respectively.

Trialkylgallium (R₃Ga) compounds, among others, have been used as precursors in the MOCVD of GaN and gallium chalcogenides for an application in electronics.^[167–170] They are known for their high volatility and clean decomposition.

For this application a cold-wall MOCVD reactor (see chapter 7.4) was chosen, because it allows for an optimal temperature control and most efficient utilization of the precursor material. The two precursors were delivered to the reaction chamber through two individual bubbler systems via an Ar stream and were decomposed on Si(100) substrates with native oxide layer. An additional H₂ stream was introduced at the inlet of the reaction chamber, in order to facilitate clean decomposition and reduce the amount of residual carbon in the film.

Deposition experiments were carried out at a reactor pressure of 50 mbar, ensuring a sufficient saturation of precursor molecules in the gas phase. The ideal deposition temperature was found to be 330 °C. At lower temperatures, no sufficient growing rates could be achieved, while higher temperatures led to higher amounts of residual carbon content in the film.

Flow rates of the carrier gas were altered in order to gain access to different compositions of the resulting material films. Flow rates of 10 sccm (Ni), 10 sccm (Ga) and 2 sccm H₂ led to the formation of phase-pure NiGa films with a composition of 45% Ni and 55% Ga (Figure 38). Only trace amounts of residual carbon were observed in the EDX spectrum, while the observed oxygen peak resulted from surface oxidation during the transport from the reactor to the SEM/EDX device.

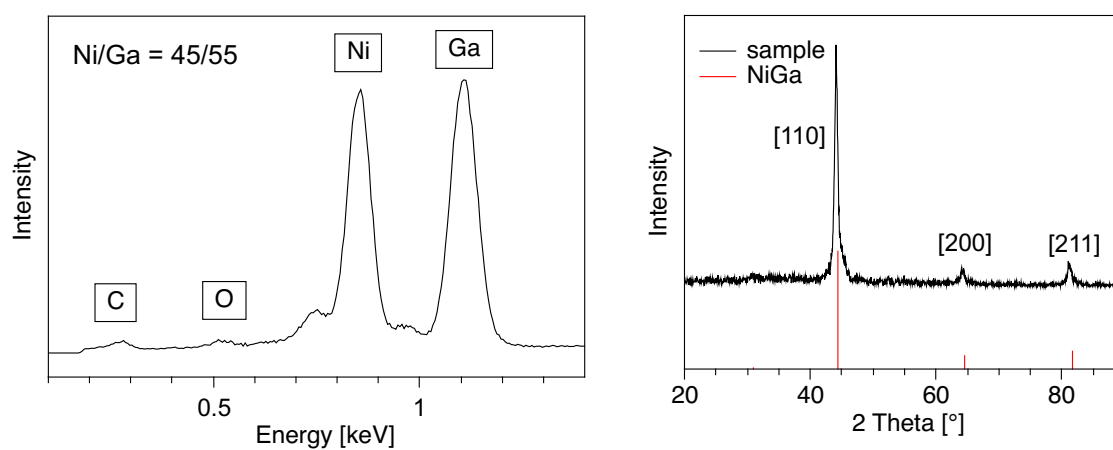


Figure 38. EDX spectrum (left) and XRD diffractogram (right) of a NiGa film, produced in the cold-wall MOCVD setup.

Based on the SEM images in Figure 39, the film covers the whole substrate and possesses a rough, grainy texture. A deposition time of 30 min lead to a film thickness of 0.80 μm .

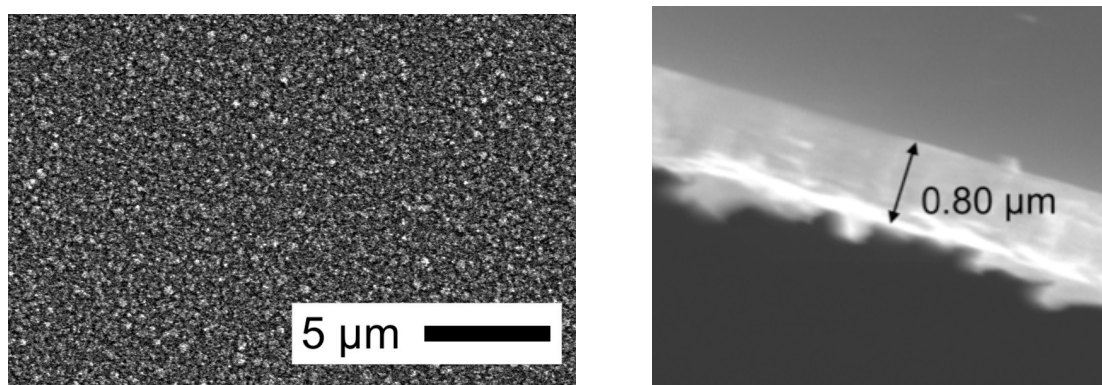


Figure 39. SEM images of the sample's surface (left) and cross-section (right).

An increase in flow rates of the Ni feed, led to the formation of textural similar films with also only minimal amounts of residual carbon (Figure 40). Compositions in the range from a Ni_1Ga_1 to a Ni_7Ga_3 , based on EDX, could be achieved.

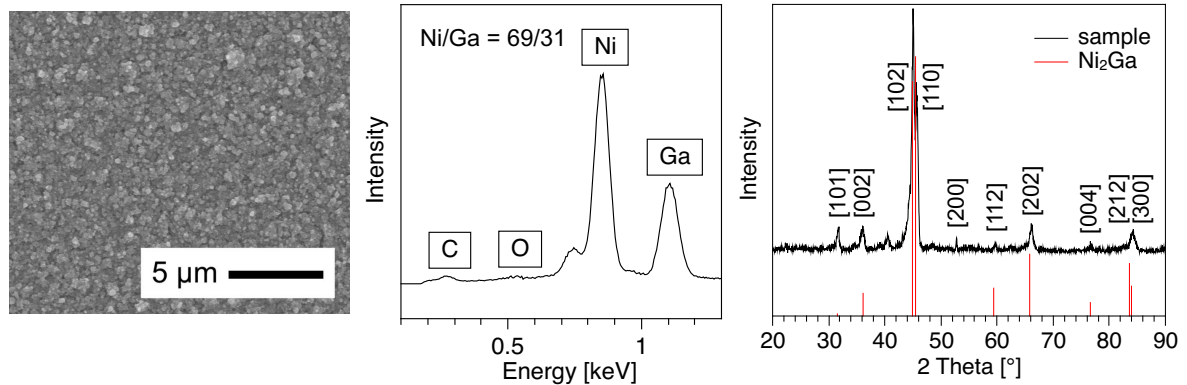


Figure 40. SEM image (left), EDX spectrum (center) and XRD diffractogram (right) of a Ni/Ga film produced in the cold-wall MOCVD setup with elevated flow rates of the Ni feed.

XRD analysis of the films produced with flow rates of 20 sccm (Ni) and 10 sccm (Ga), showed the presence of a pure Ni_2Ga phase (Figure 40, left). A further increase of the Ni flow rate, however, shifted the crystalline phases to a mixture of Ni_3Ga and Ni_2Ga (Figure 41). At relative flow rates beyond 3/1 (Ni/Ga) no formation of Ni/Ga phases was observed, while the film consisted of Ni only.

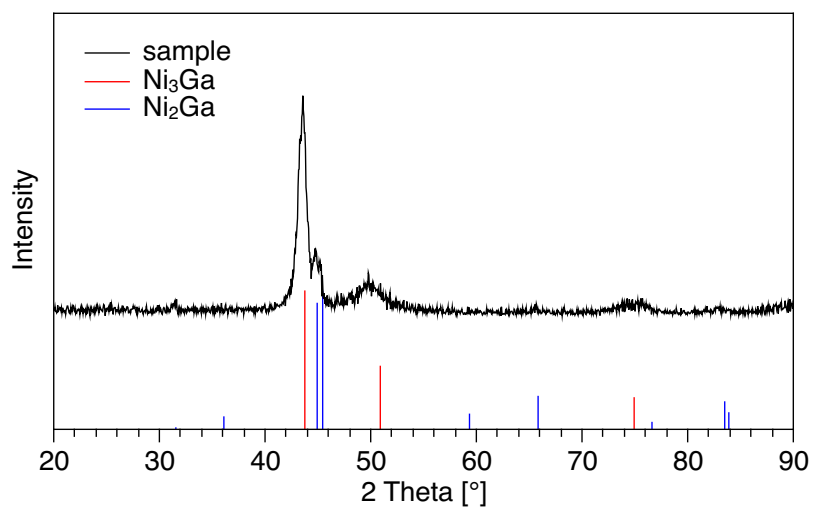


Figure 41. XRD diffractogram of a Ni/Ga film, produced in the cold-wall MOCVD setup with elevated flow rates of the Ni feed.

Due to the broad variety of different Ni/Ga phases, the narrow composition window and the flat energy profile between the individual phases, most compositions are not accessible via this method. Phase pure samples could, however, be obtained of the NiGa and Ni₂Ga phase with only minimal amounts of residual carbon.

5.2 Induction Melting

For the comparison between quantum mechanical calculations and electrochemical experiments, material samples of high purity are needed. Since even small impurities can affect the energetics of the observed reactions, this would alter the results, thus rendering the comparison invalid.

In contrast to the thin films produced via MOCVD, with a rough surface and limitation to the β -NiGa and Ni₂Ga phases, induction melting provides access to clean samples and variable compositions. Metallurgic samples of Ni/Ga intermetallics have been produced via induction melting^[66,67] and arc melting^[68,171] under inert atmosphere before.

First orienting experiments were carried out in an open crucible under air. This led to the formation of a thick gray oxide layer, which can be attributed to the oxidation of mainly Ga (Figure 42, left). Since partial oxidation of the gallium under these conditions altered the Ni/Ga ratio in an unpredictable manner, the setup was modified in order to exclude oxygen (Figure 43).

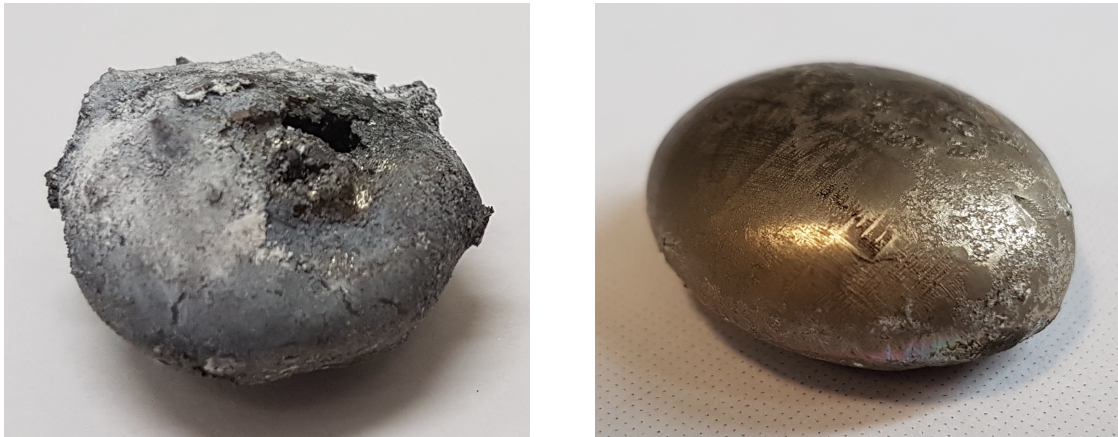


Figure 42. Sample of Ni/Ga after induction melting under air (left) and argon (right) atmosphere.

The crucible was equipped with an argon hose and a glass cap in order to prevent oxidation, while retaining the ability to observe the molten sample. An argon flow of approx. 200 sccm was sufficient to exclude most oxygen content from the atmosphere after initial 10 min purging. The resulting samples exhibited only minimal amounts of surface oxidation (Figure 42, right).

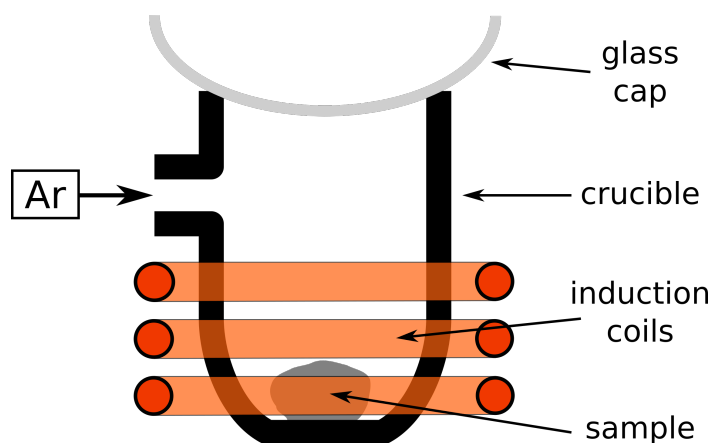


Figure 43. Setup for the induction melting experiments.

Samples of Ni and Ga with a combined mass of approx. 12 g were heated with 560 W power until a homogeneous melt was reached (2-3 min) plus additional 3 min to ensure sufficient mixing. This treatment resulted in pale gold colored nuggets with homogeneous Ni/Ga distribution, as confirmed by EDX elemental mapping (Figure 44).

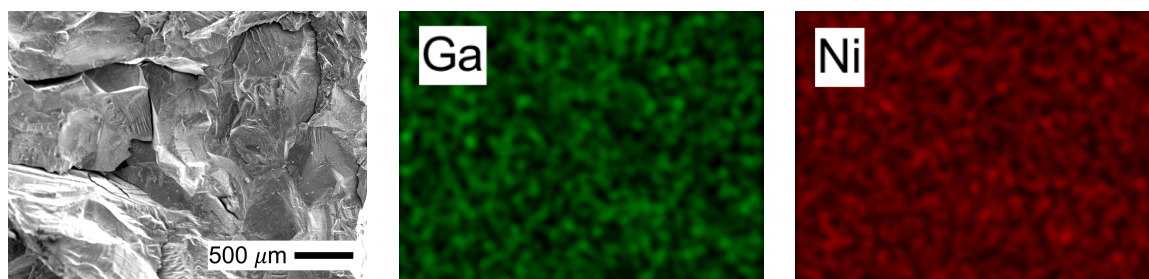


Figure 44. SEM image (left) and EDX element mapping of a fracture surface from an induction melting sample.

Using a Ni/Ga ratio of 1:1 resulted in a phase-pure sample of NiGa (Figure 45). EDX analysis revealed a composition of 47/53 (Ni/Ga) with minimal amounts of carbon and oxygen. The detected carbon signal originates from the used carbon adherent on the sample holder. A contamination of the bulk material with carbon can be ruled out, because all initial materials were tested for impurities and no additional carbon sources were introduced in the process. Since no visible oxidation took place during melting and the EDX spectrum was recorded on a freshly broken chip, the oxygen signal can be assigned to surface-oxidation during sample transfer, which has been reported for Ni/Ga intermetallics before.^[141]

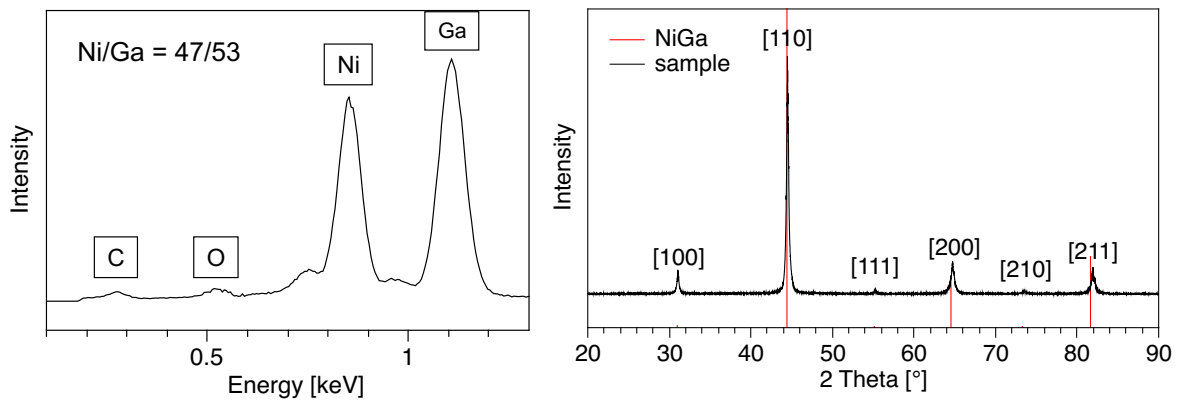


Figure 45. EDX (left) and XRD (right) analysis of a NiGa sample obtained by induction melting.

With a variation of the Ni/Ga ratio to 3:1, also phase pure samples of Ni₃Ga were obtained with a composition of 77/23 (Ni/Ga), determined via EDX (Figure 46).

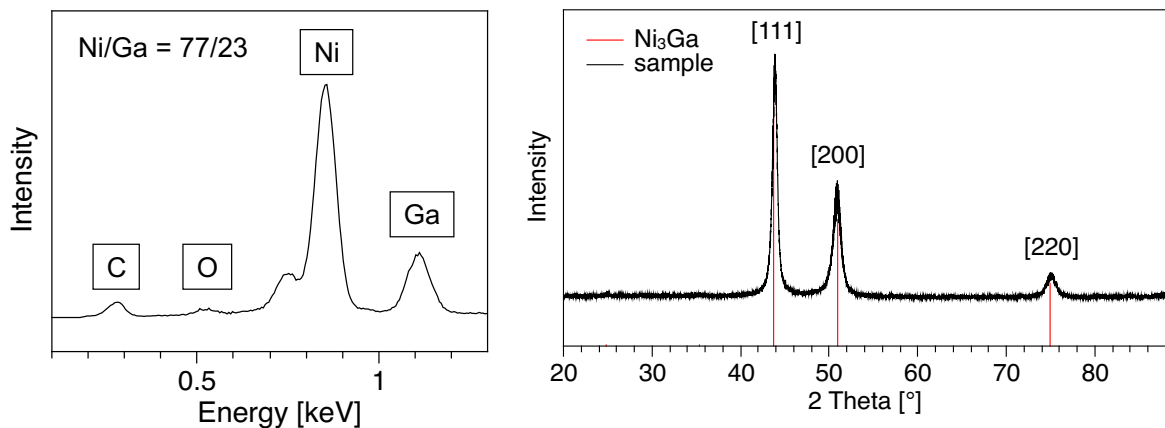


Figure 46. EDX (left) and XRD (right) of a Ni₃Ga sample obtained by induction melting.

The samples prepared via induction melting can be readily applied in an electrochemical setup for mechanistic investigations due to their defined phase composition, minimal amount of impurities as well as homogeneous and unstructured surface. Therefore, optimal conditions for a valid comparison between quantum mechanical calculations and electrochemical experiments are achieved.

6 Conclusion and Outlook

6.1 Quantum Mechanical Calculations

A quantum cluster model was developed to mimic several different surfaces of pure metals and intermetallic phases. Based on all experimentally observed C₁ and C₂ products in the electrochemical CO₂ reduction, a reaction network was deployed and the energies of all intermediates evaluated via DFT on several catalytic surfaces.

A comparison of the obtained energies on a distinct surface, following the paths with the lowest energy barrier, resulted in a mechanistic description for the formation of each product.

Cu

On Cu(211), the mechanism for CH₄ formation involves hydrogenation and dehydration of *CO₂ resulting in *CO, which is then successively hydrogenated at the carbon center, finally forming CH₄. The formation of the main C₂ products C₂H₄ and EtOH involves the dimerization of two *CO as C-C-bond forming step and then follows several hydrogenation and dehydration steps.

The key intermediate was found to be *CO. Its hydrogenation is the rate-determining step in CH₄ production and its dimerization is the rate-determining step in the formation of C₂ products. The respective activation energies for these steps and the CO adsorption energy determine the selectivity between CO, CH₄ and C₂ products. These results agree well with experimental observations found in literature.

The competing hydrogen evolution is one of the main reasons for low Faradaic efficiencies of CO₂RR products and was found to be active on Cu(211), Cu(100) and Cu(111) alike. During CO₂RR it is, however, suppressed by surface coverage with CO, which acts as a catalyst poison.

Ni/Ga

The energetic evaluation on Ni/Ga intermetallics also revealed the conversion of *CO to be the rate determining step for CH_4 production. On NiGa(210), two pathways towards CH_4 are similar in energy. In addition to the pathway determined on Cu(211), hydrogenation of the *OCH_2 intermediate could also take place at the oxygen center, which would result in the *CH_2 and *CH_3 intermediates. The dimerization of *CH_2 and *CH_3 is likely to be the point of C-C-bond formation on NiGa, since the *CO dimerization is much higher in energy than on Cu.

On $Ni_3Ga(211)$, the calculations suggest a mechanism for CH_4 formation, which proceeds through *COH and subsequently *C . The *C is hydrogenated successively forming CH_4 . The preference of *COH over *CHO is caused by the structure-directing properties of Ga in the intermetallic phase and can potentially be used for the design of tailored catalytic materials. Like on NiGa, the formation of C_2 products is expected to be the dimerization of *CH_2 or *CH_3 . Evidence for this mechanism can be found experimentally through the identification of *carbon black* or carbides after a production run.

General

Comparing the adsorption energies of *CO and *CHO on different materials revealed linear scaling relations, which describe their correlation and puts limits on the minimum achievable activation energy. It was found that on any material, destabilizing *CO results in 0.7 times less destabilization of *CHO , which leads to a lower activation energy. On the other hand, destabilizing *CO leads to an easier desorption of CO, thus lowering the selectivity for CH_4 . Since a higher product selectivity is economically more valuable than a reduction in overpotential, the development of new catalysts should focus on moderately strong CO binding sites with up to +180 kJ/mol, since above that value the evolution of H_2 dominates.

Outlook

From the currently available data no scaling relation becomes apparent for *CO dimerization, which needs to be evaluated in more detail in order to enhance the selectivity for C₂ products on Cu. Also, the point of C-C-bond formation on Ni/Ga intermetallics should be evaluated in more detail, since not all possibilities could be addressed in this study. This is advised to be coupled with experimental investigations. If CH₄ and C₂H₆ share a common rate-limiting step on NiGa/Ni₃Ga and *carbon black* or carbides are identified on Ni₃Ga, this would be a sign in favor of the proposed mechanism.

The application of more advanced methods like coupled cluster is not possible for this large system with the available resources, but might be beneficial for a more accurate energetic evaluation. This, however, can be done with an embedded cluster approach, as described by *Kubas et al.*, that reduced the number of explicitly treated atoms.^[172]

6.2 Material Synthesis

CVD

Acetylacetonates of Ni and Ga were applied to deposit thin films of NiGa in a hot-wall MOCVD setup, while a substantial amount of residual carbon remained in the films.

Ni(allyl)Cp and Ga^tBu₃ were successfully applied as precursors in a cold-wall MOCVD setup for the phase-pure deposition of NiGa and Ni₂Ga films with only trace amounts of residual carbon. Further variation in composition led to mixed phases, due to their narrow composition windows. The deposited films exhibit rough surfaces, which are expected to enhance their catalytic activity in the CO₂RR.

Induction Melting

The synthesis of additional Ni/Ga phases via induction melting was examined and led to the production of phase-pure NiGa and Ni₃Ga. Those clean samples will show no catalytic effects due to impurities and surface structuring, which is necessary for a valid comparison between theory and experiment.

Outlook

For the electrochemical evaluation of the produced materials a cooperation with the group of Prof. M. Behrens is arranged. But due to a lack of specialized equipment, the evaluation could not take place in the time frame of this thesis.

While the induction melting samples are expected to reproduce the computational findings, the rough structure of the CVD films might enhance their catalytic activity. Induction melting was found to be a reliable method for the synthesis of distinct phases, since the intended composition can be determined exactly and it will therefore be applied in the synthesis of additional metallic materials.

7 Methods and Materials

7.1 General

The experimental work was executed in the group of Prof. Dr. Stephan Schulz at the University of Duisburg-Essen, Institute of Inorganic Chemistry, Universitätsstraße 7, 45141 Essen.

The quantum chemical calculations were conducted on resources of the Schulz group at the University of Duisburg-Essen and of the Max Planck Institute for Chemical Energy Conversion in Mülheim.

7.2 Computational Details

The total energies of the adsorbates on different surfaces have been calculated with DFT using a cluster ansatz in the *ORCA 4.0* program.^[173] Calculations have been performed using the *revised Perdew, Burke and Ernzerhof* (RPBE) exchange-correlation functional^[85] and *Ahlrichs'* def2-TZVP basis set.^[174] In order to account for dispersion effects, *Grimme's* atom-pairwise dispersion correction with the *Becke-Johnson* damping scheme (DFT-D3) was included.^[97,175]

In all calculations, surfaces were modeled using a cluster with two layers of atoms, surrounding the central 5-atom (211)/(210) or 4-atom (111) motive, thus consisting of 64-65 atoms. The coordinates of the outermost layer were constrained in space, to account for rigidity in the crystal structure. All other atoms were allowed to relax freely. The electrolyte was incorporated implicitly with the *conductor-like polarizable continuum model* (CPCM), using the dielectric constant of water ($\epsilon = 80.4$).^[98]

The *computational hydrogen electrode* (CHE) model was used to calculate the free energy of reaction intermediates with respect to the energy of adsorbates and the applied potential (U).^[176] This model uses the definition, that the chemical potential of a transferred proton-electron pair equals half the potential of a hydrogen molecule H_2 at standard pressure and is defined as 0 V vs the *reversible hydrogen electrode* (RHE) at all pH values. The free energy of the reaction is corrected for the applied potential by the term $-eU$, with e being the absolute value of the elementary charge, leading to the total equation

$$\Delta E = E(AH^*) - E(A^*) - \left(\frac{1}{2}E(H_2) - eU\right)$$

In this model, the onset potential for the generation of a specific product, is the potential needed in order to make all steps in the mechanism exothermic. In a broad screening, only the reaction energies were considered as a measure for the reaction pathway, as activation energies were expected to be in the same order for all protonation reactions. The activation energies for the relevant steps were approximated by a relaxed surface scan of the corresponding C/O-H bond. Since those reactions are chemically similar on the investigated surfaces, the individual activation energies were extrapolated to other materials following the *Bell-Evans-Polanyi* principle.^[135,136] In this study only the direct hydrogen transfer from the surface was evaluated, therefore the mentioned activation energies can be seen as an upper limit of the actual value.

7.3 Analytics

EDX and SEM

Energy dispersive X-ray spectroscopy and scanning electron microscopy analyses were conducted on a JSM-6510 (Joel) device with tungsten cathode and EDX unit (Bruker).

XRD

X-ray diffractograms were recorded on a D8 ADVANCE (Bruker) device with Cu-K_α radiation and a Lynx Eye detector (Bruker).

DSC

Differential scanning calorimetry analyses were conducted on a DSC 200 PC Netzsch device in sealed aluminum crucible.

NMR

NMR spectra were recorded on a DMX 300 MHz spectrometer from *Bruker* with the residual solvent peak as the internal reference.

7.4 Chemical Vapor Deposition

For the deposition experiments one cold-wall and one hot-wall MOCVD-reactor were used. The atmosphere inside both reactors was adjusted by gas flow controllers (MKS Instruments, 0.3 to 100 sccm) and oil- or membrane vacuum pumps at the outlet.

In the hot-wall reactor (Figure 47), the carrier gas consists of argon as an inert gas and a reactive gas like H_2 or O_2 . The gas flow controllers are attached to a quartz tube which is rested in a tube furnace. The precursor container and substrate are then placed inside the tube at distinct positions. Depending on the oven temperature, the precursor container is positioned in the temperature gradient zone at the end of the oven, in order to provide a controlled sublimation without decomposition. The substrate is placed in the center of the oven, in order to guarantee peak temperature and no gradient. This leads to material deposition on the substrate and tube in that zone. Volatile decomposition products are then directed through a cold trap before the gas stream enters the pump.

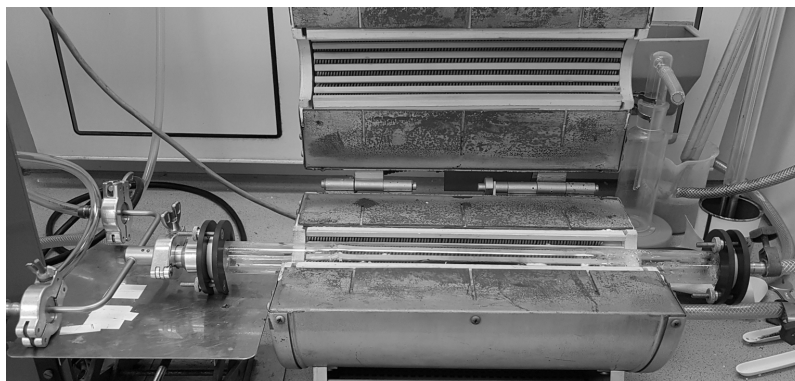


Figure 47. Schematic illustration and photo of the hot-wall reactor used during this project.

In the cold-wall reactor (Figure 48), liquid precursors are used in a bubbler system, which saturates the carrier gas with the precursors. The flow rates through each bubbler system are adjusted individually, in order to control the stoichiometry of the precursors in the gas phase. The supply pipes are heated resistively and are combined right before entering the reaction chamber, in order to avoid condensation of the precursors and preliminary reaction in the gas-phase. The gas stream in the reaction chamber is then guided over the substrate, which is selectively heated by a ceramic plate heating element. Volatile decomposition products are then directed through a cold trap before the gas stream enters the pump.

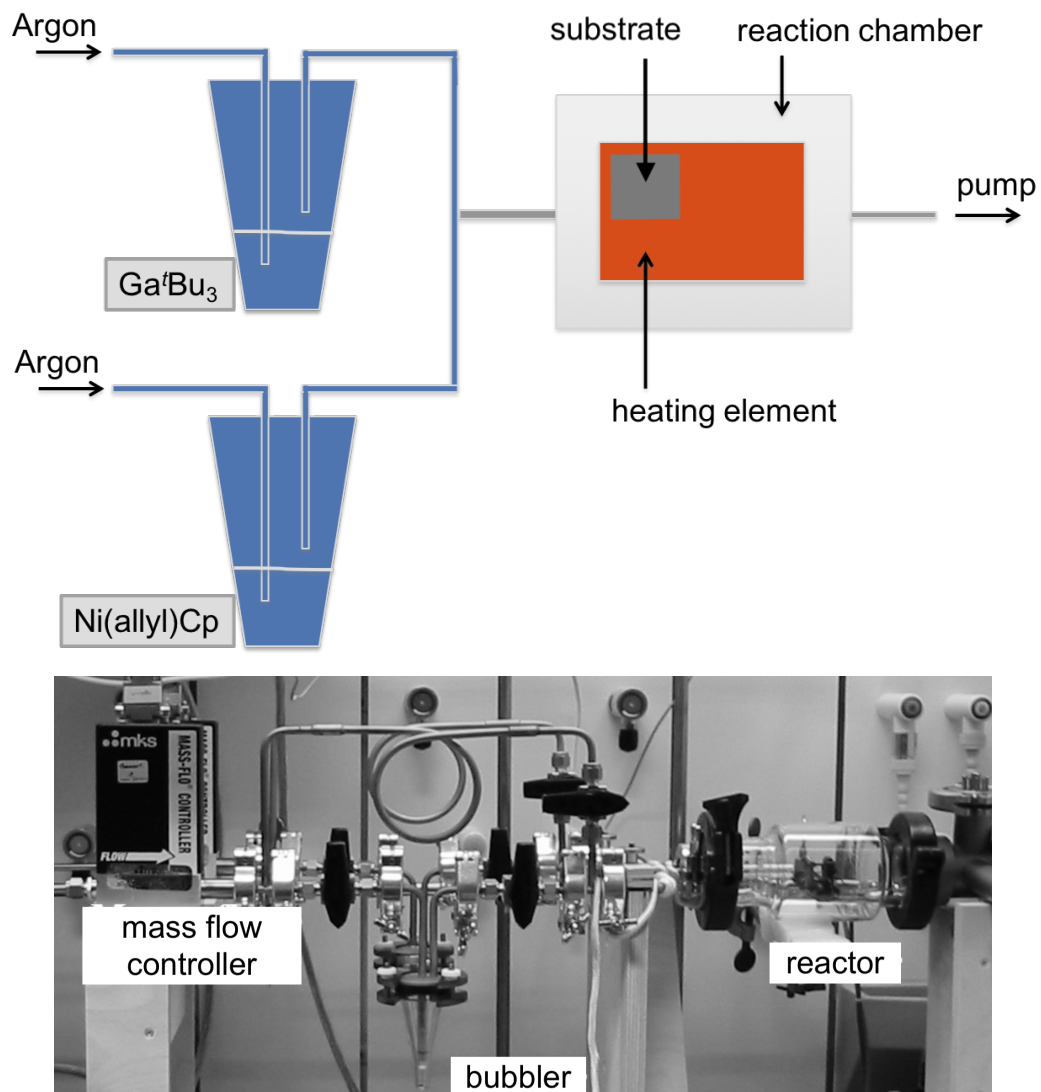


Figure 48. Schematic illustration and photo of the cold-wall CVD setup, containing two bubbler systems and the reaction chamber with heating element and substrate.

7.5 Induction Melting

In an induction furnace, the required heat to melt metals is introduced via electromagnetic induction. A powerful alternating current runs through water-cooled copper coils, surrounding the crucible, which creates a rapidly reversing magnetic field. This magnetic field in turn creates eddy currents inside the metal, which heats up due to its resistivity and, in cases of ferromagnetic materials, due to magnetic hysteresis. Once melted, the induced eddy currents provide continuous stirring, thus ensuring sufficient mixing (Figure 49).

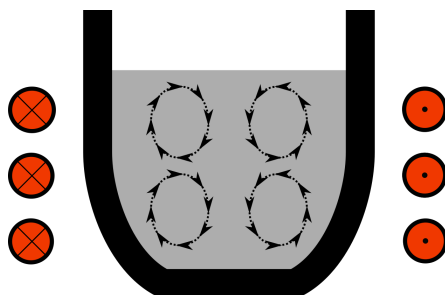


Figure 49. Stirring, introduced through electromagnetic induction.

An UltraFlex EasyMelt-1P (2.8 kW, 60 Hz) induction furnace was used for the induction melting experiments. The quartz crucible was modified to accept an argon pipe as well as a flask as lid, in order to reduce the oxygen content of the atmosphere during melting (Figure 50).



Figure 50. Induction oven used in the induction melting experiments (left) and a close-up of the modified crucible (right).

7.6 X-Ray Diffraction

X-ray diffraction (XRD) is a bulk-sensitive, non-destructive technique for the analysis of (partially) crystalline samples. It allows for qualitative and quantitative phase analysis, the determination of cell parameters as well as grain size and stress.

For the diffraction of radiation to occur, its wavelength must be in the range of the interatomic distance in crystalline materials. This is why, under certain circumstances, diffraction can be observed when X-rays pass the periodically allocated structures of a crystal (Figure 51).

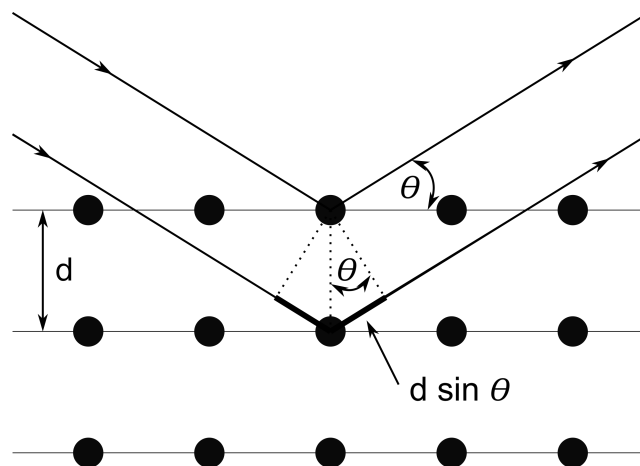


Figure 51. Illustration of diffraction in a crystal lattice.

Bragg's law describes the conditions under which constructive interference occurs:

$$n\lambda = 2d \cdot \sin \theta$$

with a positive integer n , the wavelength λ , the interplanar distance d and the incident angle θ .

In practice, monochromatic Cu- K_α radiation with a wavelength of $\lambda = 1.5418 \text{ \AA}$ is used for XRD measurements in most cases. To generate Cu- K_α radiation, an electron beam is accelerated in an electric field and directed onto a copper anode. In addition to the continuous bremsstrahlung, K_α and K_β radiation is produced and filtered by a monochromator allowing only the Cu- K_α radiation to pass.

The intensity of the diffracted radiation is then detected as a function of its angle against the primary beam.

The measured diffractogram can be used for the identification of already known phases by comparison with reflex position and intensities in databases, or for determining the structural parameters of new phases.

7.7 Electron Microscopy

Electron microscopes utilize accelerated electrons with wavelengths substantially below those of visible light. This way, a much higher resolution in the nanometer scale can be achieved. The maximum resolution of microscopes is determined by the *Abbe* diffraction limit:

$$d = \frac{\lambda}{2n \cdot \sin \alpha}$$

With the minimum distance between two observable points d , the wavelength of the radiation λ , the diffraction index of the medium n , and the half angle α . Therefore, higher resolution can be achieved with lower wavelengths.

The required electrons are emitted from an electron gun in high-vacuum equipped with a filament cathode, often consisting of tungsten. They are then focused by condenser lenses and deflected in the x and y axes in order to scan the specimen's surface in a raster fashion.

This primary electron beam loses energy through interaction with the sample by scattering and absorption (Figure 52). The size of the tear-drop shaped interaction volume depends on the electron's kinetic energy as well as the specimen's density and atomic number and ranges from under 100 nm to approximately 5 μm into the sample.

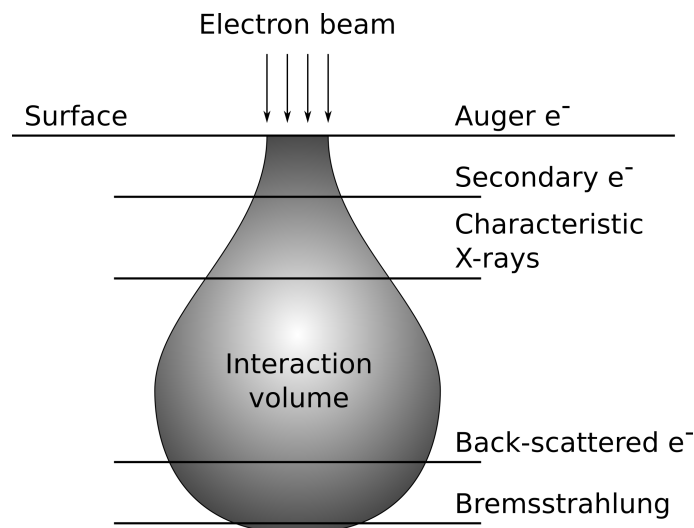


Figure 52. Interaction volume of electrons with the sample in electron microscopes and the origin zones of detectable radiation.

The energy exchange results in elastically back scattered electrons, inelastically scattered secondary electrons and electromagnetic radiation which can be analyzed with various techniques in order to gain information about the specimen's morphology and composition.

In a *scanning electron microscopy* (SEM) setup, either the secondary or backscattered electrons are detected and the resulting voltage is amplified. The changing current at various positions of the electron beam on the sample is then displayed as a variation of brightness on the monitor, resulting in an image of the sample.

7.8 Energy-Dispersive X-Ray Spectroscopy

Often coupled with SEM, *energy-dispersive X-ray spectroscopy* (EDX) can deliver a space-resolved and non-destructive elemental composition analysis of a sample's surface.

The interaction between the primary electron beam and the specimen leads to the formation of secondary and backscattered electrons as well as Auger-electrons and X-rays (Figure 53). While secondary and backscattered electrons are used for imaging, Auger-electrons and the characteristic X-rays are analyzed via different techniques with regard to the elemental composition of the sample.

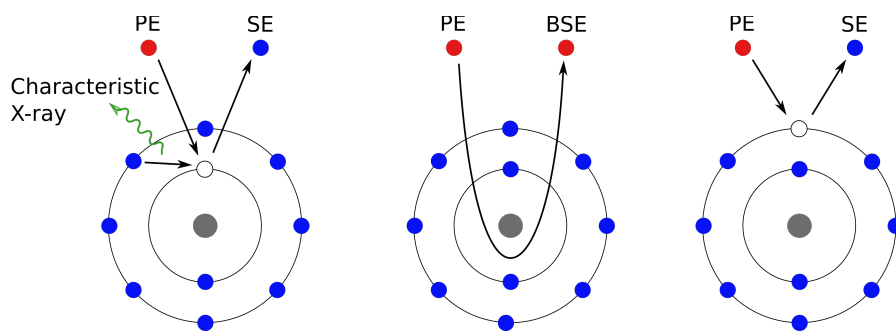


Figure 53. Illustration of the formation of *secondary electrons* (SE), characteristic X-rays, and *back-scattered electrons* (BSE) created by the interactions of *primary electrons* (PE) with the atoms of the sample.

The characteristic X-rays used for EDX are generated when a high-energy primary electron ejects an electron from an inner shell through inelastic scattering and an electron from an outer, higher-energy shell fills the hole. The energy difference between the outer and inner shell is emitted as an X-ray quant and can be collected by a semiconductor detector. The energy of this X-ray quant is characteristic for the specific shell transition and can be assigned to a certain element. Through the intensity distribution of different peaks, also a quantitative statement can be made, regarding the composition. The likelihood of an X-ray quant leaving the sample, and thus being able to be detected, depends on the distance and density of the material it has to travel through as well as the X-ray's energy. Therefore, accurate assumptions on the composition can only be made after a quantitative correction procedure.^[177]

7.9 Syntheses

7.9.1 Inert Atmosphere

Oxygen or moisture sensitive reactions were carried out under an argon atmosphere using standard *Schlenk* techniques. The argon (Air Liquide, purity grade 5.0) was led through molecular sieve (4 Å), through SICAPENT (phosphorus pentoxide with moisture indicator) and twice through a 60 °C warm BTS catalyst. Glassware was stored in a 140 °C hot drying cabinet prior to use.

7.9.2 Solvents

Diethyether, pentane and toluene were dried in a MB-SPS-800 solvent drying system made by *MBRAUN*. THF was dried over sodium/potassium and distilled under argon atmosphere.

Deuterated solvents were degassed using the “*pump-freeze-thaw*” technique and stored over molecular sieve (4 Å).

7.9.3 Chemicals

Gallium was purchased from Alfa Aesar at 99.9% trace metal basis.

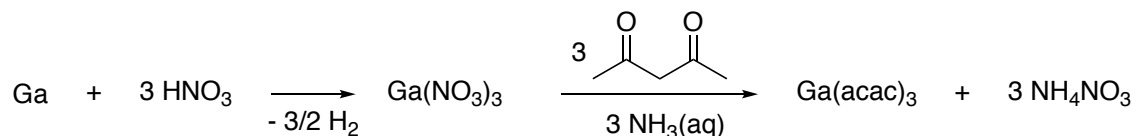
Nickel was purchased from Alfa Aesar at 99.98% trace metal basis.

Cu(acac)₂ was purchased from Sigma Aldrich at >99.9% trace metal basis.

Ni(acac)₂ was purchased from Alfa Aesar at >95% purity.

Unless otherwise noted all liquids used under inert conditions were degassed and stored over molecular sieve (4 Å).

Synthesis of Gallium Acetylacetonate Ga(acac)₃

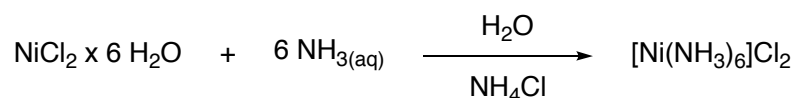


Protocol adapted from *Birnara et al.*^[163]

Concentrated nitric acid (70 ml) was added to gallium (7.0 g, 100 mmol, 1.0 equiv.) and stirred until the gallium was consumed completely (approx. 3 h). NH_{3(aq)} (30%) was added to the solution until pH 4. Ethanol (20 ml) and acetylacetonone (30.8 ml, 200 mmol, 3.0 equiv.) were added and the solution was heated to reflux for 3 h. The precipitate was filtered off and dried in high vacuum to yield 27.0 g (73.6 mmol, 74%) of Ga(acac)₃ as a white powder.

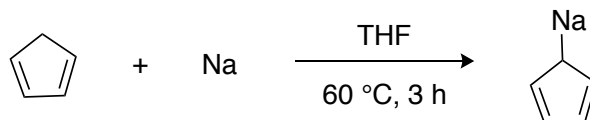
Synthesis of Allylcyclopentadienylnickel Ni(allyl)(Cp)

Hexaaminenickel(II) chloride [Ni(NH₃)₆]Cl₂



Protocol adapted from *Hecht*.^[178]

Nickel chloride hexahydrate (12.2 g, 51.3 mmol) was dissolved in 9 ml H₂O. Saturated NH₄Cl solution (12 ml) and aqueous NH₃ solution (30%, 25 ml) were added and the resulting violet suspension was cooled to 0 °C. The suspension was filtered, the solid was washed with aqueous NH₃ solution and dried in a desiccator. 10.9 g (46.8 mmol, 91%) of [Ni(NH₃)₆]Cl₂ were isolated as a dark violet powder.

Cyclopentadienyl Sodium NaCp

Protocol adapted from *Panda et al.*^[179]

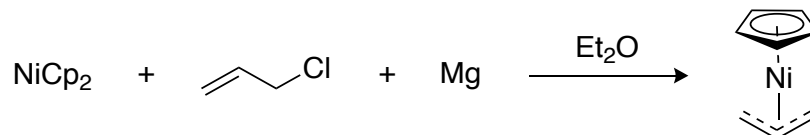
Freshly cracked cyclopentadiene (220 ml, 2.66 mol, 1.1 equiv.) was added to a suspension of sodium (55.7 g, 2.42 mol, 1.0 equiv.) in THF (300 ml) and heated to 60 °C for 3 h during which all of the sodium was consumed. The THF and excessive cyclopentadiene were removed in vacuo, resulting in 198 g (2.25 mol, 93%) of NaCp as a white powder.

Cyclopentadienyl Nickel NiCp₂

Protocol adapted from *Ritleng et al.*^[180]

NaCp (61.8 g, 701 mmol, 2.5 equiv.) was dissolved in THF (150 ml) and [Ni(NH₃)₆]Cl₂ (65.0 g, 280 mmol, 1.0 equiv.) was added to the mixture. The solution was heated to reflux for 2 h, converting the purple solution into a dark green solution with a grey precipitate. After cooling to room temperature, the suspension was filtered and the THF was removed in vacuo. The remaining green solid was sublimed, resulting in 42 g (222 mmol, 79%) of NiCp₂.

Allylcyclopentadienylnickel Ni(allyl)(Cp)

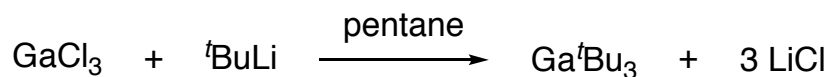


Protocol adapted from *Pasynkiewicz et al.*^[181]

Et₂O (100 ml) was added to 5.86 g (241 mmol, 2.3 equiv.) of magnesium turnings. Allyl chloride (13.1 ml, 161 mmol, 1.5 equiv.) in 100 ml Et₂O was added dropwise without stirring under retention of a reactive flux. After complete addition, the mixture was diluted with Et₂O to a total volume of 250 ml and heated to reflux for 12 h. NiCp₂ (20 g, 106 mmol, 1.0 equiv.) was dissolved in Et₂O and added at room temperature. The mixture was heated to reflux for 2 h and was filtered afterwards. Et₂O was removed from the filtrate under reduced pressure and the residue distilled. At 10 mbar and 68-75 °C, 10.4 g of Ni(allyl)(Cp) (63.1 mmol, 60%) were collected as a deep violet viscous liquid.

¹H NMR (300 MHz, CDCl₃): δ/ppm = 5.17 (s, Cp-H, 5 H), 4.96 (p, ³J_{HH} = 11 Hz, C-CH-C, 1 H), 2.67 (d, ³J_{HH} = 11 Hz, -CH₂, 4 H).

Synthesis of Tritertbutylgallium Ga^tBu₃



Protocol adapted from Cowley *et al.*^[182]

GaCl₃ (5.06 g, 28.7 mmol, 1.0 equiv.) was dissolved in 10 ml toluene and cooled to –30 °C. ^tBuLi (45.4 ml, 1.9 M in pentane, 86.2 mmol, 3.0 equiv.) was added dropwise over the course of 45 min at this temperature. The mixture was allowed to slowly warm up to room temperature and was stirred for 12 h.

The suspension was filtered and the solvent was removed in vacuo. During distillation, 3.60 g of Ga^tBu₃ (14.9 mmol, 52%) were isolated at 10 mbar and 78 °C as a colorless liquid.

¹H NMR (300 MHz, CDCl₃): δ/ppm = 1.15 (s, 27 H).



8 References

- [1] “<https://www.iea.org/statistics/kwes/emissions/>,” **2018**.
- [2] “<https://climate.nasa.gov/>,” **2018**.
- [3] M. Meinshausen, N. Meinshausen, W. Hare, S. C. B. Raper, K. Frieler, R. Knutti, D. J. Frame, M. R. Allen, *Nature* **2009**, *458*, 1158–1162.
- [4] W. P. Nel, C. J. Cooper, *Energy Policy* **2009**, *37*, 166–180.
- [5] M. Höök, A. Sivertsson, K. Aleklett, *Nat. Resour. Res.* **2010**, *19*, 63–81.
- [6] C. Le Quéré, R. M. Andrew, J. G. Canadell, S. Sitch, J. Ivar Korsbakken, G. P. Peters, A. C. Manning, T. A. Boden, P. P. Tans, R. A. Houghton, R. Keeling, S. Alin, O. Andrews, P. Anthony, L. Barbero, L. Bopp, F. Chavallier, L. Chini, P. Ciais, K. Currie, C. Delire, S. Doney, P. Friedlingstein, T. Gkritzalis, I. Harris, J. Hauck, V. Haverd, M. Hoppema, K. Klein Goldewijk, A. Jain, E. Kato, A. Körtzinger, P. Landschützer, N. Lefèvre, A. Lenton, S. Lienert, D. Lombardozzi, J. Melton, N. Metzl, F. Millero, P. Monteiro, D. Munro, J. Nabel, S. Nakaoka, K. O'Brien, A. Olsen, A. Omar, T. Ono, D. Pierrot, B. Poulter, C. Rödenbeck, J. Salisbury, U. Schuster, J. Schwinger, R. Séférian, I. Skjelvan, B. Stocker, A. Sutton, T. Takahashi, H. Tian, B. Tilbrook, I. Van Der Laan-Luijkx, G. Van Der Werf, N. Viovy, A. Walker, A. Wiltshire, S. Zaehle, *Earth Syst. Sci. Data* **2016**, *8*, 605–649.
- [7] J. Artz, T. E. Müller, K. Thenert, J. Kleinekorte, R. Meys, A. Sternberg, A. Bardow, W. Leitner, *Chem. Rev.* **2018**, *118*, 434–504.
- [8] F. A. Rahman, M. M. A. Aziz, R. Saidur, W. A. W. A. Bakar, M. R. Hainin, R. Putrajaya, N. A. Hassan, *Renew. Sustain. Energy Rev.* **2017**, *71*, 112–126.
- [9] E. Dlugokencky, P. Tans, “NOAA/ESRL,” can be found under www.esrl.noaa.gov/gmd/ccgg/trends/, **2018**.
- [10] M. Aresta, A. Dibenedetto, A. Angelini, *Chem. Rev.* **2014**, *114*, 1709–1742.
- [11] P. Markewitz, W. Kuckshinrichs, W. Leitner, J. Linssen, P. Zapp, R.

-
- Bongartz, A. Schreiber, T. E. Müller, *Energy Environ. Sci.* **2012**, *5*, 7281–7305.
- [12] M. Alvarez-Guerra, J. Albo, E. Alvarez-Guerra, A. Irabien, *Energy Environ. Sci.* **2015**, *8*, 2574–2599.
- [13] W. Keim, *Carbon Dioxide as a Source of Carbon*, Springer Netherlands, Dordrecht, **1987**.
- [14] W. Leitner, *Coord. Chem. Rev.* **1996**, *153*, 257–284.
- [15] P. Sabatier, Senderens, *J. Soc. Chem. Ind.* **1902**, *21*, 504–506.
- [16] M. Götz, J. Lefebvre, F. Mörs, A. McDaniel Koch, F. Graf, S. Bajohr, R. Reimert, T. Kolb, *Renew. Energy* **2016**, *85*, 1371–1390.
- [17] C. Ratnasamy, J. P. Wagner, *Catal. Rev.* **2009**, *51*, 325–440.
- [18] F. Fischer, H. Tropsch, *Chem. Ber.* **1926**, *59*, 832–836.
- [19] N. Armaroli, V. Balzani, *Angew. Chemie* **2007**, *119*, 52–67.
- [20] N. Armaroli, V. Balzani, *Angew. Chemie - Int. Ed.* **2007**, *46*, 52–66.
- [21] G. W. Crabtree, M. S. Dresselhaus, M. V. Buchanan, *Phys. Today* **2004**, *57*, 39–44.
- [22] X. Zou, Y. Zhang, *Chem. Soc. Rev.* **2015**, *44*, 5148–5180.
- [23] J. Klankermayer, S. Wesselbaum, K. Beydoun, W. Leitner, *Angew. Chemie - Int. Ed.* **2016**, *55*, 7296–7343.
- [24] J. Klankermayer, S. Wesselbaum, K. Beydoun, W. Leitner, *Angew. Chemie* **2016**, *128*, 7416–7467.
- [25] H. Ooka, M. C. Figueiredo, M. T. M. Koper, *Langmuir* **2017**, *33*, 9307–9313.
- [26] J. Hagen, in *Ind. Catal.*, Wiley-VCH Verlag GmbH & Co. KGaA, Weinheim, Germany, **2015**, 459–462.
- [27] A. M. Klibanov, *Nature* **2001**, *409*, 241–246.
- [28] Y. Zhang, J. Ge, Z. Liu, *ACS Catal.* **2015**, *5*, 4503–4513.
- [29] J. H. Jones, *Platin. Met. Rev.* **2000**, *44*, 94–105.
- [30] P. Cossee, *J. Catal.* **1964**, *3*, 80–88.
- [31] J. Smidt, W. Hafner, R. Jira, R. Sieber, J. Sedlmeier, A. Sabel, *Angew. Chemie Int. Ed.* **1962**, *1*, 80–88.
- [32] J. Smidt, W. Hafner, R. Jira, R. Sieber, J. Sedlmeier, A. Sabel, *Angew. Chemie* **1962**, *74*, 93–102.

- [33] O. Deutschmann, H. Knözinger, K. Kochloefl, T. Turek, *Ullmann's Encycl. Ind. Chem.* **2012**, 223–269.
- [34] M. Behrens, F. Studt, I. Kasatkin, S. Kuhl, M. Havecker, F. Abild-Pedersen, S. Zander, F. Girgsdies, P. Kurr, B.-L. Kniep, M. Tovar, R. Fischer, J. K. Nørskov, R. Schlögl, *Science* **2012**, 336, 893–897.
- [35] F. Studt, F. Abild-Pedersen, Q. Wu, A. D. Jensen, B. Temel, J. D. Grunwaldt, J. K. Nørskov, *J. Catal.* **2012**, 293, 51–60.
- [36] F. Studt, I. Sharafutdinov, F. Abild-Pedersen, C. F. Elkjær, J. S. Hummelshøj, S. Dahl, I. Chorkendorff, J. K. Nørskov, *Nat. Chem.* **2014**, 6, 320–324.
- [37] G. A. Olah, *Angew. Chemie* **2005**, 117, 2692–2696.
- [38] G. A. Olah, *Angew. Chemie Int. Ed.* **2005**, 44, 2636–2639.
- [39] G. A. Olah, A. Goepfert, G. K. S. Prakash, *J. Org. Chem.* **2009**, 74, 487–498.
- [40] S. Rönsch, J. Schneider, S. Matthischke, M. Schlüter, M. Götz, J. Lefebvre, P. Prabhakaran, S. Bajohr, *Fuel* **2016**, 166, 276–296.
- [41] K. Zhao, Q. Bkour, X. Hou, S. W. Kang, J. C. Park, M. G. Norton, J. II Yang, S. Ha, *Chem. Eng. J.* **2018**, 336, 20–27.
- [42] P. Forzatti, E. Tronconi, I. Pasquon, *Catal. Rev.* **1991**, 33, 109–168.
- [43] X. Chang, T. Wang, J. Gong, *Energy Environ. Sci.* **2016**, 9, 2177–2196.
- [44] J. Hong, W. Zhang, J. Ren, R. Xu, *Anal. Methods* **2013**, 5, 1086–1097.
- [45] S. N. Habisreutinger, L. Schmidt-Mende, J. K. Stolarczyk, *Angew. Chemie* **2013**, 125, 7516–7557.
- [46] S. N. Habisreutinger, L. Schmidt-Mende, J. K. Stolarczyk, *Angew. Chemie - Int. Ed.* **2013**, 52, 7372–7408.
- [47] Z. Xiong, Z. Lei, Y. Li, L. Dong, Y. Zhao, J. Zhang, *J. Photochem. Photobiol. C Photochem. Rev.* **2018**, 36, 24–47.
- [48] M. Shen, L. Zhang, J. Shi, *Nanotechnology* **2018**, 29, 412001–412012.
- [49] T. Zhang, W. Lin, *Chem. Soc. Rev.* **2014**, 43, 5982–5993.
- [50] Y. Hori, A. Murata, R. Takahashi, *J. Chem. Soc. Faraday Trans. 1 Phys. Chem. Condens. Phases* **1989**, 85, 2309–2326.
- [51] K. P. Kuhl, E. Cave, D. N. Abram, T. F. Jaramillo, *Energy Environ. Sci.* **2012**, 5, 7050–7059.

-
- [52] S. Lee, D. Kim, J. Lee, *Angew. Chemie - Int. Ed.* **2015**, *54*, 14701–14705.
- [53] S. Lee, D. Kim, J. Lee, *Angew. Chemie* **2015**, *127*, 14914–14918.
- [54] R. Kortlever, I. Peters, C. Balemans, R. Kas, Y. Kwon, G. Mul, M. T. M. Koper, *Chem. Commun.* **2016**, *52*, 10229–10232.
- [55] D. D. Zhu, J. L. Liu, S. Z. Qiao, *Adv. Mater.* **2016**, *28*, 3423–3452.
- [56] Y. Hori, K. Kikuchi, S. Suzuki, *Chem. Lett.* **1985**, *14*, 1695–1698.
- [57] A. Dutta, C. E. Morstein, M. Rahaman, A. Cedeño López, P. Broekmann, *ACS Catal.* **2018**, *8*, 8357–8368.
- [58] J. He, N. J. Johnson, A. Huang, C. Berlinguette, *ChemSusChem* **2017**, *48–57*.
- [59] D. M. Dobkin, M. K. Zuraw, *Principles of Chemical Vapor Deposition*, Springer Netherlands, Dordrecht, **2003**.
- [60] S. Y. Lee, P. Nash, P. Nash, *ASM Int. Mater. Park. OH* **1991**, 133–140.
- [61] H. Okamoto, *J. Phase Equilibria Diffus.* **2008**, *29*, 296.
- [62] B. Predel, in *Ga-Gd -- Hf-Zr* (Ed.: O. Madelung), Springer Berlin Heidelberg, Berlin, Heidelberg, **1996**.
- [63] A. U. Seybolt, J. H. Westbrook, *Acta Metall.* **1964**, *12*, 449–460.
- [64] J. N. Pratt, J. M. Bird, *J. Phase Equilibria* **1993**, *14*, 465–472.
- [65] L.-S. Hsu, Y. D. Yao, Y. Y. Chen, *Mod. Phys. Lett. B* **1997**, *11*, 407–414.
- [66] R. Ducher, R. Kainuma, K. Ishida, *Intermetallics* **2007**, *15*, 148–153.
- [67] J. A. Leiro, M. H. Heinonen, *Surf. Sci.* **1996**, *346*, 73–78.
- [68] Li-Shing Hsu, R. S. Williams, *J. Phys. Chem. Solids* **1994**, *55*, 305–312.
- [69] B. Guenais, A. Poudoulec, J. Caulet, A. Guivarc'h, *J. Cryst. Growth* **1990**, *102*, 925–932.
- [70] C. Li, Y. Chen, S. Zhang, J. Zhou, F. Wang, S. He, M. Wei, D. G. Evans, X. Duan, *ChemCatChem* **2014**, *6*, 824–831.
- [71] K. Schütte, A. Doddi, C. Kroll, H. Meyer, C. Wiktor, C. Gemel, G. van Tendeloo, R. A. Fischer, C. Janiak, *Nanoscale* **2014**, *6*, 5532–5544.
- [72] P. A. M. Dirac, *Proc. R. Soc. A Math. Phys. Eng. Sci.* **1929**, *123*, 714–733.
- [73] M. Born, R. Oppenheimer, *Ann. Phys.* **1927**, *389*, 457–484.
- [74] D. Sholl, J. Steckel, *Density Functional Theory: A Practical Introduction*, John Wiley And Sons, Hoboken, NJ, **2009**.
- [75] J.-L. Bretonnet, *AIMS Mater. Sci.* **2017**, *4*, 1372–1405.

- [76] P. Hohenberg, W. Kohn, *Phys. Rev.* **1964**, *136*, B864–B871.
- [77] W. Kohn, L. J. Sham, *Phys. Rev.* **1965**, *140*, A1133–A1138.
- [78] R. P. Feynman, *Phys. Rev.* **1939**, *56*, 340–343.
- [79] E. Matito, D. Casanova, X. Lopez, J. M. Ugalde, *Theor. Chem. Acc.* **2016**, *135*, 1–4.
- [80] B. Teng, X. Wen, M. Fan, F. Wu, Y. Zhang, *Phys. Chem. Chem. Phys.* **2014**, *16*, 18563–18569.
- [81] J. P. Perdew, A. Zunger, *Phys. Rev. B* **1981**, *23*, 5048–5079.
- [82] J. P. Perdew, K. Burke, M. Ernzerhof, *Phys. Rev. Lett.* **1996**, *77*, 3865–3868.
- [83] S. Grimme, *J. Comput. Chem.* **2006**, *27*, 1787–1799.
- [84] N. Q. Su, X. Xu, *Annu. Rev. Phys. Chem.* **2017**, *68*, 155–182.
- [85] B. Hammer, L. B. Hansen, J. K. Nørskov, *Phys. Rev. B* **1999**, *59*, 7413–7421.
- [86] K. Kim, K. D. Jordan, *J. Phys. Chem.* **1994**, *98*, 10089–10094.
- [87] F. Jensen, *Wiley Interdiscip. Rev. Comput. Mol. Sci.* **2013**, *3*, 273–295.
- [88] R. E. Stratmann, G. E. Scuseria, M. J. Frisch, *J. Chem. Phys.* **1998**, *109*, 8218–8224.
- [89] N. Mardirossian, M. Head-Gordon, *Mol. Phys.* **2017**, *115*, 2315–2372.
- [90] A. D. Becke, *Phys. Rev. A* **1988**, *38*, 3098–3100.
- [91] C. Lee, W. Yang, R. G. Parr, *Phys. Rev. B* **1988**, *37*, 785–789.
- [92] K. Burke, *J. Chem. Phys.* **2012**, *136*, 150901.
- [93] R. Holze, *Electrochemical Thermodynamics and Kinetics*, Springer Berlin Heidelberg, Berlin, Heidelberg, **2007**.
- [94] L. C. Grabow, M. Mavrikakis, *ACS Catal.* **2011**, *1*, 365–384.
- [95] O. Deutschmann, *Modeling and Simulation of Heterogeneous Catalytic Reactions: From the Molecular Process to the Technical System*, Wiley-VCH, **2011**.
- [96] E. R. Johnson, I. D. Mackie, G. A. DiLabio, *J. Phys. Org. Chem.* **2009**, *22*, 1127–1135.
- [97] S. Grimme, J. Antony, S. Ehrlich, H. Krieg, *J. Chem. Phys.* **2010**, *132*, 154104.
- [98] V. Barone, M. Cossi, *J. Phys. Chem. A* **1998**, *102*, 1995–2001.

-
- [99] M. Petrantoni, A. Hemeryck, J. M. Ducéré, A. Estève, C. Rossi, M. Djafari Rouhani, D. Estève, G. Landa, *J. Phys. Chem. Solids* **2010**, *71*, 130–133.
- [100] R. T. Downs, M. Hall-Wallace, *Am. Mineral.* **2003**, *88*, 247–250.
- [101] M. D. Hanwell, D. E. Curtis, D. C. Lonie, T. Vandermeersch, E. Zurek, G. R. Hutchison, *J. Cheminform.* **2012**, *4*, 1-17.
- [102] L. Zhang, Z.-J. Zhao, J. Gong, *Angew. Chemie* **2017**, *129*, 11482–11511.
- [103] L. Zhang, Z.-J. Zhao, J. Gong, *Angew. Chemie Int. Ed.* **2017**, *56*, 11326–11353.
- [104] R. A. van Santen, *Modern Heterogeneous Catalysis*, Wiley-VCH Verlag GmbH & Co. KGaA, Weinheim, Germany, **2017**.
- [105] Y. Hori, *Mod. Asp. Electrochem.* **2008**, 89–189.
- [106] C. W. Li, J. Ciston, M. W. Kanan, *Nature* **2014**, *508*, 504–507.
- [107] C. W. Li, M. W. Kanan, *J. Am. Chem. Soc.* **2012**, *134*, 7231–7234.
- [108] K. Manthiram, B. J. Beberwyck, A. P. Alivisatos, *J. Am. Chem. Soc.* **2014**, *136*, 13319–13325.
- [109] F. S. Roberts, K. P. Kuhl, A. Nilsson, *Angew. Chemie Int. Ed.* **2015**, *54*, 5179–5182.
- [110] F. S. Roberts, K. P. Kuhl, A. Nilsson, *Angew. Chemie* **2015**, *127*, 5268–5271.
- [111] Y. Hori, H. Wakebe, T. Tsukamoto, O. Koga, *Surf. Sci.* **1995**, *335*, 258–263.
- [112] Y. Hori, I. Takahashi, O. Koga, N. Hoshi, *J. Mol. Catal. A Chem.* **2003**, *199*, 39–47.
- [113] S. N. Steinmann, C. Michel, R. Schwiedernoch, J. S. Filhol, P. Sautet, *ChemPhysChem* **2015**, *16*, 2307–2311.
- [114] J. S. Yoo, R. Christensen, T. Vegge, J. K. Nørskov, F. Studt, *ChemSusChem* **2016**, *9*, 358–363.
- [115] J. T. Feaster, C. Shi, E. R. Cave, T. Hatsukade, D. N. Abram, K. P. Kuhl, C. Hahn, J. K. Nørskov, T. F. Jaramillo, *ACS Catal.* **2017**, 4822–4827.
- [116] A. A. Peterson, F. Abild-Pedersen, F. Studt, J. Rossmeisl, J. K. Nørskov, *Energy Environ. Sci.* **2010**, *3*, 1311–1315.
- [117] X. Nie, W. Luo, M. J. Janik, A. Asthagiri, *J. Catal.* **2014**, *312*, 108–122.
- [118] T. Adit Maark, B. R. K. Nanda, *J. Phys. Chem. C* **2016**, *120*, 8781–8789.

- [119] K. S. Rawat, A. Mahata, B. Pathak, *J. Catal.* **2017**, *349*, 118–127.
- [120] X. Nie, M. R. Esopi, M. J. Janik, A. Asthagiri, *Angew. Chemie Int. Ed.* **2013**, *52*, 2459–2462.
- [121] X. Nie, M. R. Esopi, M. J. Janik, A. Asthagiri, *Angew. Chemie* **2013**, *125*, 2519–2522.
- [122] T. Sheng, W. Lin, S. Sun, *Phys. Chem. Chem. Phys.* **2016**, *18*, 15304–15311.
- [123] X. Liu, J. Xiao, H. Peng, X. Hong, K. Chan, J. K. Nørskov, *Nat. Commun.* **2017**, *8*, 15438–15445.
- [124] S. P. Liu, M. Zhao, W. Gao, Q. Jiang, *ChemSusChem* **2016**, 1–8.
- [125] I. Ledezma-Yanez, E. P. Gallent, M. T. M. Koper, F. Calle-Vallejo, *Catal. Today* **2016**, *262*, 90–94.
- [126] F. Calle-Vallejo, M. T. M. Koper, *Angew. Chemie Int. Ed.* **2013**, *52*, 7282–7285.
- [127] F. Calle-Vallejo, M. T. M. Koper, *Angew. Chemie* **2013**, *125*, 7463–7463.
- [128] J. H. Montoya, A. A. Peterson, J. K. Nørskov, *ChemCatChem* **2013**, *5*, 737–742.
- [129] R. B. Sandberg, J. H. Montoya, K. Chan, J. K. Nørskov, *Surf. Sci.* **2016**, *654*, 56–62.
- [130] M. Gattrell, N. Gupta, A. Co, *J. Electroanal. Chem.* **2006**, *594*, 1–19.
- [131] P. Panagiotopoulou, *Appl. Catal. B Environ.* **2018**, *236*, 162–170.
- [132] M. P. Andersson, F. Abild-Pedersen, I. N. Remediakis, T. Bligaard, G. Jones, J. Engbæk, O. Lytken, S. Horch, J. H. Nielsen, J. Sehested, J. R. Rostrup-Nielsen, J. K. Nørskov, I. Chorkendorf, *J. Catal.* **2008**, *255*, 6–19.
- [133] C. Shi, K. Chan, J. S. Yoo, J. K. Nørskov, *Org. Process Res. Dev.* **2016**, *20*, 1424–1430.
- [134] K. J. P. Schouten, Y. Kwon, C. J. M. van der Ham, Z. Qin, M. T. M. Koper, *Chem. Sci.* **2011**, *2*, 1902–1909.
- [135] R. P. Bell, *Proc. R. Soc. A Math. Phys. Eng. Sci.* **1936**, *154*, 414–429.
- [136] M. G. Evans, M. Polanyi, *Trans. Faraday Soc.* **1938**, *34*, 11–24.
- [137] Y. Hori, A. Murata, Y. Yoshinami, *J. Chem. Soc. Faraday Trans.* **1991**, *87*, 125–128.
- [138] J. O. Bockris, N. Pentland, *Trans. Faraday Soc.* **1952**, *48*, 833–839.

-
- [139] A. S. Varela, M. Kroschel, T. Reier, P. Strasser, *Catal. Today* **2016**, *260*, 8–13.
- [140] I. Sharafutdinov, C. F. Elkjær, H. W. Pereira de Carvalho, D. Gardini, G. L. Chiarello, C. D. Damsgaard, J. B. Wagner, J.-D. Grunwaldt, S. Dahl, I. Chorkendorff, *J. Catal.* **2014**, *320*, 77–88.
- [141] D. A. Torelli, S. A. Francis, J. C. Crompton, A. Javier, J. R. Thompson, B. S. Brunschwig, M. P. Soriaga, N. S. Lewis, *ACS Catal.* **2016**, *6*, 2100–2104.
- [142] C. J. H. Jacobsen, S. Dahl, B. G. S. Clausen, S. Bahn, A. Logadottir, J. K. Nørskov, *J. Am. Chem. Soc.* **2001**, *123*, 8404–8405.
- [143] D. A. Hansgen, D. G. Vlachos, J. G. Chen, *Nat. Chem.* **2010**, *2*, 484–489.
- [144] M. P. Andersson, T. Bligaard, A. Kustov, K. E. Larsen, J. Greeley, T. Johannessen, C. H. Christensen, J. K. Nørskov, *J. Catal.* **2006**, *239*, 501–506.
- [145] J. R. V. Garcia, T. Goto, *Mater. Trans.* **2003**, *44*, 1717–1728.
- [146] V. N. Vertoprakhov, S. A. Krupoder, *Russ. Chem. Rev.* **2000**, *69*, 1057–1082.
- [147] H. F. Holtzclaw, J. P. Collman, R. M. Alire, *J. Am. Chem. Soc.* **1958**, *80*, 1100–1103.
- [148] P. Mårtensson, *J. Electrochem. Soc.* **1998**, *145*, 2926–2931.
- [149] J. P. Fackler, F. A. Cotton, *Inorg. Chem.* **1963**, *2*, 102–106.
- [150] J. Goswami, L. Raghunathan, A. Devi, S. A. Shivashankar, S. Chandrasekaran, *Thin Solid Films* **1996**, *15*, 573–575.
- [151] T. H. Stumm, H. van den Bergh, *Mater. Sci. Eng. B* **1994**, *23*, 48–53.
- [152] R. Kas, R. Kortlever, A. Milbrat, M. T. M. Koper, G. Mul, J. Baltrusaitis, *Phys. Chem. Chem. Phys.* **2014**, *16*, 12194–12201.
- [153] H. E. Carlton, J. H. Oxley, *AIChE J.* **1965**, *11*, 79–84.
- [154] G. E. Buono-Core, M. Tejos, G. Alveal, R. H. Hill, *J. Mater. Sci.* **2000**, *35*, 4873–4877.
- [155] L. Brissonneau, C. Vahlas, *Chem. Vap. Depos.* **1999**, *5*, 135–142.
- [156] T. S. Yang, W. Cho, M. Kim, K.-S. An, T.-M. Chung, C. G. Kim, Y. Kim, *J. Vac. Sci. Technol. A Vacuum, Surfaces, Film.* **2005**, *23*, 1238–1243.
- [157] T. M. Chung, S. S. Lee, W. Cho, M. Kim, Y. K. Lee, J. H. Hwang, K. S. An,

- C. G. Kim, *Bull. Korean Chem. Soc.* **2011**, *32*, 783–784.
- [158] H. Choi, S. Park, T. Hyung Kim, *Chem. Mater.* **2003**, *15*, 3735–3738.
- [159] Q. Chen, *J. Electrochem. Soc.* **1991**, *138*, 2821–2826.
- [160] N. Bahlawane, F. Reilmann, L. C. Salameh, K. Kohse-Höinghaus, *J. Am. Soc. Mass Spectrom.* **2008**, *19*, 947–954.
- [161] D. Kim, S. Yoo, K. An, *Bull. Korean Chem. Soc.* **2002**, *23*, 225–228.
- [162] K. W. Chang, J. J. Wu, *J. Phys. Chem. B* **2002**, *106*, 7796–7799.
- [163] C. Birnara, V. G. Kessler, G. S. Papaefstathiou, *Polyhedron* **2009**, *28*, 3291–3297.
- [164] M. Nieminen, L. Niinistö, E. Rauhala, *J. Mater. Chem.* **1996**, *6*, 27–31.
- [165] T. Kada, M. Ishikawa, H. Machida, A. Ogura, Y. Ohshita, K. Soai, *J. Cryst. Growth* **2005**, *275*, 1115–1119.
- [166] G. Bendt, Hauptgruppen- Und Übergangsmetallchalkogenide Aus Lösung Und Gasphase, Dissertation, University of Duisburg-Essen, **2017**.
- [167] A. N. Red'kin, V. I. Tatsii, Z. I. Makovei, A. N. Gruzintsev, E. E. Yakimov, *Inorg. Mater.* **2004**, *40*, 1049–1053.
- [168] S. Lee, K. Kaneko, S. Fujita, *Jpn. J. Appl. Phys.* **2016**, *55*, 1202B8.
- [169] S. Suh, D. M. Hoffman, *Chem. Mater.* **2000**, *12*, 2794–2797.
- [170] S. L. Stoll, E. G. Gillan, A. R. Barron, *Chem. Vap. Depos.* **1996**, *2*, 182–184.
- [171] C. Schmetterer, H. Flandorfer, C. L. Lengauer, J. P. Bros, H. Ipser, *Intermetallics* **2010**, *18*, 277–285.
- [172] A. Kubas, D. Berger, H. Oberhofer, D. Maganas, K. Reuter, F. Neese, *J. Phys. Chem. Lett.* **2016**, *7*, 4207–4212.
- [173] F. Neese, *Wiley Interdiscip. Rev. Comput. Mol. Sci.* **2012**, *2*, 73–78.
- [174] F. Weigend, R. Ahlrichs, *Phys. Chem. Chem. Phys.* **2005**, *7*, 3297–3305.
- [175] S. Grimme, S. Ehrlich, L. Goerigk, *J. Comput. Chem.* **2011**, *32*, 1456–1465.
- [176] J. K. Nørskov, J. Rossmeisl, A. Logadottir, L. Lindqvist, J. R. Kitchin, T. Bligaard, H. Jónsson, *J. Phys. Chem. B* **2004**, *108*, 17886–17892.
- [177] D. R. Tobergte, S. Curtis, *J. Chem. Inf. Model.* **2013**, *53*, 1689–1699.
- [178] H. Hecht, *Präparative Anorganische Chemie*, Springer-Verlag, Berlin, **1951**.
- [179] T. K. Panda, M. T. Gamer, P. W. Roesky, *Organometallics* **2003**, *22*, 877–878.

-
- [180] V. Ritleng, E. Brenner, M. J. Chetcuti, *J. Chem. Educ.* **2008**, *85*, 1646–1648.
- [181] S. Pasykiewicz, A. Pietrzykowski, W. Buchowicz, M. Poptawska, *J. Organomet. Chem.* **1993**, *463*, 235–238.
- [182] A. R. Cowley, A. J. Downs, S. Marchant, V. A. Macrae, R. A. Taylor, S. Parsons, *Organometallics* **2005**, *24*, 5702–5709.

9 Abbreviations

acac	acetylacetonate
ALD	atomic layer deposition
B3LYP	Becke, 3-parameter, Lee-Yang-Paar
CHE	computational hydrogen electrode
CO ₂ RR	CO ₂ reduction reaction
CPCM	conductor-like polarizable continuum model
CVD	chemical vapor deposition
DFT	density functional theory
DSC	differential scanning calorimetry
EDX	energy dispersive X-ray diffraction
Et	ethyl
FE	Faradaic efficiency
GDP	gross domestic product
GGA	general gradient approximation
GTO	Gaussian-type orbital
HER	hydrogen evolution reaction
LDA	local density approximation
Me	methyl
MOCVD	metal organic chemical vapor deposition
NMR	nuclear magnetic resonance
PB	periodic boundaries
PE	primary electrons
PES	potential energy surface
PVD	physical vapor deposition
R	alkyl
RHE	reversible hydrogen electrode
RPBE	revised Perdew-Burke-Ernzerhof
sccm	standard cubic centimeter
SCF	self-consistent field
SE	secondary electrons
SEM	scanning electron microscopy
SHE	standard hydrogen electrode
SPE	single point energy
STO	Slater-type orbital
^t Bu	tertbutyl
U	electric potential
XRD	X-ray diffraction



10 Acknowledgements

I would like to thank

- Prof. S. Schulz for the supervision during my Ph.D., for his advice regarding material synthesis and the granted freedom with the direction of my project.
- Prof. A. Auer for his mentoring in the field of computational chemistry, for the fruitful discussions and his serving as second referee.
- the Max-Planck-Society, especially the IMPRS RECHARGE, for the funding of my project and the provision of computational time.
- Kevin Kaiser for the thoroughly correction of this thesis.
- my family, friends and many coworkers for their support during this 3 1/2 years.



11 Publications

J. Krüger, C. Ganesamoorthy, L. John, C. Wölper, S. Schulz, A General Pathway for the Synthesis of Gallastibenes containing Ga=Sb Double Bonds, *Chem. Eur. J.* **2018**, *24*, 9157-9164.

A. Heckel, G. Bendt, L. John, C. Wölper, S. Schulz, Synthesis and solid-state structures of Ph₃E-Ga(t-Bu₃) adducts, *Appl. Organomet. Chem.* **2018**, *32*, e4430.

J. Krüger, J. Schoening, L. John, C. Wölper, S. Schulz, Synthesis and X-ray crystal structures of Ga-substituted distibenes [L(X)GaSb]₂, *ZAAC* **2018**, *644* (17), 1028-1033.

C. Ganesamoorthy, J. Krüger, E. Glöckler, C. Helling, L. John, W. Frank, C. Wölper, S. Schulz, Comprehensive study on reactions of group 13 diyls with tetraorganodipentelanes, *Inorg. Chem.* **2018**, *57* (15), 9495-9503.

J. Krüger, C. Wölper, L. John, L. Song, P. Schreiner, S. Schulz. Syntheses, Structures and Bonding Analyses of Carbene-stabilized Stibinidenes, *in preparation*.

L. John, S. Schulz, A. Auer, Mechanistic insights into the electrochemical CO₂ reduction to highly reduced products on Cu vs. Ni/Ga intermetallics, *in preparation*.